TOWARDS SINGLE CELL PROTEOMICS

Jörg Ziegler

INAUGURATIONSDISSERTATION

zur Erlangung der Würde eines Doktors der Philosophie

vorgelegt der

Philosophisch-Naturwissenschaftlichen Fakultät

der Universität Basel

von

Jörg Ziegler

aus Seelisberg, Uri, Schweiz

Basel, Schweiz 2012

work hard, work smart,
be honest

Genehmigt von der Philosophisch-Naturwissenschaftlichen Fakultät
Auf Antrag von:
Prof. Dr. Andreas Engel, Fakultätsverantwortlicher
Prof. Dr. Andreas Plückthun, Korreferent
Dr. Celestino Padeste, Experte

Basel, den 22.2.2011
Prof. Dr. Martin Spiess, Dekan

ABSTRACT

Towards Single Cell Proteomics

Jörg Ziegler, M. E. Müller Institut, Biozentrum Universität Basel
4056 Basel, Switzerland

This thesis focuses on different novel ideas and concepts in the area bioanalytics in order to develop the sensitivity and liquid handling towards the level of single cell proteomics.

In biochemical sensors binding events are detected, when target molecules diffuse close enough to interact with specific recognition elements. To develop a fast and sensitive immunosensor, we benefit from short diffusion times and capillarity in microchannels. We fabricated an on-chip immunochemical surface assay which is performed within a microfluidic system. Using such a chip, the concentration of CRP in human blood serum was determined within eleven minutes. We were able to detect less than 1 ng mL^{-1} of CRP using only 1μL of sample. To further reduce the sample volume towards single cells, we first structured surfaces with nanometer-sized patterns to separate, handle and culture individual cells. Pillar arrays with a height of 1 μm, aspect ratios of 1:5 and a top diameter of 120 nm were fabricated in silicon and were used as a master to produce a PDMS intermediate on which PLLA replicas were casted. At an inter-pillar distance of 200 nm, we could show how individual cells grow along the lines of cones replicated in PLLA. To handle the liquid content of individual cells and to detect single molecules within such heterogeneous analytes, we developed a method to prepare total content sample for electron microscopy. The method combines microfluidic-based in-line negative staining for TEM as well as desalting for mass measurements by STEM. The main advantages are the lossless sample preparation by liquid contact writing of micro-patterns on EM grids and excellent staining at physiological pH. To detect low molcular weight single molecules label-free with a very high specificity, we propose to immobilize arrays of single DARPins on a very flat surface and to discriminate

their bound and unbound state by height measurements using AFM. Arrays of immobilization islands for single DARPins were fabricated by EUV-IL, EBL and a newly developed direct immobilization method. By EUV-IL and a glancing angle metal deposition step 20 nm sized gold immobilization islands could be fabricated. By EBL and thermal annealing, arrays of 5 nm sized gold islands have been achieved. These islands are in the size range of single DARPin molecules. To functionalize only the gold islands with DARPins, the surrounding silicon dioxide surface has to be protected against non-specific DARPin adsorption. However PEG molecules for efficient passivation are often to long and the small immobilization islands might be buried by PEG. Therefore we used a photoresist mask and a chemical linker to directly immobilize single DARPins onto silicon dioxide. On the same chip, the pattern size of the mask was varied and besides several mm sized lines full of DARPins, arrays of single immobilized DARPins could be produced. On such arrays, single binding events between DARPins and their corresponding target proteins were detected and bound and unbound DARPins could be discriminated. The developed methodologies and the engineered surfaces are promising tools for the analysis towards single cell proteomics and their further development might result in valuable methods for systems biology.

Keywords: microfluidics, pillar arrays, nano-dot array, single cell, cell growth, TEM, STEM, XIL, EBL, GLAD, thermal annealing, immunoassay, DARPin.

Jörg Ziegler, 2012

List of peer-reviewed papers included in this thesis

Jörg Ziegler, Manuel Simon, Vitaliy Guzenko, Andreas Plückthun, Andreas Engel, Celestino Padeste Label-free Single Molecule Detection using Multi-arrays of Individual Immobilized DARPins *Nature Nanotechnology* **2012** in preparation

Simon Kemmerling, Jörg Ziegler, Gabriel Schweighauser, Stefan A. Arnold, Dominic Giss, Shirley Müller, Philippe Ringler, Kenneth N. Goldie, Niels Goedecke, Andreas Hierlemann, Henning Stahlberg, Andreas Enge, Thomas Braun Connecting μ-Fluidics to Electron Microscopy *Journal of Structural Biology* **2012** 177, 128-134

Vitaliy A. Guzenko, Jörg Ziegler, Anastasia Savouchkina, Celestino Padeste, and Christian David Fabrication of Large Scale Arrays of Metallic Nanodots by means of High Resolution E-beam Lithography *Microelectronic Engineering* **2011** *88*, 1972-1974

C. Padeste, H. Özçelik, J. Ziegler, A. Schleunitz, M. Bednarzik, D. Yücel, V. Hasirci Replication of High Aspect Ratio Pillar Array Structures in Biocompatible Polymers for Tissue Engineering Applications *Microelectronic Engineering* **2011** *88*, 1836-1839

Savouchkina, A. and Foelske-Schmitz, A. and Kotz, R. and Wokaun, A. and Scherer, G.G. and Padeste, C. and Ziegler, J. and Auzelyte, V. and Solak, H. Extreme Ultraviolet Interference Lithography for Generation of Platinum Nanoparticles on Glassy Carbon *Electrochemical Society ECS Trans.* **2010** 25 (24), 175-184

Jörg Ziegler, Martin Zimmermann, Patrick Hunziker, Emmanuel Delamarche High-Performance Immunoassays based on Through-Stencil Patterned Antibodies and Capillary Systems *Analytical Chemistry* **2008**, 80, 1763-1769

List of Peer-reviewed papers not mentioned in this thesis

Sachiko Hiromoto, Joerg Ziegler, and Akiko Yamamoto Morphological Change of Fibroblast Cells on Titanium and Platinum Cultured at Anodic and Cathodic Potentials *Corrosion Engineering* **2008**, 57, 9, 521-535

Broz P, Driamov S, Ziegler J, Ben-Haim N, Meier W, and Hunziker P. Toward Intelligent Nanosize Bioreactors: a pH-switchable, Channel-equipped, Functional Polymer Nanocontainer *Nano Letters* **2006** Oct 11; 6(10):2349-2353

Contributions at international conferences

Jörg Ziegler, Celestino Padeste, Vitaliy Guzenko, Manuel Simon, Lutz Kummer, Andreas Plückthun, Andreas Engel Nanostructured Substrates to Immobilise DARPins for Single Cell Proteomics *Biosensors, Glasgow, United Kingdom* May 23. – 26., **2010**

Helmut Schift, Klaas Hellbernd, Arne Schleunitz, Christian Spreu, Jörg Ziegler, Jaejong Lee Shape Control of Polymer Reflow Structures Fabricated by Nanoimprint Lithography *Nanoimprint & Nanoprint Technology, San Jose, California US* November 11. – 13., **2009**

Jörg Ziegler, Frank A. Zoller, Lutz Kummer, Petra Parizek, Harun H. Solak, Celestino Padeste, Andreas Plückthun, Andreas Engel Highly Selective DARPins and Nanostructured Arrays for Functional Single Cell Proteomics *Single Cell Analysis Workshop, Zürich, Switzerland* September 11. – 12., **2008**

J. Ziegler, M. Zimmermann, P. Hunziker, E. Delamarche Fully Autonomous Microfluidic Capillary Systems for Fast and Sensitive Surface Immunoassays *MicroTAS-2007, Paris, France* October 7. – 11., **2007**

Broz P, Ben-Haim N, Ziegler J, Vebert C, Marsch S, Meier W, and Hunziker P. Nanotechnology in Medicine: Toward Intelligent Nanosize Bioreactors: a pH-switchable, Channel-equipped, Functional Polymer Nanocontainer. *Bio-Valley Science Day, Basel, Switzerland* October 17., **2006**

M. Wolf, M. Zimmermann, J. Ziegler, E. Delamarche and P. Hunziker Receptor-specific Immobilisation of Cells *International Conference on Nanoscience and Technology (ICN+T), Basel, Switzerland* July 30 – August 4., **2006**

Invited Presentations

Jörg Ziegler Towards Single Cell Proteomics *Single Cell Analysis Workshop, Zürich, Switzerland* August 17., **2010**

Jörg Ziegler From Protein Microstructures on Polymers to Nanometersized Immobilisation Sites on SiO2 *FHNW, Windisch, Switzerland* May 19., **2010**

Jörg Ziegler Immunoassays in Microfluidics *IMTEK, Freiburg, Germany*, April 14., **2008**

Jörg Ziegler Antibody Patterning using Through-Stencils *Roche, Basel, Switzerland* March 27., **2008**

Jörg Ziegler Microfluidics used for Immunoassay Development *Physical Chemistry, Basel, Switzerland* November 5., **2007**

Jörg Ziegler and Martin Zimmermann Microfluidics for Point-of-Care Immuno-diagnostics *Bühlmann Laboratories, Schönenbuch, Switzerland* May 9., **2007**

x

Contents

1. General Introduction

All currently known living organisms are based on cells as their smallest fundamental functional unit[1]. Living cells are spatially defined by a biological membrane, which surrounds the whole cell and isolates their content from its environment. Within a cell, proteins are quantitatively the most abundant macro-molecules[2]. As for example, in eukaryotic cells, the total protein concentration is typically 100 mg/mL corresponding to 10^{10} protein molecules per mL and all have their unique functions[3]. Proteins could be described as the work force, doing the tasks defined in the genes. Therefore, to understand which processes in a cell are active at a well-defined point of time under dedicated circumstances, the set of expressed proteins has to be analyzed. In the ideal case the whole proteome of a single cell cultured under well-defined conditions is determined.

The present thesis concentrates on different aspects in the development of protein analytics towards single cell proteomics, i.e. the quantitative determination of minute amounts of proteins by immunochemical methods implemented in a microfluidic device (Chapter 2), the culturing of cells on well-defined polymeric substrates (Chapter 3), the preparation of the content of single cells for protein determination by electron microscopy (Chapter 4) and the development of protein array structures for protein analysis based on AFM height measurements (Chapters 5-7). In the following a general introduction to the fields addressed in the chapters 2-7 is given.

Protein analysis using microfluidic systems – Biochemical tests using immunological methods were first performed and published in 1959 by Yalow and Berson using radioactive labels[4]. Immunoassays[5] are based on the unique property of certain proteins, to selectively bind to other proteins, and to a wide range of other chemical entities like other biomolecules, cells and even metals like gold[6]. Furthermore, they can discriminate binding partners with high specificity[7] and have a high binding affinity towards their target[8]. The binding of the recognition element and its target is defined by the Law of Mass Action[6], and their reversible nature is described by the association rate constant and the dis-

sociation rate constant. From the association and the dissociation rate constants, the equilibrium constant – also known as the affinity constant – is derived. Immunoassays have been developed in different variations as for example direct, competitive, displacement or sandwich immunoassay. Sandwich immunoassays as they are used for the experiments in chapter two of this thesis are typically performed sequentially in three steps on a solid surface with a specifically tuned antibody pair, i.e. the capture and detection antibody (cAb and dAb, respectively). In the first step the cAbs are immobilized on the surface. Then the analyte solution is applied on such prepared surfaces in step two so that the cAbs bind their antigens present in the analyte solution. Finally in the third step, a labeled dAb is bound in order to quantify the amount of antigen captured by the cAb. Examples for labels include radioactive isotopes, enzymes, or fluorescence dyes. The measured signal is thereby related to the concentration of antigen in the analyte solution. To prevent hindering of binding between the cAb and dAb, those pairs have to be tuned to each other. Furthermore washing steps are necessary between each step, to minimize unspecific signals. Today, immuno-assays are widely used and well described and they represent a very important diagnostic method in basic life sciences and in the field of medical analysis. For example, lateral flow assays used for pregnancy tests[9] or nicotine abuse[10]. These tests are non-invasive, self-explaining and simple to use and patients may be able to interpret the results by themselves. In science, immunoassays are very often performed in micro titer plates that cover the need for a highly flexible format. In medical diagnostics, more emphasis is put on high throughput rather than on flexibility. Several companies are producing fully automated high-throughput analytical systems for centralized medical laboratories. Such highly integrated chemical analyzers allow a broad range of body fluids to be analyzed, as for example saliva, urine, arterial or venous blood or cerebrospinal liquor. A full random access of samples and a throughput of 200 tests/hour[11] and up to 15 million tests per year are common[12]. Even if those machines are highly accurate and still preserve a valuable flexibility, turnaround times are long and large volumes of analyte solutions are needed. To achieve shorter process times and smaller volumes, the fluidic system has to be made smaller, down to micrometer sized channel dimensions, where very small analyte volumes can be used in combination with very fast diffusion times.

The concept of microfluidics uses the extraordinary properties of liquids confined in micrometer scale for transportation, processing and analysis of liquid samples. In microfluidics, surface tension forces generally dominate gravity, inertia or friction. Surface tension originates from cohesive intramolecular forces and describes the interaction of a liquid with its surrounding gas. The Young's equation relates the energies at the vapor-solid, liquid-solid, and vapor-liquid interfaces via the equilibrium contact angle of the liquid to the solid surface. Hereby the contact angle can be used as a measure of wettability of a surface in the case of aqueous liquids. Poorly wettable surfaces manifest themselves with a contact angle bigger than 90° at the solid-liquid-vapor contact line and are commonly defined as hydrophobic, whereas wettable surfaces are called hydrophilic and show contact angles smaller than 90°. The contribution of the surface tension to the pressure in rectangular capillaries is described by the Young-Laplace equation[13, 14, 15]. The capillary pressure is depending on the flow velocity, i.e. the volume of liquid which flows in a certain time through the capillary. The miniaturization affects also the absolute number of analyte molecules present in a sample. In the system investigated in chapter 2, 1 µL of human serum spiked with 0.1 µg/mL C-reactive protein (CRP) was typically used. This corresponds to about 5700 CRP molecules in a microliter of analyte. Even if the absolute number of molecules compared to the volume of the analyte seems to be small, diffusion is relatively high in micro-meter scale volumes compared to the macroscopic world. Since the flow regime is laminar, mixing of reagents occurs due to diffusion instead of turbulences such as in large volumes[16, 17, 18]. Fick's law describes the flux of diffusion and using the Stokes-Einstein-relation the diffusion coefficient of globular proteins can be calculated. In aqueous solutions, the diffusion constant of proteins ranges typically form ~10^{-7}-10^{-5} cm^2 s^{-1} depending on their size. As an example, a protein having the size of 17 kDa has a diffusion coefficient of 10^{-6} cm^2 s^{-1} and it needs 0.05 s for a diffusion distance of 10 µm. Such short diffusion times and small analytical volumes make microfluidics very interesting for detection applications in the biological field.

Separation, handling and culturing of individual cells – Frequently published and straightforward methods for cell separation are geometrical trapping structures based on the steric fit of cells within micro-scale wells of a similar dimension. The cells are seeded on the prefilled well array and allowed to settle into the wells. After settlement, cells that are not inside a well are washed away. Such cell arrays allow a high throughput analysis at an individual cell level under even more controllable environmental conditions compared to cells grown on a Petri dish[19]. Wheeler et al. created a system combining structures and channels, to trap individual cells and to apply reagents by microfluidics[20]. Another passive technique uses the change of the fluidic resistance when microstructures are loaded by single cells[21]. This cell-trapping device can again be integrated in a microfluidic system to control the perfused environment and the cellular behavior can be observed using a standard microscope. Another approach is to isolate individual cells within small droplets of immiscible fluids[22]. In this case, proteins and other biomolecules secreted by individual cells can be collected, concentrated and provided for further analysis. This is not possible in single cell arrays, sharing the same medium because secreted biomolecules diffuse and mix up within the environmental medium. Using a microfluidic droplet generator, this method has the potential of high-throughput analysis by still observing single cells[23]. However, the described methods to separate cells all consider the cell as a particle and not as a living entity, which can grow, adapt its morphology and actively change its position. Especially during the proliferation phase, cells react to differences in the chemical coating and topographical property of surfaces and adapt their growing direction. The influence of nanostructured substrates on the cell growth has been shown in chapter 4. We developed a two-step replication process, to successfully produce 2 x 2 mm arrays of cone structures with an aspect ratio of 1:5 and top diameters of 120 nm in poly-L-lactide (PLLA). The nanopatterned PLLA substrates were further coated with fibronectin and the influence of inter-pillar distances on cell outgrowth along cone lines could be shown.

Analytics at the level of single cells – Over the last years, biological research made big progress in the characterization of single biological components, for

example in the determination of protein structures or the decoding of the human genome sequence. To understand the relationship between these different elements each of them has to be analyzed at distinct times. As so far, large numbers of cells have to be analyzed to obtain sufficient ratios between signal and background. This analysis strategy has the drawback that each measurement represents an average that might hide differences in between individual cells. Well-known examples are single bacteria, which are resistant to antibiotics. This antibiotic resistance of single cells in an otherwise genetically identical population most likely originates in different expression of specific proteins. However, population-based methods cannot detect the small differences of protein expression of single cells[24] and therefore it is necessary to analyze cells individually.

Once cells are separated, several methods are available to investigate their properties and to determine the spatial arrangement of intracellular elements within single cells. To assess the stiffness and surface roughness of single cells and bacteria in vitro and in vivo, the atomic force microscope (AFM) can be used in contact or non-contact mode[25, 26, 27]. Immunostaining with fluorescent labels is used to localize distinct proteins within cells. To clearly recognize the spatial composition of single cells (Cryo-) EM tomography[28, 29] is currently the leading technology. However (Cryo)-EM tomography is limited to cells with a maximum diameter of about 2 μm. To analyze the content of bigger cells the cell membrane has to be lysed.

The lysis of single cells can be achieved by optical, acoustic, mechanical, electrical or chemical means[30]. During pulsed laser microbeam-induced cell lysis, which is an optical method, a nanosecond pulse from a 532 nm laser is focused through a high numerical aperture objective lens to a small spot where localized plasma formation occurs. This results in the generation of a shock wave, followed by generation of a cavitation bubble that expands and contracts within a few microseconds. The cells are lysed either during the expansion of the cavitation bubble or during bubble collapse, when a liquid jet is directed downwards onto the slide[31]. Mechanical lysis using sharp edges, termed 'nanoknives' and produced by multiple isotropic deep reactive ion etch steps, has been demonstrated to lyse cells very efficiently[32]. Detergent-based lysis arises from incorporation of detergent into the cell membrane to solubilize lipids and proteins in the

membrane, creating pores within the membrane. The selection of the surfactant is significant since it can affect the speed of cell lysis, as well as the protein extraction efficiency. Strong ionic detergents such as sodium dodecyl sulphate (SDS) are able to provide cell lysis of the order of seconds, but they tend to denature proteins from the cell. However, denatured proteins are unfavorable in structure determination and also in protein binding or enzyme activity assays. Milder non-ionic detergents such as Triton X-100 cause slower cell lysis, and have a much lower tendency to denature proteins[33]. Zwitterionic detergents such as CHAPS (3-[(3-cholamidopropyl)dimethylammonio]-1-propane-sulphonate) can be used for cell lysis as well, and result in no net change in the charge of solubilized proteins[34]. Electric fields generating transmembrane potentials of the order of 0.2-1.5 V cause rupture of the lipid bilayer. Pores are formed in the cell membranes, and with a sufficient magnitude of electric field and a sufficient exposure time cells are lysed[35, 36]. The cell size, shape and membrane composition determines the electric field strength required to promote cell lysis. In acoustic cell lysation, ultrasonic waves generate localized areas of high pressure that shear cells. Some cell membranes can resist quite high shear forces and long sonication steps are necessary, leading to a significant heating of the sample and thus denaturing of proteins. However by a precedent treatment with a detergent, sonication can lyse cells easier[37].

Once single cells are lysed, care has to be taken on how to handle the small volumes. The whole content of single cells can be analyzed with several methods using capillaries or lab-on-chip devices. McClain and coworkers demonstrated a microfluidic device, where Jurkat cells loaded with fluorogenic dyes were electrically lysed on a chip. A hydrodynamic flow was used to direct the cellular debris to waste while the dyes were electrokinetically transported into an orthogonal channel for electrophoretic separation and laser induced fluorescence detection (LIF)[38]. A microfabricated fluidic device for the automated real-time analysis of individual cells using capillary electrophoresis (CE) and electrospray ionization mass spectrometry (ESI-MS) was developed and used by Mellors et al.[39]. Their microfluidic structure incorporates a means for rapid lysis using a combination of rapid buffer exchange and an increase in electric field strength and a free solution electrophoresis channel, where cellular constituents are separated. An

electroosmotic pump is incorporated at the end of the electrophoretic separation channel to direct the eluent to the integrated electrospray emitter for ionization of separated components to be analyzed by mass spectrometry (MS). To provide biochemical specificity to EM-based protein analytics, Kelly et al. recently functionalized EM grids with nickel-nitrilotriacetic acid groups (Ni-NTA)[40]. These so-called Affinity Grids, are EM grids coated with a dried lipid monolayer that contains Ni-NTA lipids as used for monolayer purification. His-tagged proteins or macromolecular complexes could be rapidly and conveniently captured and prepared for electron microscopy, without the need of any biochemical purification. Since the Affinity Grids are stable for some time in the presence of glycerol and detergents, it was possible to isolate His-tagged aquaporin-9 (AQP9) from detergent-solubilized membrane fractions of Sf9 insect cells. His-tagged proteins could even be isolated within minutes from Escherichia coli cell extracts.

In chapter 4 we propose a direct writing of total volume cell lysate on EM grids for structure and mass analysis by transmission electron microscopy (TEM) and scanning TEM (STEM), respectively. In a microfluidic system, the negative staining of the whole cell content is done by dialysis followed by pipetting through a thin nozzle, which deposits the analyte in small meandered traces on a conventional EM grid.

AFM-based proteomics – As a drawback of the EM techniques as discussed above, are the mapping of small changes of the protein structure, like different phosphorylation states or the detection of proteins smaller than 30 kDa is almost impossible. Therefore, we propose to functionalize surfaces with ordered arrays of single distinct immunochemical receptor molecules in order to capture the target molecules from analyte solutions on predefined places. Using immunochemical receptors, it is no longer necessary to detect the structure of a protein to determine its concentration, but to simply count bound and unbound receptors. By a statistical evaluation of the two states, the concentration of the target protein in the solution can be determined and a detection limit towards single molecules seems to be possible. To detect the size difference of single bound and unbound receptor elements to sub 30 kDa target molecules, the reso-

lution of the detection method has to be better than 1 nm. As a possible detection tool, atomic force microscopes (AFM) can deliver the requested resolution, however only in the z-direction. Therefore the receptor molecules have to be immobilized at relatively large distances on a very flat surface.

As an example, Ros et al. used AFM techniques to detect and probe immobilized recombinant single-chain Fv fragment (scFv) antibody molecules on template stripped gold surfaces[41]. The scFv's directed against the antigen fluorescein were covalently immobilized on a flat gold surface via the C-terminal cysteine, resulting in a high accessibility of the binding site. In AFM height measurements on functionalized and non-functionalized areas Ros et al. could confirm the immobilization of scFv. Furthermore the functionality of the immobilized scFv was determined by directly measuring the unbinding force to the antigen fluorescein, which was immobilized covalently via a long hydrophilic spacer to the silicon nitride SPM-tip. Thus, closely related antibody molecules differing in only one amino acid at their binding site could be distinguished. However it is a challenge to efficiently passivate a gold surface against unspecific binding. Therefore it would be of an advantage, to have gold only as the material of the immobilization island, to bind proteins via the SH-group by their accessible cysteine[42]. Glass et al. demonstrated such gold immobilization islands on solid surfaces fabricated by self-assembly processes[43]. They used polymeric micelles with a gold core and immobilized them in a homogenous layer on a silicon dioxide surface. After the immobilization, a plasma treatment completely destroyed the polymer shell and removed the entire remaining polymer, resulting in gold particles arranged in regular distances. By varying size of the polymer shell, the spacing between the gold particles can be changed. Immobilization of single antibodies without metal islands is reported by He et al.[44]. They describe a DNA self-assembly into well-defined two-dimensional (2D) mesh with a tetragonal order and a side length of about 19 nm. Already before, DNA-based self-assembly with millimeter-sized well-ordered 2D arrays and features of nanometer scale, had been reported and were used as templates to organize nanoparticles and macromelecules[45]. However He et al.[44] conjugated antigens into the DNA motifs and turned the otherwise passive DNA mesh into an active antibody array. Two fluorescein moieties were covalently conjugated with the DNA during synthesis.

After self-assembly, the antigen-containing DNA arrays were incubated with anti-fluorescein antibodies (IgG) in solution. The two fluorescein moieties on the cross of the DNA motif can simultaneously bind to the two antigen-binding sites of the "Y"-shaped IgG molecule. By AFM measurements the height of the DNA arrays was found to be 1.7-1.9 nm, while the height of the antibody was 2.7-3.5 nm. By using DNA self-assembly very high density antibody arrays were produced with an excellent orientation of the antibody. However there is no free antigen-binding site available in the antibodies. To turn their DNA self-assembled arrays into active sensor surfaces, biotin was conjugated to the DNA. By incubating streptavidin, 2D streptavidin arrays could be generated, to which biotinylated antibodies could bind. But IgGs or the biotin-avidin-constructs are big and flexible. This makes them difficult to be imaged by AFM and it is almost impossible to detect bound target molecules, which are six times smaller than the IgG itself. Therefore, a receptor molecule that is small and stable, but still as specific as possible and with a very low Koff would be required.

These requirements are fulfilled by the recently developed Designed Ankyrin Repeat Proteins (DARPins)[46]. DARPins are constructs of two to five repeat motifs and origin in the naturally occurring ankyrin proteins. Ankyrin proteins are an own class of proteins with characteristically high affinity protein-protein interactions. The used DARPins have three repeat motifs with large variable target interaction surfaces. The amino acids at this interaction surface are not essential to preserve the protein structure, but are responsible for the interaction to the target protein. By exchanging them with any of the naturally occurring amino acids except cysteine, glycine and proline, the dissociation constant can be enhanced towards picomolar affinity or the specificity to another binder can be changed[7]. The three repeating units building the binding domain are flanked with stabilizing constant repeat motifs. The total mass of the used DARPin is around 14 kDa, which corresponds, related to its elongated oval structure, to a width of about 5 nm and a length of about 8.5 nm.

To immobilize single DARPins on a surface, the immobilization islands should have a size comparable to a single DARPin molecule. To clearly discriminate one single DARPin from its neighboring DARPin by AFM, the spacing of the immobilization islands on the surface has to be well defined, wide enough and

very regular. Furthermore, arbitrary guiding structures to localize the array of very small immobilization islands by means of AFM are necessary. Those specifications make it difficult to produce arrays by self-assembly. Therefore, we used top-down fabrication methods such as extreme UV interference lithography (EUV-IL) and electron beam lithography (EBL) combined with thin film metal deposition, to produce gold islands on solid substrates. By using EUV-IL, as described in chapter five, we could successfully produce masks with openings of 60 nm and a period of 100 nm. By an additional glancing angle metal deposition (GLAD) we could successfully constrict the opening by 50% of the original size. After applying an annealing step the resulting immobilization islands, were very homogeneous and stable enough on the surface for the subsequent immobilization and background passivation steps. However, with a diameter of about 30 nm, they were still big compared to the DARPin molecules.

Using state of the art EBL we could successfully produce gold immobilization islands of 6 nm in diameter. To reach such small sized immobilization islands, we used a double layer photoresist and an additional annealing step after lift-off, as described in chapter 6 of this thesis. In order to bind the DARPins only to the gold islands, the surrounding silicon dioxide surface has to be passivated to minimize non-specific protein adsorption. The fact that the passivation has to be applied before DARPin immobilization turned out to be a major disadvantage of the developed gold dot array structures. The diameter and the height of around 3 nm of the gold dot structures are small compared to the size of efficient passivation chemicals, such as poly(-ethyleneglycol) derivatives with chain lengths which are often several times the height of the immobilization islands[47], leading to a full coverage of the whole surface. As a consequence the immobilization islands are completely buried in the passivation layer and they can no longer be accessed and functionalized by DARPins. Therefore it would be preferable to immobilize the DARPin on the substrate, before the lift-off of the mask. Through the holes of the mask, single DARPin molecules could bind to the dedicated areas on the substrate and any unspecific binding of the DARPins to the mask is washed away during the lift-off of the mask. Such a process would lead to well arranged DARPin pattern on an otherwise clean substrate surface, but it is only possible if the capture molecules remain functional after the lift-off

process in organic solvents. This is unusual for many proteins but proved to be possible for DARPins. In chapter 7 we describe the development of a process based on EBL to create a patterned Poly(Methyl-Methacrylic Acid) (PMMA) mask on a silicon dioxide substrate. Using linker chemistry, we could successfully immobilize DARPins covalently to the oxidized silicon. After dissolution of the PMMA mask the DARPin functionalized surfaces were passivated and used to detect target proteins. On the same substrate we could immobilize μm-sized patterns of DARPins for the detection with fluorescence labels, but also single DARPin molecules, detected by the described height discrimination using an AFM. Single binding events were detectable and DARPins with and without their bound target protein could be discriminated.

1.1 References

1 Alberts, B.; Johnson, A.; Lewis, J.; Raff, M.; Roberts, K. and Walter, P. *Garland Science,* **2002**.

2 Eckert, W. A. and Kartenbeck, J. *Springer Labormanuale*, **1997**.

3 Voet, D. and Voet, J. *Biochemistry, J. Wiley & Sons,* **2004**.

4 Yalow, R. and Berson, S. *Nature,* **1959***, 184*, 1648-1649.

5 Wild, D. *Elsevier Science,* **2005**.

6 Ibii, T.; Kaieda, M.; Hatakeyama, S.; Shiotsuka, H.; Watanabe, H.; Umetsu, M.; Kumagai, I. and Imamura, T. *Analytical Chemistry, American Chemical Society,* **2010**.

7 Binz, H. K.; Amstutz, P.; Kohl, A.; Stumpp, M. T.; Briand, C.; Forrer, P.; Grutter, M. G. and Plückthun, A. *Nat Biotech, Nature Publishing Group,* **2004***, 22*, 575-582.

8 Weber, P.; Ohlendorf, D.; Wendoloski, J. and Salemme, F. *Science,* **1989***, 243*, 85-88.

9 Cole, L. A.; Sutton-Riley, J. M.; Khanlian, S. A.; Borkovskaya, M.; Rayburn, B. B. and Rayburn, W. F. *Journal of the American Pharmacist Association,* **2005***, 45*, 608-615.

10 NicAlert *http://www.americanscreeningcorp.com/NicAlert_P1246C29.cfm,* **2011**.

11 High-throughput automated immunoassay analyzer. *Medical Laboratory Observer,* **2009**

12 Roche, cobas e 602 *http://www.roche.com/de/media/media_releases/med-cor-2010-07-20.htm,* **2011**.

13 Young, T. *Philosophical Transactions of the Royal Society of London, The Royal Society,* **1805***, 95*, 65-87.

14 Rüger, A. *Centaurus,* **1985***, 28*, 244-276.

15 Förste, J., Spurk, J. H. *WILEY-VCH Verlag,* **1991***, 71*, 442-442.

16 Purcell, E. M. *American Journal of Physics,* **1977***, 45*, 3-11.

17 Zimmermann, M.; Delamarche, E.; Wolf, M. and Hunziker, P. *Biomed Microdevices,* **2005***, 7*, 99-110.

18 Zimmermann, M.; Schmid, H.; Hunziker, P. and Delamarche, E. *Lab Chip,* **2007***, 7,* 119-125.

19 Rettig, J. R. and Folch, A. *Analytical Chemistry,* **2005***, 77,* 5628-5634.

20 Wheeler, A. R.; Throndset, W. R.; Whelan, R. J.; Leach, A. M.; Zare, R. N.; Liao, Y. H.; Farrell, K.; Manger, I. D. and Daridon, A. *Analytical Chemistry,* **2003***, 75,* 3581-3586.

21 Di Carlo, D. and Lee, L. P. *Analytical Chemistry,* **2006***, 78,* 7918-7925.

22 He, M.; Edgar, J. S.; Jeffries, G. D. M.; Lorenz, R. M.; Shelby, J. P. and Chiu, D. T. *Analytical Chemistry, American Chemical Society,* **2005***, 77,* 1539-1544.

23 Edd, J. F.; Di Carlo, D.; Humphry, K. J.; Koster, S.; Irimia, D.; Weitz, D. A. and Toner, M. *Lab Chip, The Royal Society of Chemistry,* **2008***, 8,* 1262-1264.

24 Taniguchi, Y.; Choi, P. J.; Li, G.-W.; Chen, H.; Babu, M.; Hearn, J.; Emili, A. and Xie, X. S. *Science,* **2010***, 329,* 533-538.

25 Stolz, M.; Gottardi, R.; Raiteri, R.; Miot, S.; Martin, I.; Imer, R.; Staufer, U.; Raducanu, A.; Duggelin, M.; Baschong, W.; U., D.; Friederich, N. F.; Aszodi, A. and Aebi, U. *Nat Nano, Nature Publishing Group,* **2009***, 4,* 186-192.

26 Fantner, G. E.; Barbero, R. J.; Gray, D. S. and Belcher, A. M. *Nat Nano, Nature Publishing Group,* **2010***, 5,* 280-285.

27 Lister, T. E. and Pinhero, P. J. *Langmuir, American Chemical Society,* **2001**, 17, 2624-2628.

28 Ben-Harush, K.; Maimon, T.; Patla, I.; Villa, E. and Medalia, O. *J Cell Sci,* **2010***, 123,* 7-12.

29 Lucic, V.; Forster, F. and Baumeister, W. *Annual Review of Biochemistry,* **2005***, 74,* 833-865.

30 Brown, R. B. and Audet, J. *Journal of the Royal Society Interface,* **2008***, 5,* S131-S138.

31 Rau, K. R.; Quinto-Su, P. A.; Hellman, A. N. and Venugopalan, V. *Biophysical Journal,* **2006***, 91,* 317-329.

32 DiCarlo, D. D.; Jeong, K.-H. and Lee, L. P. *Lab Chip, The Royal Society of Chemistry,* **2003***, 3,* 287-291.

33 Berezovski, M. V.; Mak, T. W. and Krylov, S. N. *Analytical and Bioanalytical Chemistry,* **2007***, 387,* 91-96.

34 Pang, Z.; Al-Mahrouki, A.; Berezovski, M. and Krylov, S. N. *Electrophoresis,* **2006***, 27,* 1489-1494.

35 Rols, M. P. and Teissie, J. *Electricity and Magnetism In Biology and Medicine,* **1993**, 151-154.

36 Lu, K.-Y.; Wo, A. M.; Lo, Y.-J.; Chen, K.-C.; Lin, C.-M. and Yang, C.-R *Biosensors and Bioelectronics, Selected Papers from the 2nd International Meeting on Microsensors and Microsystems,* **2006***, 22,* 568-574.

37 Zhang, H. and Jin, W. *Journal of Chromatography A,* **2006***, 1104,* 346-351.

38 McClain, M. A.; Culbertson, C. T.; Jacobson, S. C.; Allbritton, N. L.; Sims, C. E. and Ramsey, J. M. *Analytical Chemistry, American Chemical Society,* **2003***, 75,* 5646-5655.

39 Mellors, J. S.; Jorabchi, K.; Smith, L. M. and Ramsey, J. M. *Analytical Chemistry, American Chemical Society,* **2010***, 82,* 967-973.

40 Kelly, D. F.; Abeyrathne, P. D.; Dukovski, D. and Walz, T. *Journal of Molecular Biology,* **2008***, 382,* 423-433.

41 Ros, R.; Schwesinger, F.; Padeste, C.; Pluckthun, A.; Anselmetti, D.; Guntherodt, H. J. and Tiefenauer, L. *Scanning and Force Microscopies For Biomedical Applications, Proceedings of,* **1999***, 3607,* 84-89.

42 Bain, C. D.; Biebuyck, H. A. and Whitesides, G. M. *Langmuir, American Chemical Society,* **1989***, 5,* 723-727.

43 Glass, R.; Arnold, M.; Cavalcanti-Adam, E. A.; Bluemmel, J.; Haferkemper, C.; Dodd, C. and Spatz, J. P. *New Journal of Physics,* **2004***, 6,* 101.

44 He, Y.; Chen, Y.; Liu, H.; Ribbe, A. E. and Mao, C. *Journal of the American Chemical Society, American Chemical Society,* **2005**, 127, 12202-12203.

45 Zhang, J.; Liu, Y.; Ke, Y. and Yan, H. *Nano Letters, American Chemical Society,* **2006**, 6, 248-251.

46 Binz, H. K.; Stumpp, M. T.; Forrer, P.; Amstutz, P. and Plückthun, A. *Journal of Molecular Biology,* **2003**, 332, 489-503.

47 Huang, N. P.; Michel, R.; Voros, J.; Textor, M.; Hofer, R.; Rossi, A.; Elbert, D. L.; Hubbell, J. A. and Spencer, N. D. *Langmuir,* **2001***, 17,* 489-498.

2. High-Performance Immunoassays Based on Through-Stencil Patterned Antibodies and Capillary Systems

Jörg Ziegler[1] Martin Zimmermann,[1,2] Patrick Hunziker,[1]

Emmanuel Delamarche,[2]

[1] University Hospital Basel, Petersgraben 4, 4031 Basel, Switzerland

[2] IBM Research GmbH, Zurich Research Laboratory, Säumerstrasse 4,
   8803 Rüschlikon, Switzerland

2.1 Keywords

stencil, protein deposition, microfluidic, immunoassay, autonomous capillary system, PDMS, CRP

2.2 Abbreviations

BSA, bovine serum albumin; **cAb(s)**, capture antibody(-ies); **CRP**, C-reactive protein; **CS(s)**, capillary system(s); **dAb(s)**, detection antibody(-ies); **HDT**, hexadecanethiol; **HS-PEG**, thiolated poly[ethylene glycol]; **PBS**, phosphate-buffered saline; **PDMS**, poly[dimethylsiloxane]

2.3 Abstract

We present a simple method to pattern capture antibodies (cAbs) on poly(dimethylsiloxane) (PDMS), with high accuracy and in a manner compatible with mass fabrication for use with capillary systems (CSs), using stencils microfabricated in Si. Capture antibodies are patterned as 60-270 µm wide and 2 mm long lines on PDMS and used with CSs that have been optimized for convenient handling, pipetting of solutions, pumping of liquids, such as human blood serum, and visualization of signals for fluorescence immunoassays. With the use of this method, C-reactive protein (CRP) is detected with a sensitivity of 0.9 ng mL^{-1} (7.8 pM) in 1 µL of CRP-spiked human serum, within 11 min and using only four pipetting steps and a total volume of sample and reagents of 1.35 µL. This exemplifies the high performances that can be achieved using this approach and an otherwise conventional surface sandwich fluorescence immunoassay. This method is simple and flexible and should therefore be applicable to a large number of demanding immunoassays.

2.4 Introduction

Immunoassays are widely used for diagnostics, research in life sciences, therapy monitoring, environmental monitoring, and food safety.[1] These assays rely on the specific interaction between antigens and antibodies to detect analytes (antigens or antibodies) of interest in body fluids or other samples. Even for a

average flow rates in the reaction chambers	sample viscosity [mPas]	reaction chamber			
		20 µm deep		30 µm deep	
		[nL s^{-1}]	CV (%)	[nL s^{-1}]	CV (%)
water	1	1.9	4.7	4.2	4.8
PBS + 1% BSA	1	1.9	5.0	4.0	3.4
solution of 20% hum. albumin	4	0.5	12.0	1.5	11.9

Table 1. Characteristic flow rates of samples when filling CSs.

Flow resistors   **Vent**

Loading   **PDMS**   **Reaction**   **Capillary**   **0.5 cm**

pad   **with cAbs**   **chamber**   **pump**
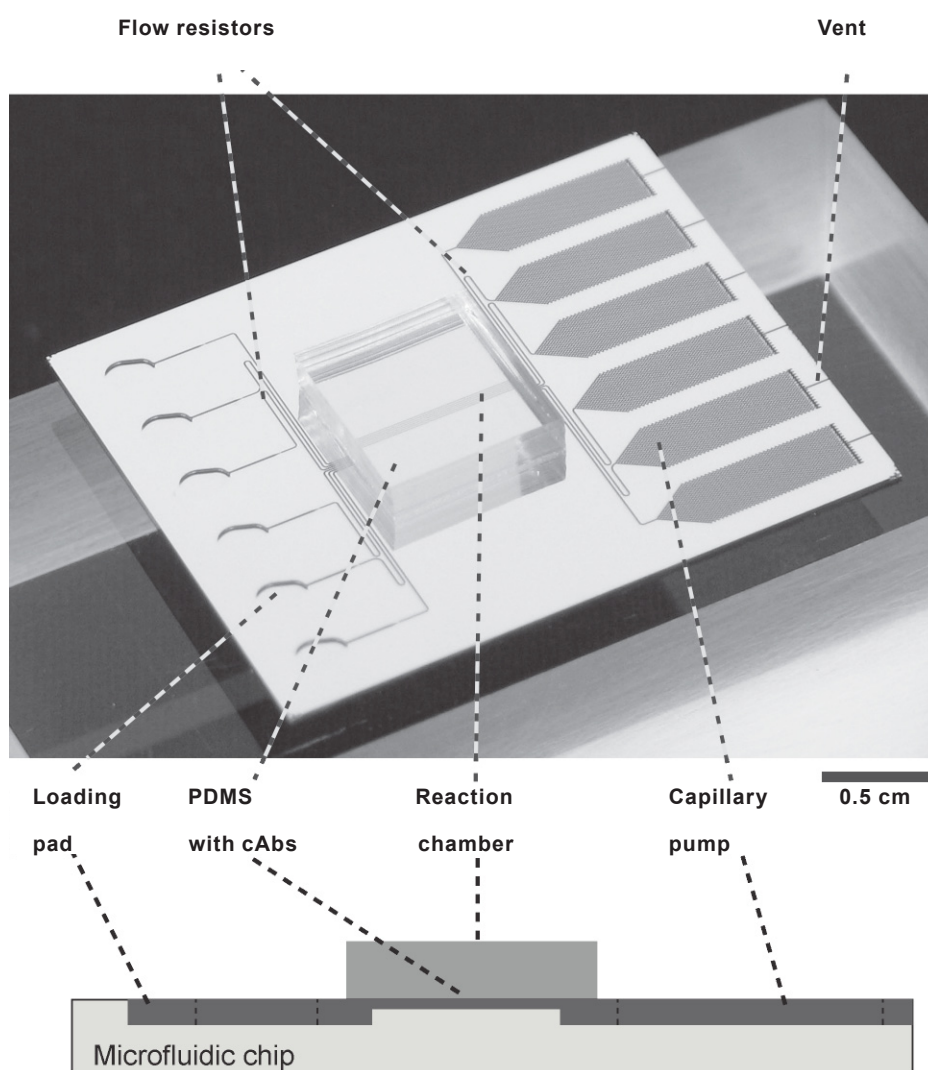
Microfluidic chip

Figure 1. Photograph of an Au-coated silicon microfluidic chip having six independent CSs. Up to six independent surface immunoassays can be performed using such a chip. Assays are performed by successively loading samples and reagents into the loading pads and capturing analytes flowing in the reaction chambers using cAbs, which are patterned on a sealing block of PDMS.

single type of application, the requirements for having informative and efficient immunoassays can vary strongly. There is, for example, a notable difference between platforms used for portable immunoassays done near a patient and a clinical analyzer from the central laboratory of a hospital.[2] The first platform must be simple to use and provides results within minutes, whereas a clinical analyzer typically runs a large number of possible tests and can process samples (i.e. filtration, dilution, thermal treatment, spinning, etc.) to optimize the sensitivity and accuracy of the test. Immunoassays that are used for research in life sciences are usually more specialized and customized than those for diagnostic applications. The signal of an immunoassay can be based on radioactivity, light (emitted or absorbed), electrochemistry,[3] a current,[4] fluorescence, or even changes in the index of refraction[5] or mass of a sensing surface[6]. These assays comprise numerous incubation and rinsing steps, with volumes of solution ranging from a microliter to hundreds of microliters. These steps can last for a few seconds, for example, when rinsing or adding reagents, to hours, for example for ligand-receptor binding reactions for high-sensitivity assays or for depositing a cAb on a the surface of the well of a microtiter plate. The diversity of platforms,[7] formats, and steps performed for immunoassays in research suggests that new platforms should be versatile and flexible in the number of steps and volumes of solutions they can accommodate. We pioneered the concepts of microfluidic networks and then CSs with the goal of providing convenient platforms for high-performance immunoassays.[8] Key to these concepts is the use of a PDMS substrate patterned with receptors for analytes that can reversibly seal microfluidic structures.[9] The microfluidic structures are accurately prepared by means of microfabrication using Si wafers or in plastics using replication techniques. CSs extend microfluidic networks by implementing a more precise control over the filling behavior of liquids entering the microstructures.[10] They typically have loading pads, inside which reagents and samples are pipetted, reaction chambers covered with PDMS, and capillary pumps. Valves and flow resistances can also be added to reduce evaporation of liquid, meter liquid, or delay the progression of a liquid in some parts of the CS.[8, 11] Importantly, the geometry and wetting properties of the microstructures encode a precise capillary pressure in the various parts of the CSs, which permits drawing a desired amount of liquid in a CS with a controlled flow rate without requiring actuated pumping systems.
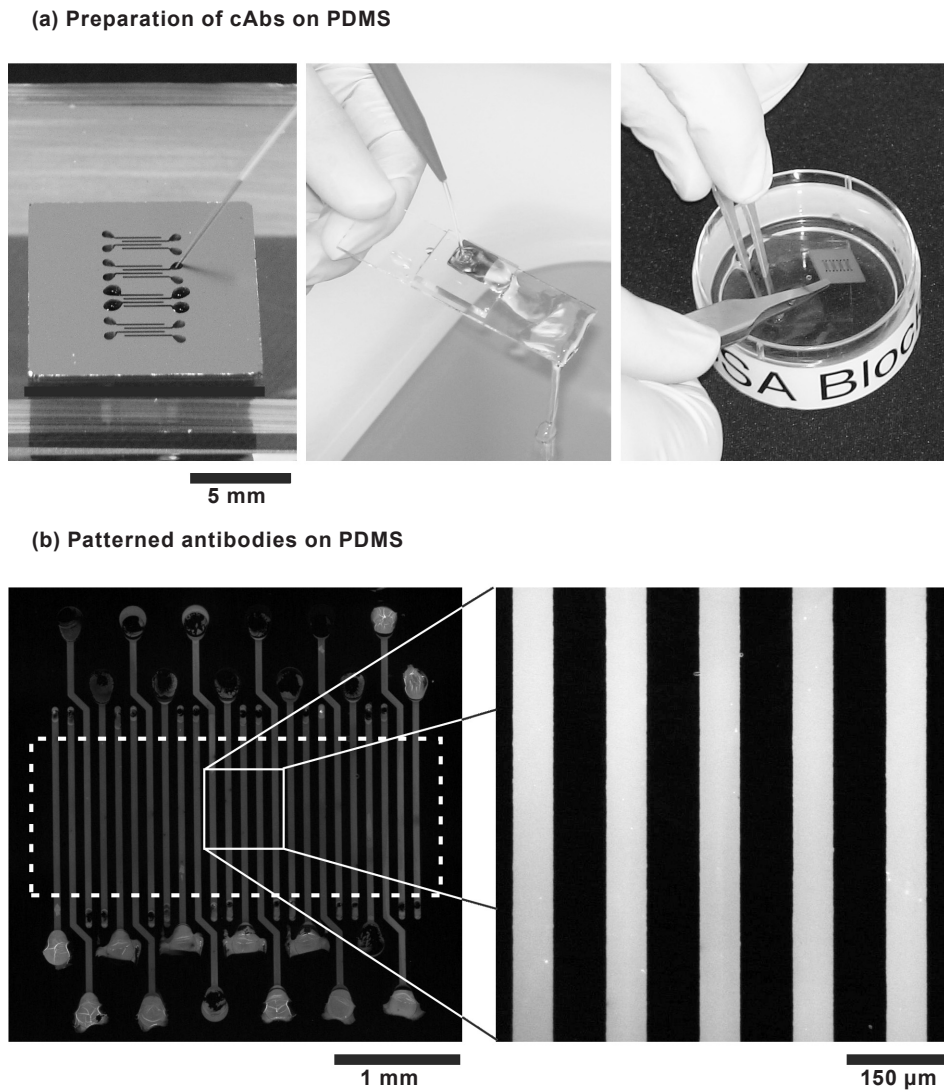
(a) Preparation of cAbs on PDMS

5 mm

(b) Patterned antibodies on PDMS

1 mm   **150 µm**

Figure 2. Local delivery of Abs to PDMS areas using microfabricated stencils. (a) The 2-mm-long stencils of a silicon template can be filled individually with a solution of Abs, and rinsed under a stream of PBS and deionised water. The PDMS is then separated from the template under a blocking solution of BSA and dried. (b) Fluorescence micrograph showing the accurate delivery of TRITC-labeled Abs through stencils onto a PDMS surface homogeneously covered with cAbs.

The merit of CSs for immunoassays is the possibility to detect rapidly multiple analytes in samples smaller than 1 µL in volume.[12] Here the patterning of cAbs on PDMS plays a critical role by providing well-defined areas for the capture of analytes from solution. These areas, which are typically a few tens of micrometers in lateral dimensions, help limiting the depletion of analytes[13] and can be spaced so as to provide many contiguous signals and controls, which is useful for the combinatorial screening of analytes,[14] for imaging data in one step, and for achieving assays with small intra-assay variations.[10] These assays, called "micromosaic immunoassays", utilize two microfluidic chips for patterning cAbs and dispensing samples.[15]

We present in this paper a method for accurately patterning Abs on PDMS using stencils and use the patterned Abs with CSs for effecting highly miniaturized fluorescence surface immunoassays. We first describe the functions of the CSs for immunoassays and the use of the stencils for delivering Abs to a PDMS surface, and then assess the characteristics of sandwich fluorescence surface immunoassays. These immunoassays were performed with stencil-deposited cAbs, the new CSs, and human serum spiked with CRP. CRP is protein rapidly synthesized by the liver in response to many conditions, including infection, inflammation, and cardiovascular diseases.[16, 17, 18]

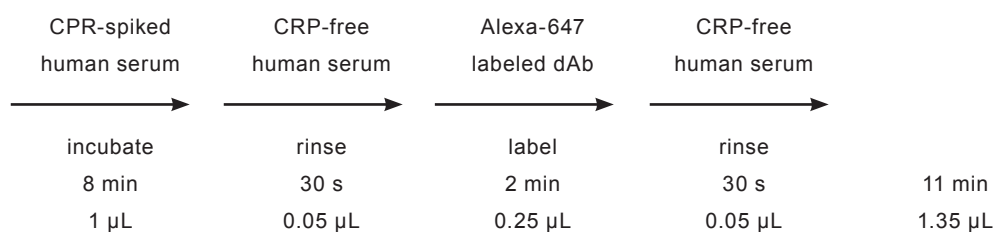| CPR-spiked human serum	CRP-free human serum	Alexa-647 labeled dAb	CRP-free human serum	
→	→	→	→	
incubate	rinse	label	rinse	
8 min	30 s	2 min	30 s	11 min
1 µL	0.05 µL	0.25 µL	0.05 µL	1.35 µL

Figure 3. Flow scheme of the steps necessary for an assay in CSs. The immunoassay comprises four pipetting steps (arrows), for incubation of the analyte, rinsing of noncaptured analytes, binding dAbs to captured analytes, and rinsing excess dAbs. The purpose of the steps, the volume of reagent and sample used, and the duration of the steps are displayed below the arrows.
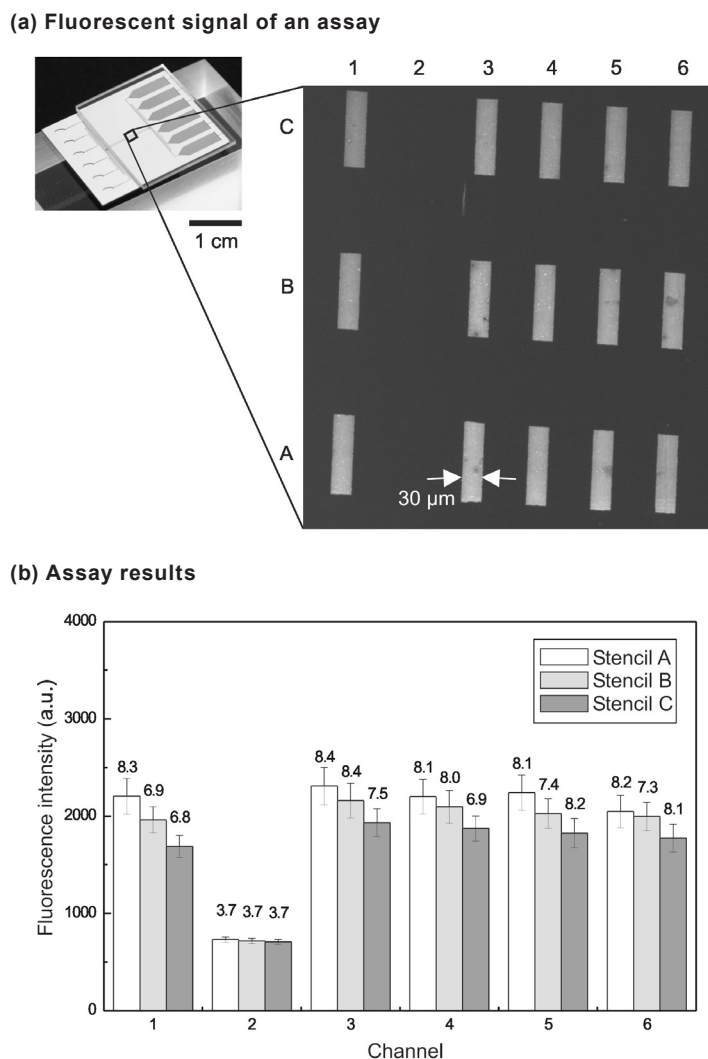
(a) Fluorescent signal of an assay

(b) Assay results

Figure 4.   Fluorescence surface immunoassays for CRP performed in CSs using cAbs patterned on PDMS using a stencil template. (a) The CSs were sealed with PDMS from the beginning of the reaction chamber to the end of the capillary pumps. The PDMS was patterned with lines of one type of cAbs (CRP-C2, 125 µg mL^{-1}) which cross the reaction chambers of the CSs. The optical micrograph shows the fluorescence signal of Alexa-647-labeled dAbs (CRP-C6, 250 µg mL^{-1}) after five identical assays (CRP, 0.1 µg mL^{-1}) were performed in each CS except in channel 2, in which the analyte was free of CRP. (b) The bar chart shows the mean fluorescence intensity of the signals shown in (a) with the standard deviation.

2.5 Materials and Methods

2.5.1 Reagents and Proteins

Solutions of phosphate-buffered saline (PBS) (tablets P4417, Sigma) and bovine serum albumin (BSA) (Sigma) were reconstituted in ultra pure water (Millipore Simplicity 185, Bedford MA) and filtered prior to use with a 0.20-µm syringe filter (Sartorius, Epsom UK). Solutions of alkanethiols were prepared in ethanol (puriss. ≥ 99.8%, Fluka) using thiolated poly(ethylene glycole) (HS-PEG, 12750-4, Rapp Polymere GmbH, Tübingen, Germany) and hexadecanethiol (HDT, 52270, Fluka, Buchs, Switzerland). PDMS prepolymers (Sylgard 184, Dow Corning, Midland MI) were mixed at a ratio of 1:10 using a DOPAG mixer (Cham, Switzerland), poured onto planar polystyrene Petri dishes (Greiner BioOne), and cured overnight in an oven at 60 °C. The cured 3-mm-thick layer of PDMS was cut into 8×8 mm^2 pieces. Antibodies were patterned on the surface of the PDMS that faced the Petri-dish.

Lyophilized goat anti-rabbit IgG (R2004, Sigma-Aldrich) and rabbit anti-guinea pig IgG TRITC-labelled (T7153, Sigma-Aldrich) were reconstituted in PBS at concentrations of 125 and 250 µg mL^{-1}, respectively. Human CRP (8C72), anti-CRP (4C28-C2, 4C28-C6), anti-CRP-FITC (4C28F-C6) and human CRP-free serum (8CFS) were bought from HyTest (Turku, Finland) and diluted in PBS. Human CRP-free serum was spiked with human CRP to the desired CRP concentration. The anti-CRP-C6 Abs were labeled using an Alexa Fluor® 647 labeling kit (Alexa Fluor® 647 Monoclonal Antibody Labeling Kit, Molecular Probes). The number of fluorophores per protein was measured to be four using an Eppendorf BioPhotometer.

2.5.2 Handling of Microfluidic Capillary Systems and Templates

The microfluidic CSs and the stencil templates were etched in Si using photolithography and deep reactive-ion etching. The CSs were sputtered with Au and diced to yield individual microfluidic chips having 6 CSs each.

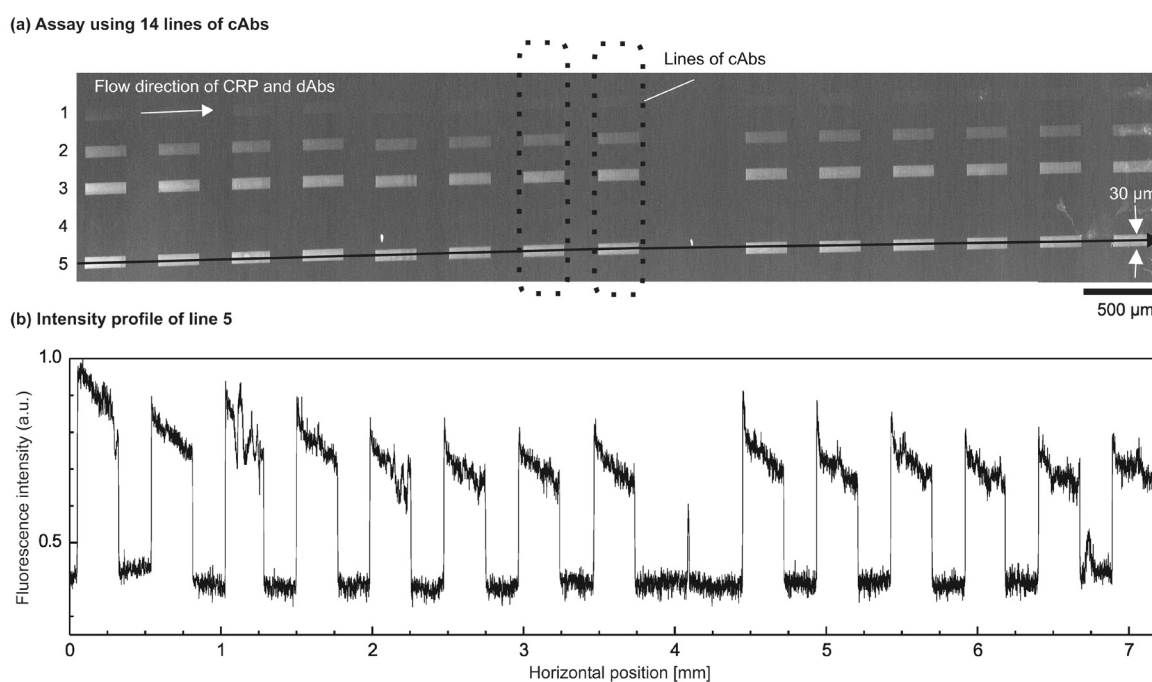Prior to each use, the microfluidic chips were cleaned in an UV-ozone reactor

(a) Assay using 14 lines of cAbs

Flow direction of CRP and dAbs

Lines of cAbs

1
2
3
4
5

30 μm

500 μm

(b) Intensity profile of line 5

Fluorescence intensity (a.u.)

1.0

0.5

0   1   2   3   4   5   6   7

Horizontal position [mm]

Figure 5.   Micromosaic immunoassay for CRP performed in CSs and using cAbs patterned on PDMS through a stencil (a) patterned using a capture area having a total length of 3.7 mm and 14 lines of cAbs on PDMS. The optical micrograph shows the fluorescence signals of the assay, in which 14 lines of cAbs were crossed horizontally by CRP diluted in PBS and then FITC-labeled dAbs in PBS. The cAbs were deposited from solution onto PDMS using two concentrations (125 and 250 μg mL^{-1} on, respectively, the eight columns on the left and six on the right). The CRP concentrations were 0.04 (CS 1), 0.2, 0.5, 0, and 1 μg mL^{-1}. The concentration of dAbs was 250 μg mL^{-1}. (b) Fluorescence intensity profile of surface-bound dAbs along the center of channel 5.

24

(UV-Ozone Photoreactor PR-100, Ultra-Violet Products, Upland, CA) during 60 min. A planar PDMS stamp having the size of a microfluidic chip was inked with a 2 mM solution of HDT in ethanol for 30 s, rinsed with ethanol, and dried under a stream of N_2. The PDMS stamp was applied manually to the chip for 30 s to make its top surface hydrophobic. The chip was then covered with a 2 mM solution of HS-PEG in ethanol for 30 s, rinsed with ethanol, and dried under a stream of N_2 to render the CSs wettable and the surfaces protein-repellent. The derivatized chips were stored in dry environment and typically used within 6 h.

The Si wafers with the stencils were diced into 12×12 mm^2 individual templates having 16 or 24 stencils. Each stencil comprises a loading pad connected to a 2-mm-long line. The templates were cleaned in O_2 plasma (Tepla Microwave-Plasma System 100, PVA Tepla, Asslar Germany) during 2 min at 200 W and 0.7 Torr before they were placed on the PDMS block. The stencils were filled with a solution of cAbs for a 15-min-long deposition of cAb on PDMS at room temperature. The stencils in contact with PDMS were rinsed under a stream of PBS and ultra pure water. The PDMS surface was separated from the stencil using tweezers, exposed to a blocking solution of BSA for 15 min, rinsed with PBS and ultra pure water, and dried under a stream of N_2. The templates were rinsed and cleaned in an O_2 plasma before reuse.

The PDMS block was placed on the CSs in such a way that the lines of cAbs were oriented perpendicularly to the reaction chambers of the CSs. A non-patterned block of PDMS was used to seal the capillary pumps. Immunoassays were performed by pipetting the solution of analyte into the loading pads of the CSs, followed by a solution for rinsing and a solution containing detection antibodies (dAbs). CRP-free human serum was then placed around the PDMS substrate, which was removed from the CSs. The PDMS was rinsed under a stream of PBS and ultra pure water, dried under a stream of N_2, and imaged. Fluorescence micrographs were obtained using a fluorescence microscope (Eclipse 90i, Nikon, Japan), which was equipped with a 100 W halogen lamp for excitation, and a digital camera (DS-1QM, Nikon) cooled to –30 °C for imaging. Fluorescence micrographs were analyzed using the software NIS-Elements (Nikon). After the experiments, the microfluidic chips were rinsed with PBS, ultra pure water and

ethanol, dried under a stream of N_2, and cleaned again in the UV-ozone reactor.

2.6 Results and Discussion

2.6.1 Capillary Systems for Multiplexed Immunoassays

Figure 1 shows a microfluidic chip having six independent CSs with their reaction chambers sealed with a block of PDMS. All structures of the CSs have a depth of 180 μm, except for the reaction chambers, which are 20 μm deep. A depth of 180 μm enables loading pads and sealed capillary pumps to hold a total volume of 2 μL without requiring too large a footprint on the chip. When 2 μL of solution are pipetted into a loading pad, most of the solution protrudes outside of the pad without spreading toward adjacent pads because the top part of the chip is covered with a hydrophobic self-assembled monolayer. These pads are approximately twice as large as those of the previous CSs to ease the loading of solutions using manual micropipetting.[8] The depth of the reaction chambers provides a good compromise between having an efficient transport of analytes to the capture sites,[19, 20] keeping the hydraulic resistance of the reaction chambers low, and preventing the collapse of the PDMS into the chamber.[21] The reaction chambers are 30 μm wide, 9 mm long, and are separated from each other by 120 μm. Their length permits the convenient manual placement of a block of PDMS having numerous lines of cAbs, and their spacing allows six rows of signals per millimeter. Grouping the reaction chambers in the center of the chip facilitates imaging the results of assays because the fluorescence signals on the surface of PDMS can be acquired in one imaging step.[10] The total volume of 2 μL of the capillary pumps was selected based on previous work, in which 600 nL of sample were used for high sensitivity assays,[10] and based on the maximum volume of dAbs and rinsing solution estimated to be necessary for completing the assay. The pumps have a vent to prevent the entrapment of air. The use of large pads and pumps and the grouping of reaction chambers in the middle of the chip make the CSs asymmetric: CSs near the edges of the chip have longer distances between pads, pumps, and reaction chambers. For this reason, mean-
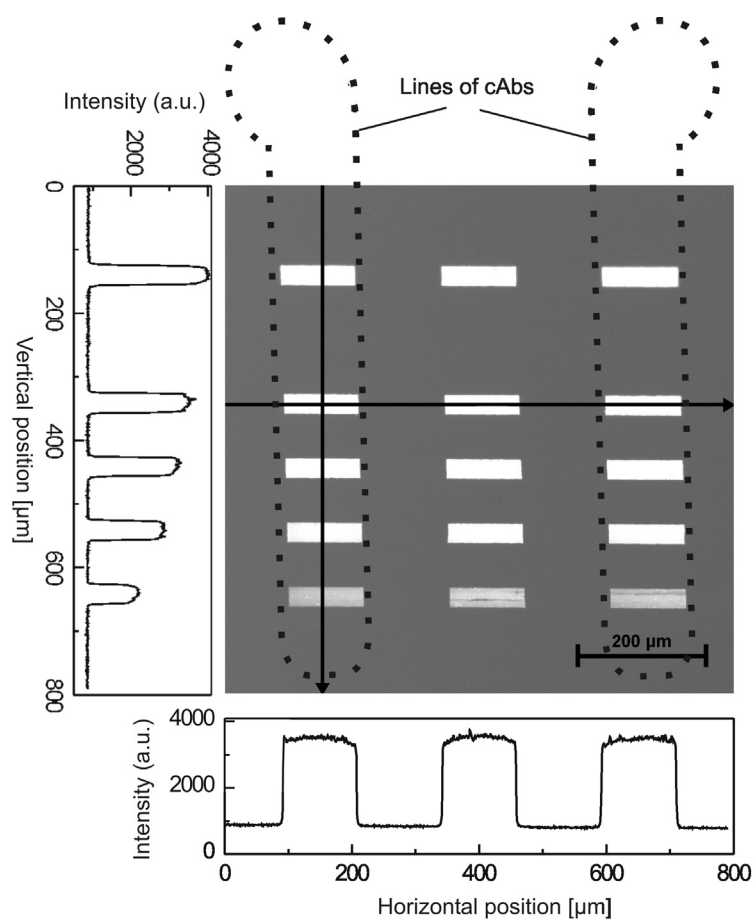
Figure 6.   Micromosaic immunoassay for CRP in human serum. Optical micrograph showing a mosaic of fluorescence signals corresponding to the detection of CRP using cAbs (125 μg mL^{-1} in PBS) deposited onto PDMS using stencils. CRP-spiked CRP-free human serum and FITC-labeled dAbs (250 μg mL^{-1} in CRP-free human serum) were provided horizontally in independent CSs. The CRP concentrations were 10 (top row), 0, 3, 1, 0.3, and 0.1 μg mL^{-1}. Each concentration of CRP results in a fluorescence intensity as can be seen in the vertical graph on the left-hand side. The horizontal intensity profile gives the fluorescence intensity of a particular CRP concentration over different lines of cAbs.
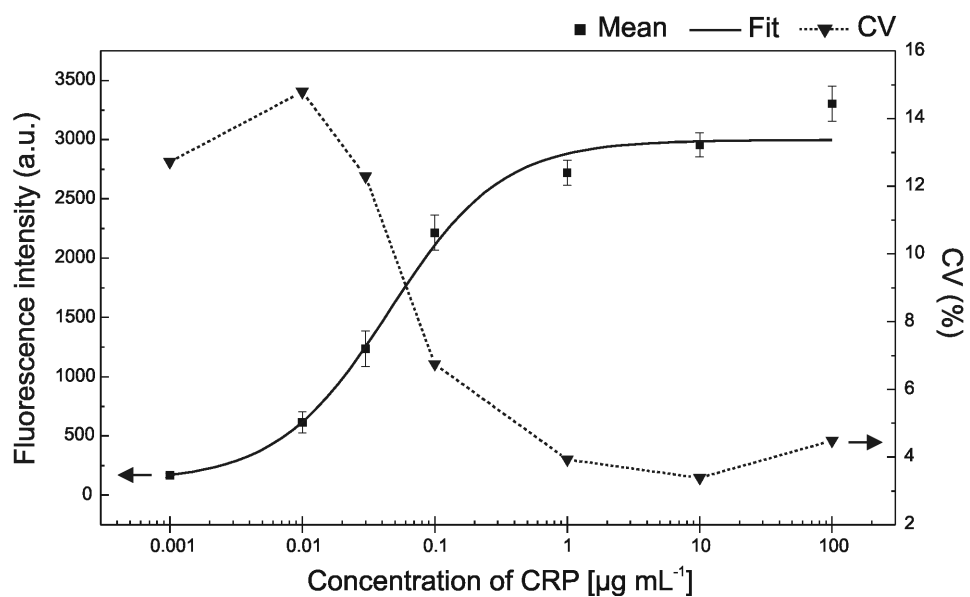
Figure 7.   Reference curve of a micromosaic immunoassay for CRP in human serum. Plot of the fluorescence intensities obtained from assays done with different concentrations of CRP (■) and their coefficient of variation (▼). The fluorescence intensities are fitted with a sigmoidal curve (solid line). Error bars correspond to the standard deviation. This assay has a calculated sensitivity of 0.9 ng mL^{-1}. The dotted line is a guide to the eye.

dering channels are added to the inner CSs to equalize the hydraulic resistance of all CSs.

A sample added to a loading pad of a CS flows through the reaction chamber and moves into the capillary pump at a flow rate depending in part on the surface tension and viscosity of the sample, Table 1. Water and a solution of 1% BSA in PBS, which has a similar viscosity as human serum (1 mPa s), flow at 1.9 nL s^{-1} with variations ≤ 5% through CSs having 20-µm-deep reaction chambers. Reducing the hydraulic resistance of the CSs by using 30-µm-deep reaction chambers increases the flow rate to 4.2 nL s^{-1} for water and 4 nL s^{-1} for PBS containing 1% BSA. Blood or blood plasma, which might be used in point-of-care applications, have higher viscosities than serum. The blood viscosity depends on the hematocrit and can amount to 3 to 8 times the viscosity of water, with typical values being 3 to 4.[22] As blood is a non-Newtonian liquid, the viscosity therefore depends also on its velocity.[23] The viscosity of plasma is ~1.8× higher than that of water. We chose a solution of 20% human albumin as a model liquid to measure the flow rate of a liquid having a viscosity of 4 mPa s in CSs. As expected, such a liquid flows slower than less viscous solutions with flow rates of 0.5 and 1.5 nL s^{-1} in CSs having 20-µm-deep and 30-µm-deep reaction chambers, respectively. The coefficient of variation is ~12% in both cases, which might be improved by optimizing the internal structures in the capillary pump to have finer and more continuous structures. In the experiments described next, CSs having 20-µm-deep reaction chambers are used, in which 0.9 µL of human serum flow within ~8 min.

2.6.2 Patterning Antibodies on PDMS using Stencils

Figure 2 shows a template that is used to localize antibodies to specific areas of a PDMS surface as well as fluorescence images of the resulting patterns. The template was microfabricated in Si and has zones with four stencils. The template can readily be rendered hydrophilic or cleaned for reuse by using an O^2-based plasma. The template is placed manually on a block of PDMS, and the conformal contact occurring between the PDMS and the template seals the stencils. The stencils are accessible from above and can be filled individually by

manual pipetting. The pads and stencils are laid out in such a way as to ease the addressing of each pad while keeping the stencils grouped as much as possible to keep the assay signals of the as contiguous as possible. Using a pitch of 1 mm for the loading pads and keeping the solution of antibody solution that is pipetted into the pads to values smaller than 0.3 μL help prevent pad overflow and cross-talk when pipetting manually. We found that a deposition time of 15 min was sufficient to saturate the PDMS surface with a layer of Abs using a 125 μg mL^{-1} solution of Abs in PBS. The filled template was kept in a humid environment during deposition to prevent evaporation of solution from the stencils. All stencils were rinsed for a few seconds using a flexible dispensing bottle filled with PBS and with the jet of PBS being in the direction of the stencils, Figure 2a. The template adhered well to the PDMS, even during intense rinsing involving multiple steps. The template was separated from PDMS in a BSA bath to quickly cover any area of PDMS left free of Abs with BSA. The fluorescence images in Figure 2b show an example of delivering Abs locally to PDMS areas using 60-μm-wide stencils. In this case, cAbs (anti-rabbit IgGs) have been homogeneously applied from solution to PDMS and 0.3 μL aliquots of TRITC-labeled rabbit IgGs were locally provided in each stencil. The homogenous fluorescence signals observed in the inner area of the template (dashed rectangle in Figure 2b) underline the homogeneous, local delivery of Abs to the PDMS surface. Having a pad at the beginning of each stencil not only facilitates the addressing of the stencil but also helps localize imperfections (drying artifacts, entrapment of air bubble) away from the areas used for the assay.

Stencils can greatly vary in size and be several hundreds micrometer wide,[24, 25] a few micrometers in diameter,[26, 27] or even just 100 nm in size.[28] Here, we looked for stencils that were (i) easy to microfabricate even with micrometer accuracy, (ii) small enough to enable the delivery of approximately 6 to 10 solutions of proteins per millimeter across capture areas and to allow the use of sub-microliter volumes of protein solution, and (iii) made from a material that can withstand strong oxidizing conditions so that cleaning them and removing proteins from the template would be easy using ozone, oxidative plasmas, or oxidants in solution. The length of the stencils provides the possibility of patterning long lines of cAbs on PDMS, thereby preventing issues involved in aligning the reaction

chambers of CSs with the patterned cAbs. The width of the stencils defines one lateral dimension of the mosaic of fluorescence signals. We were not able to fill stencils individually by hand if their pads had a pitch of 0.6 mm. Pipetting robots can in principle be used for filling higher-density stencils and/or preparing PDMS substrates in mass for miniaturized immunoassays. In the remainder of the paper, cAbs for CRP are patterned onto PDMS using 16 stencils as shown in Figure 2a, with a pitch of 1 mm between pads and 120- to 270-μm-wide stencils. These assays have a potential maximum of 96 test sites when combined with a microfluidic chip having six independent reaction chambers.

2.6.3 Fluorescence Immunoassays in CS and Stencil-Patterned Abs

A first series of immunoassays was performed in CSs using human serum spiked with 0.1 μg mL^{-1} CRP to determine the homogeneity of the fluorescence intensity in adjacent capture areas and CSs, Figure 4. This immunoassay was also developed with the goal of using minute volumes of solutions and brief incubation times. One microliter of CRP-spiked human serum was added in each pad of the CSs, except in CS No. 2, in which CRP-free human serum was loaded to provide a control. After a quick rinsing step with CRP-free human serum, 0.25 μL of a solution of Alexa-647 labeled dAbs was flowed through the CS for 2 min, followed by a second brief rinsing step, Figure 3. After 11 min, the assay was finished and the block of PDMS separated from the CSs in the presence of human serum. The PDMS surface was rinsed, dried, and the fluorescent signals were imaged. A fluorescence image of a block of PDMS having three rows of cAbs (A, B, C, deposited using the stencils) that are crossed by six CSs (1 − 6) is shown in Figure 4b. CRP in the CSs passed over rows A, B, and then C. The 15 zones of signal shown in Figure 4a are accurate rectangles, having a width of 30 μm (corresponding to the width of the reaction chamber in the CS) and a length of 120 μm (corresponding to the width of the stencils). No signal was generated in CS 2 or outside the areas of PDMS, where no cAbs had been patterned, as expected. A detailed comparison of the fluorescence intensities of the individual areas, Figure 4b, reveals that corresponding areas A1-A6, B1-B6 and C1-C6 in independent CSs have similar intensities, whereas the areas A, B, and

C in the same CS have decreasing intensities. The first areas of cAbs (A) passed by CRP exhibit a larger fluorescence intensity than the subsequent areas (B, C). This decrease of the fluorescence intensity is due to a slight depletion of CRP analyte in the reaction chamber during the capture step.

2.6.4 Assay Homogeneity and Performance

In Figure 5, 14 lines of cAbs and 5 lines CSs were used, and CRP was omitted in one of the CSs to provide a control. An intensity profile of the fluorescence signal corresponding to a concentration of CRP of 1 µg mL^{-1} is shown in Figure 5. The fluorescence intensity of the signals slowly decreases from the first area of cAbs to the last one, and it decreases faster along one area of cAb. This reflects the depletion of CRP along the reaction chamber, but also the enrichment in CRP of the depleted boundary layer during the 0.22 s it takes the sample to reach the next capture area. After the fourth capture area, the mean fluorescence signals of the remaining areas are equal, which suggests that the depletion layer in proximity to the surface has grown and a steady state has been reached between the diffusive and convective mass transport of CRP to the cAbs areas and the binding of CRP to the cAbs.

Figure 6 and 7 shows a micromosaic immunoassay for CRP using CSs and stencil-deposited cAbs that results from using three lines of cAbs (120 µm wide stencils) and six CSs (30 µm wide reaction chambers). The flow rate in this assay was controlled entirely by the capillary pump, and no particular precaution had to be taken to prevent evaporation of the liquids added to the pads. The fluorescence intensity of the signals on each row was averaged and used to make a reference curve of the assay. A total of six independent experiments were performed to obtain the reference curve shown in Figure 7. The calculated sensitivity of the assay (smallest concentration more than 3 times the standard deviation of the zero analyte concentration) is 0.9 ng mL–1, i.e. 7.8 pM. The coefficients of variation are < 8% for concentrations ≥ 0.1 µg mL–1 and 12 to 15% for smaller concentrations. The sensitivity of the CRP assay shown here is impressive, considering that 1 µL of sample for multiple test areas, 11 min, and a conventional immunoassay format were used. This assay is notably fast, sensi-

tive, and economical of sample compared with commercially available ELISA assays for CRP.[29] The sensitivity might be further improved by employing signal-amplification strategies similar to the work by Hosokawa et al.,[30] although this would be at the expense of making the assays longer, using more reagents, and adding numerous pipetting steps. PDMS has a refractive index of 1.47, is transparent, and has a low autofluorescence for wavelengths below 600 nm.[10] It is therefore possible to measure the fluorescent signals of the mosaic directly through PDMS without having to remove PDMS from the CSs and drying the PDMS surface. The PDMS might serve as long pass fluorescence filter,[31] or have optical fibers embedded to enhance coupling of light.[32] Preliminary experiments showed a decrease in sensitivity of the assays probably due to optical effects (data not shown).[33] The in situ detection of CRP, and potentially many other markers, is nevertheless promising for further simplifying the use of CSs and encoding immunoassays on microfluidic chips for point-of-care diagnostics.

2.7 Conclusion

Stencil-based patterning of cAbs on a PDMS substrate is a convenient method to immobilize cAbs on PDMS in a manner that should be compatible with techniques used for the mass fabrication of diagnostic devices. We regard the accurate patterning of cAbs as key to achieve high-performance surface immunoassays that do not require complex or cumbersome peripherals, surface engineering, or signal-amplification methods. By following the method and examples provided here for stencils and CSs, we suggest that users interested in detecting antigens in microliters or less of samples should easily be able to set their own assays using standard reagents, pipetting methods, and fluorescence readers. We also note that fluorescence is increasingly used for immunoassays and that synergies exist between the method presented here and long-wavelength fluorophores, quantum dots, and portable fluorescence readers.

2.8 Acknowledgment

2.9 References

1 Wild, D.; Ed. *The Immunoassay Handbook*, Elsevier Ltd.: Oxford, **2005**.

2 St-Louis, P. *Clin. Biochem.* **2000**, *33*, 427–440.

3 Rossier, J. S. and Girault, H. H. *Lab Chip* **2001**, *1*, 153–157.

4 Diaz-Gonzalez, M.; Gonzalez-Garcia, M. B. and Costa-Garcia, A. *Electroanalysis* **2005**, *17*, 1901–1918.

5 Homola, J. *Anal. Bioanal. Chem.* **2003**, *377*, 528–539.

6 Baselt, D. R.; Lee, G. U. and Colton, R. J. *J. Vac. Sci. Technol. B* **1996**, *14*, 789–793.

7 Bilitewski, U. *Anal. Chim. Acta* **2006**, *568*, 232–247.

8 Delamarche, E.; Juncker, D.; Schmid, H. *Adv. Mater.* **2005**, *17*, 2911–2933.

9 Delamarche, E.; Bernard, A.; Schmid, H.; Michel, B. and Biebuyck, H.; *Science* **1997**, *276*, 779–781.

10 Juncker, D.; Schmid, H.; Drechsler, U.; Wolf, H.; Wolf, M.; Michel, B.; de Rooij, N. and Delamarche, E. *Anal. Chem.* **2002**, *74*, 6139–6144.

11 Zimmermann, M.; Schmid, H.; Hunziker, P. and Delamarche, E. *Lab Chip* **2007**, *7*, 119–125.

12 Cesaro-Tadic, S.; Dernick, G.; Juncker, D.; Buurman, G.; Kropshofer, H.; Michel, B.; Fattinger, C. and Delamarche, E. *Lab Chip* **2004**, *4*, 563–569.

13 Ekins, R. P. *Clin. Chem.* **1998**, *44*, 2015–2030.

14 Wolf, M.; Juncker, D.; Michel, B.; Hunziker, P. and Delamarche, E. *Biosens. Bioelectron.* **2004**, *19*, 1193–1202.

15 Bernard, A.; Michel, B. and Delamarche, E. *Anal. Chem.* **2001**, *73*, 8–12.

16 Ridker, P. M. *Circulation* **2003**, *107*, 363–369.

17 Hansson, G. K. *N. Engl. J. Med.* **2005**, *352*, 1685–1695.

18 Vasan, R. S. *Circulation* **2006**, *113*, 2335–2362.

19 Zimmermann, M.; Delamarche, E.; Wolf, M. and Hunziker, P. *Biomed. Microdev.* **2005**, *7*, 99–110.

20 Lion, N.; Reymond, F.; Girault, H. H. and Rossier, J. S. *Curr. Opin. Biotechnol.* **2004**, *15*, 31–37.

21 Bietsch, A. and Michel, B. *J. App. Phys.* **2000**, *88*, 4310–4318.

22 Guyton, A. and Hall, J. *Textbook of Medical Physiology*, Saunders: Philadelphia, **2000**.

23 Haynes, R. and Burton, A. *Am. J. Physiol.* **1959**, *197*, 943–950.

24 Schwarz, A.; Rossier, J. S.; Roulet, E.; Mermod, N.; Roberts, M. A. and Girault, H. H. *Langmuir* **1998**, *14*, 5526–5531.

25 Rucker, V.; Havenstrite, K.; Simmons, B.; Sickafoose, S.; Herr, A. and Shediac, R. *Langmuir* **2005**, *21*, 7621–7625.

26 Ostuni, E.; Kane, R.; Chen, C.; Ingber, D. and Whitesides, G. *Langmuir* **2000**, *16*, 7811.

27 Folch, A.; Jo, B.; Hurtado, O.; Beebe, D. and Toner, M. *J. Biomed. Mat. Res.* **2000**, *52*, 346–353.

28 Kim, G.; van den Boogaart, M. and Brugger, J. *Microelectron. Eng.* **2003**, *67*, 609–614.

29 Diagnostic Systems Laboratories, Inc. Ultra-sensitive CRP assay No DSL-10-42100 http://www.dslabs.com/kits, accessed August 2007.

30 Hosokawa, K.; Omata, M. and Maeda, M. *Anal. Chem.* **2007**, *79*, 6000–6004.

31 Hofmann, O.; Wang, X.; Cornwell, A.; Beecher, S.; Raja, A.; Bradley, D.D.C.; Demello, A. J. and Demello, J. C. *Lab Chip* **2006**, *6*, 981–987.

32 Chabinyc, M. L.; Chiu, D. T.; McDonald, J. C.; Stroock, A. D.; Christian, J. F.; Karger, A. M. and Whitesides, G. M. *Anal. Chem.* **2001**, *73*, 4491–4498.

33 Zimmermann, M.; Hunziker, P. and Delamarche, E. in preparation.

3. Replication of High Aspect Ratio Pillar Array Structures in Biocompatible Polymers for Tissue Engineering Applications

C. Padeste[a], H. Özçelik[b,c], J. Ziegler[a], A. Schleunitz[a], M. Bednarzik[a],

D. Yücel[b,c,d], V. Hasırcı[b,c]

[a] Lab. for Micro- and Nanotechnology, Paul Scherrer Institut, 5232 Villigen PSI, Switzerland

[b] METU, BIOMAT, Department of Biological Sciences, Ankara 06531, Turkey

[c] European Institute of Excellence on Tissue Engineering and Regenerative Medicine, Ankara 06531, Turkey

[d] METU, Central Laboratory, Molecular Biology and Biotechnology R&D Center, Ankara 06531, Turkey

J.Z. developed and improved the process to replicate high aspect ratio molds in PLLA, fabricated the PLLA replicates and imaged them using optical and scanning electron microscopes.

3.1 Keywords

replication, pillar arrays, PDMS, PLLA, solvent casting, cell growth, cell alignment

3.2 Abbreviations

BSA, bovine serum albumin; **ICP**, inductive coupled plasma; **NSC(s)**, neural stem cell(s); **PBS**, phosphate-buffered saline; **PDMS**, polydimethylsiloxane; **PI**, Propidium iodide; **PLLA**, poly(L-D,L-lactic acid); **RF**, radiofrequency; **RIE**, reactive ion etching; **SEM**, scanning electron microscopy

3.3 Abstract

We developed a simple two-step replication method to transfer arrays of high aspect ratio nanopillars into films of poly(L-D,L-lactic acid) (PLLA). Such structures are promising model surfaces for tissue engineering applications. From arrays of 1 μm high and 200 nm wide pillars produced with e-beam lithography and reactive ion etching negative replicas were first formed by polydimethylsiloxane (PDMS) casting. The final replicates were produced by solvent casting from 1-4 % solutions of PLLA in chlorinated solvents on the PDMS templates. The silicon masters provide excellent stability and reusability, whereas the flexibility and low surface energy of the PDMS are necessary for the separation of the casts made with PLLA, a brittle material which is difficult to handle. AFM and SEM characterizations confirmed a high fidelity reproduction of the structures with aspect ratios of 1:5. *In vitro* tests using mouse neural stem cells seeded on nanopillars showed that the cells sense the nano-sized topography and respond accordingly by orienting themselves.

3.4 Introduction

High aspect ratio structures are promising model systems to study the influence of well defined features on cell growth. In particular, structures in the size range of 100 nm to 10 μm appear important for the control of migration, adhesion and cytoskeletal organization of a range of cell types [1-3]. Understanding size effects on such length scales is fundamental for cell biology and tissue engineering. Recent studies include the measurement of forces implied by cells to randomly distributed silicon nanowires grown perpendicular to a substrate surface [4].

The technology to produce well defined structures, e.g. in silicon substrates, of dimensions interesting for studying interactions with cells is well established, but the production of high aspect ratio features of reproducible quality is still a challenge. Furthermore, to make such structures attractive for cell growth studies they need to be replicated in high numbers into biologically relevant materials.

Polydimethylsiloxane (PDMS), casting is a suitable method to produce replicates from surface topographies. Due to the elasticity and the low surface energy the detachment from structured surfaces is relatively simple and works with a resolution down to the nanometer scale [5, 6]. However, due to the material properties, PDMS casts are of little interest to be used in cell growth studies, but they are well suited as intermediate replicates to obtain desired structures in other polymeric materials. For example, casting of liquid polymers into a PDMS mold followed by UV-induced curing was used to replicate high aspect ratio microstructures produced with deep x-ray lithography [7]. Furthermore, PLLA was pressed into a PDMS mold above its glass transition temperature of 180 °C to yield microstructured surfaces for cell growth experiments [8].

Here we present a two step casting replication process with the intention to provide model surfaces for cell-growth studies made from biodegradable polymers. While the first replication step is a conventional PDMS casting to produce an intermediate replicate from the microfabricated master structure, the second replication step is done by polymer casting from a solution pipetted onto the PDMS replica. This step takes advantage on the one hand of the solubility of various polymers including PLLA and PLGAs in chlorinated organic solvents such as dichloromethane, and on the other hand of the ability of PDMS moulds to absorb significant amounts of such solvents. The penetration of the solvent of the polymer into the PDMS facilitates the formation of a compact film of polymer along the PDMS surface, finally leading to very high reproduction fidelity of the sub-μm sized features.

Modification of surfaces through the production of nanoscale surface features is attractive for many *in vitro* and *in vivo* biomaterial applications including regenerative medicine, tissue engineering, medical implants, cell-based sensors, high throughput arrays and also for our understanding of fundamental cell biology. In this study the response of mouse neural stem cells to ordered surface topography fabricated from PLLA was investigated.

3.5 Materials and Methods

3.5.1 Master Fabrication

Hole arrays in a 320 nm PMMA resist (M_r=600'000) spin coated onto a silicon wafer were produced using an e-beam lithography system (Vistec EPBG 5000+ RH) operated at 100keV. Thermal evaporation of 30 nm of chromium and lift-off was used to produce a hard mask for the subsequent silicon etching step, which was performed on a reactive ion plasma etcher (Oxford Plasmalab System ICP 180) using SF_6 and C_4F_8 etching chemistry. A fluorosilane based antisticking layer was applied to the silicon master according to published procedures [9].

3.5.2 PDMS Replication

PDMS (Sylgard 184, Dow Corning) was prepared according to the manufacturers recommendations and repeatedly degassed during 20 minutes in vacuum in order to remove air bubbles formed during the mixing process. The polymer was poured onto the master structures placed in a petri dish until a thickness of about 3-5 mm was reached. The PDMS was cured for 3 hours at 70°C and then gently detached from the pillar arrays.

3.5.3 Preparation of the PLLA Replica

50 to 100 μL of a 2% (w/v) solution of poly(L-D,L-lactic acid) (PLLA) (70:30, inherent viscosity: 5.5–6.5 dL/g) in chloroform or dichloromethane (CH_2Cl_2) were pipetted onto the PDMS molds. After slow evaporation of the solvent over a period of 24 h the films formed were peeled off.

3.5.4 *in vitro* studies

PLLA films with the nanopillar arrays were sterilized with ethyl alcohol (70% v/v). The films were then treated with 50 μg/mL fibronectin dissolved in PBS buffer and incubated at RT for 45 min. BalbC neural stem cells (NSCs) were

provided by ATCC (CRL9392). Passages 5-8 were used for *in vitro* studies. NSCs were seeded at a density of 20.000 cells/cm² on the fibronectin coated films and cultured at 37ºC and 5% CO_2 in a humidified incubator. After 2 days of culture the cells were fixed with 4% paraformaldehyde for 10 min. Cell membranes were permeabilized with a 1% Triton X-100 solution for 5 min at RT, blocked with 1% bovine serum albumin (BSA) in PBS and incubated in FITC-Phalloidin (1:100 in 0.1% BSA) for 1 h to stain the actin filaments of the cells followed by staining of the nuclei with Propidium iodide (PI) at 1:2000 dilution for 5 min. Samples were analyzed by fluorescence microscopy and scanning electron microscopy (SEM). For SEM observations, cells were fixed with glutaraldehyde (2.5 % in 0.1M cacodylate buffer, pH 7.4), freeze-dried and coated with 10 nm Au/Pd.

3.6 Result and Discussion

3.6.1 Master Fabrication

   Patterns with combinations of inter-pillar distances of 1 μm, 1.5 μm, 2 μm, 5 μm and 10 μm arranged in an orthogonal matrix of 5 x 5 areas, each of 2 x 2 mm² in size, were produced using e-beam lithography. Samples of such dimensions are ideal to observe a high number of cells cultured on one single sample with a whole series of different topographical parameters. In order to optimize the writing speed of the E-beam lithography process we used a single shot exposure strategy, in which the defocus of the beam is optimized to obtain single features of 200 nm in diameter. After development of the exposed PMMA, a 30 nm thick chromium layer was deposited on the patterns, followed by lift-off in acetone. The samples were subjected to reactive ion etching (RIE). Parameters used to optimize the etching depth and the sidewall angle were etching time, supplied power of RF (radiofrequency) and ICP (inductive coupled plasma) while the SF_6 to C_4F_8 ratio was kept constant at 1:2.5. This ratio yields sidewall angles of less than 3°, which was requested to support the PDMS demolding after casting.

   An issue which had to be solved was the selectivity for pattern transfer of the chromium mask into silicon. Erosion of the 30 nm thick mask limits the
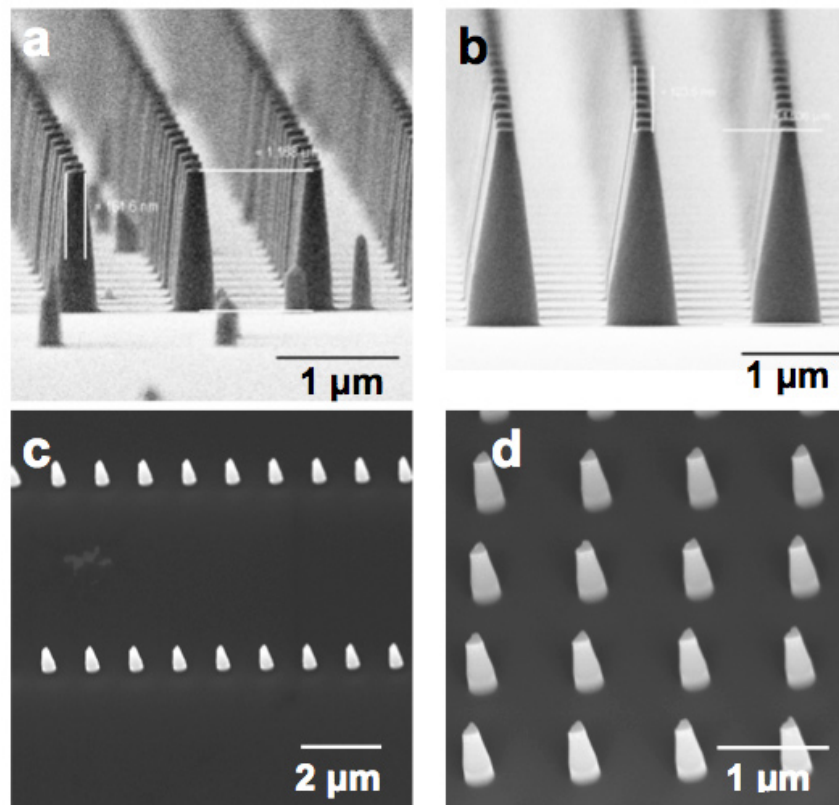
Figure 1.   SEM micrographs of examples of silicon pillar arrays with different inter-pillar distances produced with e-beam lithography and reactive ion etching. The height and shape of a pillar is dependent on the etching process parameters. Pillars shown in c) and d) were selected for further studies.

maximum achievable aspect ratio. Furthermore it leads to re-deposition of chromium, which causes the formation of additional nanotips in the area between the pillars (Figure 1a). By lowering RF and ICP power and increasing the etching time, we achieved arrays of nanopillars with conical shape and heights of up to 1.5 μm without micromasking effects caused by abrasion and re-deposition of chromium (Figure 1b). The process could be applied to whole 4 inch silicon wafers. For replication processes and biological studies we selected samples with a pillar height of 1 μm (Figure 1c and 1d).

3.6.2 Replication Steps

Replication of structures in PDMS is well established since many years and has been used to replicate surface features down to the nano-scale. The PDMS pre-polymer mixed with a curing agent is poured onto the structure to be replicated. This viscous mixture is well adapting to the surface features before it is heated to the curing temperature. In order to facilitate the detachment of the cured replicate from the substrate a fluorosilane coating was applied to the surface of the silicon master. The detachment of the replicate indeed proved to proceed very easily without implying much force onto the nano-pillars, as optical inspection of the used masters showed intact arrays of pillars.

The second replication step is relying on ability of PDMS to absorb considerable amounts of chlorinated solvents. This ability is evident from experiments which we carried out with pieces of PDMS immersed in CH_2Cl_2. After 90 minutes they showed a size increase of 21% in each direction (i.e. 75% increase in volume) and weight gain of 100%. This swelling is perfectly reversible upon evaporation of the solvent at ambient conditions for several hours.

When 50-100 μl solutions of PLLA were deposited the structured surface of the polymer cast a slight bending due to solvent uptake of the cast was observed. This solvent uptake appears to be beneficial for the replication. It leads to an increased polymer concentration at the interface of the polymer solution and the PDMS, as only the solvent, but not the dissolved polymer, can enter the PDMS network. It proved to be advantageous to slowly let the solvent evaporate for at
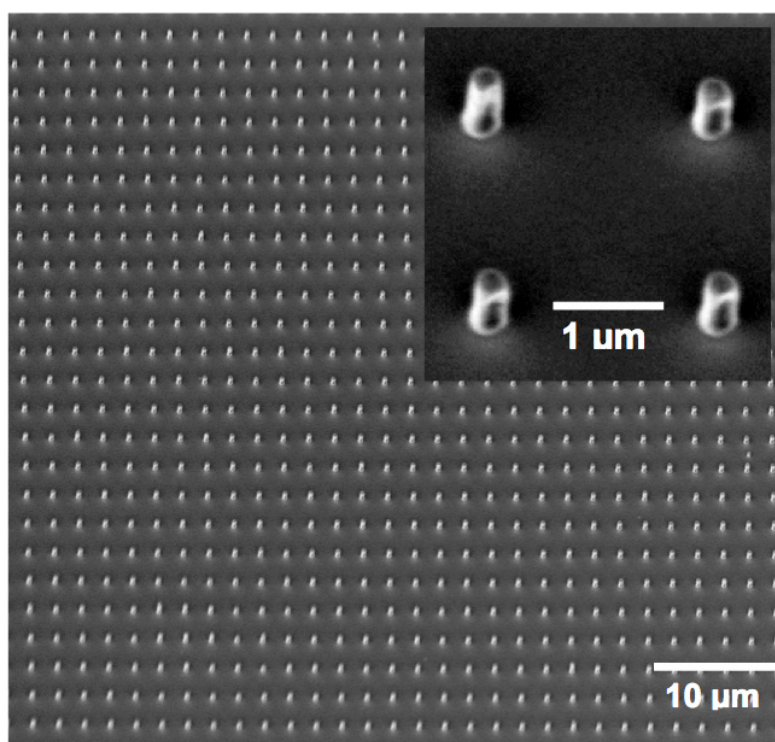
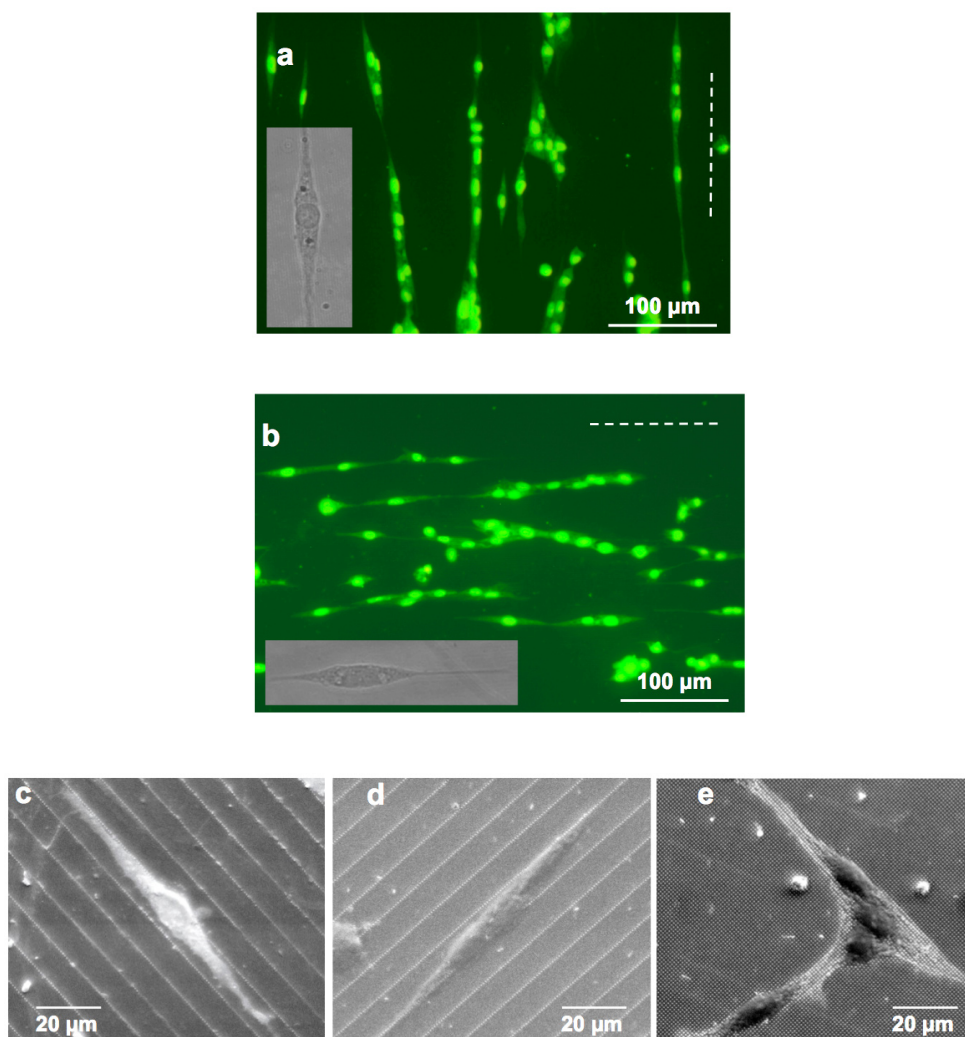**Figure 2.**   SEM images of nanopillar structures replicated in PLLA

Figure 3.   (a, b) Fluorescence micrographs of FITC-Phalloidin and PI stained NSCs on the nanopillar patterns showing the alignment of the cells in different fields of the PLLA film. Dashed lines indicate the orientation of the nanopillars. Inset images were obtained by light microscopy. SEM images of the same arrays indicate that cells are guided along the direction with the most densely packed pillars (c,d). When the pillars were symmetrically distributed 1 μm apart, then the cells were unable to orient and align (e).

least 24 hours to obtain compact polymer layers and a reproducible detachment of the thin films with the replicated pillars. While optical microscopy was used to explore the number of defects in the replicated structures, the fidelity of the replication was assessed by SEM (Figure 2). Very few pillars were missing in the replicated arrays and the size and height was found to be very close to the master structures, as confirmed by AFM measurements. Preliminary experiments showed that the process can be transferred to further polymers if they are soluble in chlorinated solvents. Of particular interest are copolymers of the type poly(lactic-co-glycolic acid) (PLGA) which are biodegradable and biocompatible.

3.6.3 *in vitro* studies

In the initial *in vitro* experiments the reaction of mouse neural stem cells on the replicated PLLA nanopillar structured films were tested. From experiments with BalbC NSCs on polystyrene tissue culture plates it was known that a coating with fibronectin is required for the NSCs to adhere to the surface. Therefore, PLLA films used in this study were coated with fibronectin prior to cell seeding.

Micrographs of NSCs cultured on the structured films revealed a strong effect by the interpillar distance on cell response, as exemplified in Figure 3. Cells tried to locate in between the pillars if the distance in any direction was ≥ 5 µm. When one of distances in x and y direction was ≥ 5 µm and the other ≤ 5 µm the orientation of the cells was always in the direction of the shorter pillar-to-pillar distance. No distinct orientation was observed when the pillars were only 1-2 µm apart in both directions. These preliminary *in vitro* studies using NSCs showed that the nanotopography of PLLA films replicated by the presented two step procedure has a significant effect on cell growth.

3.7 Conclusions

We presented a two-step replication process for the production of model systems for tissue engineering applications using biocompatible and biodegradable polymers. The use of a negative intermediate template of PDMS for solvent casting of biocompatible polymers soluble in chlorinated solvents allows high fidelity reproduction of high aspect ratio structures. In particular, structured surfaces of polymers of the PLLA and PLGA family can be reproduced in large quantities from re-usable high-quality masters. The presented replication method is simple and can be performed without the need of specific microfabrication facilities to produce well defined nanostructures. First studies showed that cells respond to topography especially if the texture is in the micro- to nanometer-range.

3.8 Acknowledgment

3.9 References

1   Bettinger, C.; Langer, R. and Borenstein, J.T. *Angew. Chem. Int. Ed.* **2009**, *48*, 5406.

2   Martinez, E.; Engel, E. and Planell, J.A. *Ann. Anat.* **2009**, *191*, 126.

3   Cyster, L.A.; Parker, K.G.; Parker, T.L. and Grant, D.M. *Biomaterials* **2004**, *25*, 97.

4   Li, Z.; Song, J.; Mantini, G.; Lu, M.Y.; Fang, H.; Falconi, C.; Chen, L.J. and Wang, Z.L. *Nano Letters* **2009**, *9*, 3575.

5   Ye, X.; Liu, H.; Ding, Y.; Li, H. and Lu, B. *Microelectron. Eng.* **2009**, *86*, 310.

6   Zorlutuna, P.; Rong, Z.; Vadgama, P. and Hasirci, V. *Acta Biomater* **2009**, *5(7)*, 2451.

7   Perennes, F.; Marmiroli, B.; Tormen, M.; Matteucci, M. and Di Fabrizio, E. *J. Microlith., Microfab., Microsyst.* **2006**, *5*, 011007.

8   Davidson, P.M.; Ozcelik, H.; Hasirci, V.; Reiter, G. and Anselme, K. *Adv. Mater.* **2009**, *21*, 3586.

9   Schift, H.; Saxer, S.; Park, S.; Padeste, C.; Piles, U. and Gobrecht, J. *Nanotechnology* **2005**, *16*, 171.

4. Connecting μ-Fluidics to Electron Microscopy

Simon Kemmerling[1], Jörg Ziegler[1], Gabriel Schweighauser[1], Stefan A. Arnold[1], Dominic Giss[1], Shirley Müller[1], Philippe Ringler[1], Kenneth N. Goldie[1], Niels Goedecke[2], Andreas Hierlemann[2], Henning Stahlberg[1], Andreas Engel[1,3], Thomas Braun[1]

[1] Center for Cellular Imaging and Nanoanalytics (C-CINA), Biozentrum, Universität Basel, Basel, Switzerland

[2] Bio Engineering Laboratory (BEL), Departement of Biosystems Science and Engineering (D-BSSE), ETHZ, Basel, Switzerland

[3] Department of Pharmacology, Case Western Reserve University, Cleveland, USA

4.1 Keywords

electron microscopy, micro fluidics, single molecule analysis, mass and shape, systems biology

4.2 Abbreviations

AF, appoferritin; **AM6.5**, ammonium molybdate at pH 6.5; **BHK**, baby hamster kidney; **ddH$_2$O**, double-distilled water; **EM**, electron microscopy; **ET**, electron tomography; **MPL,** mass-per-length; **MS** mass spectrometry; **NanoV$_{8.0}$**, NanoVan at pH 8.0; **NanoW$_{6.8}$**, NanoW at pH 6.8; **PTA$_{7.0}$**, phosphotungstic acid at pH 7.0; **SD**, standard deviation; **STEM**, standard deviation scanning transmission electron microscopy; **TEM**, transmission electron microscopy; **TMV**, tobacco mosaic virus; **UA$_{4.5}$**, uranyl acetate at pH 4.5; **UA$_{7.0}$**, uranyl acetate at pH 7.0

4.3 Abstract

A versatile methodology for electron microscopy (EM) grid preparation enabling total content sample analysis is presented. A microfluidic-dialysis conditioning module to desalt or mix samples with negative stain solution is used, combined with a robotic writing table to micro-pattern the EM grids. The method allows heterogeneous samples of minute volumes to be processed at physiological pH for structure and mass analysis, and allows the preparation characteristics to be finely tuned.

4.4 Introduction

Systems biology aims to quantify the molecular elements of a biological system, to determine their interactions and to integrate this information into network models[1]. The development of comprehensive models requires experimental information about the spatial and temporal arrangements of the network components as well as their structure, a challenge that required a multi-resolution approach and the combination of different techniques[2,3]. Cryo-electron tomography (cryo-ET) is the ultimate technique to reveal the spatial organisation of protein structures and macromolecular complexes in single cells[4,5]. Currently cryo-ET is restrained by several limitations, such as the size of the cell that can be analysed (maximum diameter of ~2 μm)[6], and by problems in data segmentation and in the template matching required for protein recognition (restricted to relatively large protein complexes)[7]. Indeed, many target structures can only be recognised if labelled with electron-dense markers (e.g., gold labels)[8], which, despite recent progress[9], often involves harsh preparative treatment of the cells. Furthermore, while ET delivers structural and spatial information, correlation of these with other methods such as mass spectroscopy (MS)[10] is difficult. A complementary approach is to physically lyse the cells and to subsequently write the entire sample onto electron microscopy (EM) grids for structure analysis by transmission EM (TEM), or mass analysis by scanning TEM (STEM). Ultimately, the use of microfluidic techniques offers the potential to analyse a single cell by making it possible to investigate protein ultrastructures and membrane fragments in lysates[11].
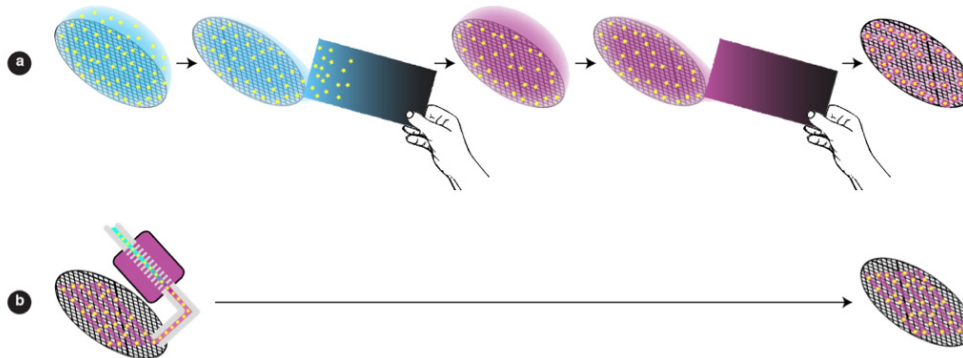
Figure 1. Schema of negative staining methods for EM. (a) Classical negative staining by hand: The sample is absorbed to the carbon film of an EM grid and the grid is blotted to remove excess sample solution. The absorption time and the specific absorption properties of the sample components determine the fraction of the sample that is immobilised. A wash and blot cycle sometimes follows (not shown). The grid is then incubated with the negative stain solution of choice, followed by another blotting step to remove excess stain solution. The grid is left to air-dry before investigation in the electron microscope. This method only immobilises a fraction of the sample on the grid. (b) The here developed microfluidic negative staining approach: A very small amount (0.1–0.3 μl) of stain-mixed sample is applied to the grid via a nozzle of 50 μm inner diameter. The grid is then air-dried without any blotting. With this method the entire sample is immobilised on the grid. Additionally, the micro-precision of the writing process allows a meander-type micro-pattern of stained sample to be created on the carbon film.

Here we present a lossless sample deposition method for EM (Figure 1), which allows the handling of minute sample volumes and immobilisation of the total sample content on EM grids to obtain, for example, the full cell inventory. This methodology is combined with a microfluidic sample-conditioning module. The constellation provides a new staining technique for heavy metal salts (negative stain) for TEM as well as specific desalting for mass measurements by STEM.

4.5 Materials and Methods

4.5.1 Stain Preparation

The reservoir of the sample-conditioning module (Figure 2a) was filled with various commonly used negative stains prepared in the following way: phosphotungstic acid ($PTA_{7.0}$): sodiumphosphotungstate tribasic hydrate (Riedel-de Haen, Switzerland) was dissolved in double-distilled water (ddH_2O) to give a 1% or 2% (w/v) final concentration. The pH of the aqueous solution was adjusted to 7.0 using 1 M potassium hydroxide; ammonium molybdate ($AM_{6.5}$): ammonium molybdate (Aldrich, Switzerland) was dissolved in ddH_2O to give an aqueous solution with a final concentration of 0.5% (w/v) at pH 6.5; NanoVan® ($NV_{8.0}$): the 2% ready to use methylamine vanadate (Nanoprobes, USA) solution at pH 8.0 was diluted with ddH_2O to give a final concentration of 1% (w/v); NanoW® ($NW_{6.8}$): the 2% ready to use methylamine tungstate (Nanoprobes, USA) solution at pH 6.8 was diluted with ddH_2O to give a final concentration of 1% (w/v); uranyl acetate ($UA_{4.5}$): uranyl acetate was dissolved in ddH_2O to give a final concentration of 0.25% (w/v) at pH 4.5; buffered uranyl acetate ($UA_{7.0}$): to prepare UA at pH 7, the above 0.25% (w/v) uranyl acetate solution was mixed with an equal volume of a 20 mM oxalic acid solution. The pH was adjusted using 3% ammonium hydroxide, added slowly while stirring[12]. This resulted in a 0.12 % UA solution at pH 7.0.

4.5.2 Test samples

Several samples were used for the initial tests and as a proof of concept: the chosen test samples apoferritin (AF; from equine spleen; Sigma, Switzerland) and tobacco mosaic virus (TMV; kindly supplied by Ruben Diaz-Avalos, New York Structural Biology Center, USA) are well characterised, and TMV is used as a standard for mass calibration in scanning transmission electron microscopy (STEM). The used test-samples were composed as follows: (1) A mixture of 0.05 mg/ml AF and 0.1 mg/ml TMV in phosphate buffered saline pH 7.4 (PBS; P4417, Sigma–Aldrich, Switzerland). (2) 0.05 mg/ml AF in PBS. (3) 0.1 mg/ml TMV in quartz-ddH2O. (4) Baby Hamster Kidney (BHK) cell lysate in PBS (see the next section).

4.5.3 BHK cell culture and lysis

Attached Baby Hamster Kidney (BHK21; ECACC 85011433) cells were grown for 48 h in a polystyrene T75-flask containing 30 ml of DHI-5 medium (see end of section) at 37 °C, 100% air humidity, and 5% CO_2. To harvest the cells the medium was removed and the flask was washed with 7 ml of PBS. To detach the cells from the flask surface, 3 ml of trypsin–EDTA were added and the cells were incubated for 5 min at 37 °C. Afterwards, 7 ml of DHI-5 medium were added and the detached cells were mixed using a pipet. A 0.5 ml of the cell suspension was left in the flask and again incubated with 30 ml of fresh media for 48 h to obtain the next batch. The rest of the cell suspension was centrifuged twice and washed with PBS (48g, 2 min). The pellet was dissolved in 2 ml of PBS. In an Eppendorf tube, 200 μl of this cell suspension were further diluted with 800 μl of PBS and the cells were lysed by sonification for 2 min at 25 kHz while cooling.

DHI-5 medium is a mixture of DME (Dulbecco's Modified Eagels Medium; D6171, Sigma, Switzerland), HamF12 (Nutrient Mixture F-12Ham; N8641, Sigma, Switzerland), and IMDM (Iscove's Modified Dulbecco's Medium, I3390, Sigma, Switzerland) media (1:1:2), supplemented with 5% FCS (Foetal Bovine
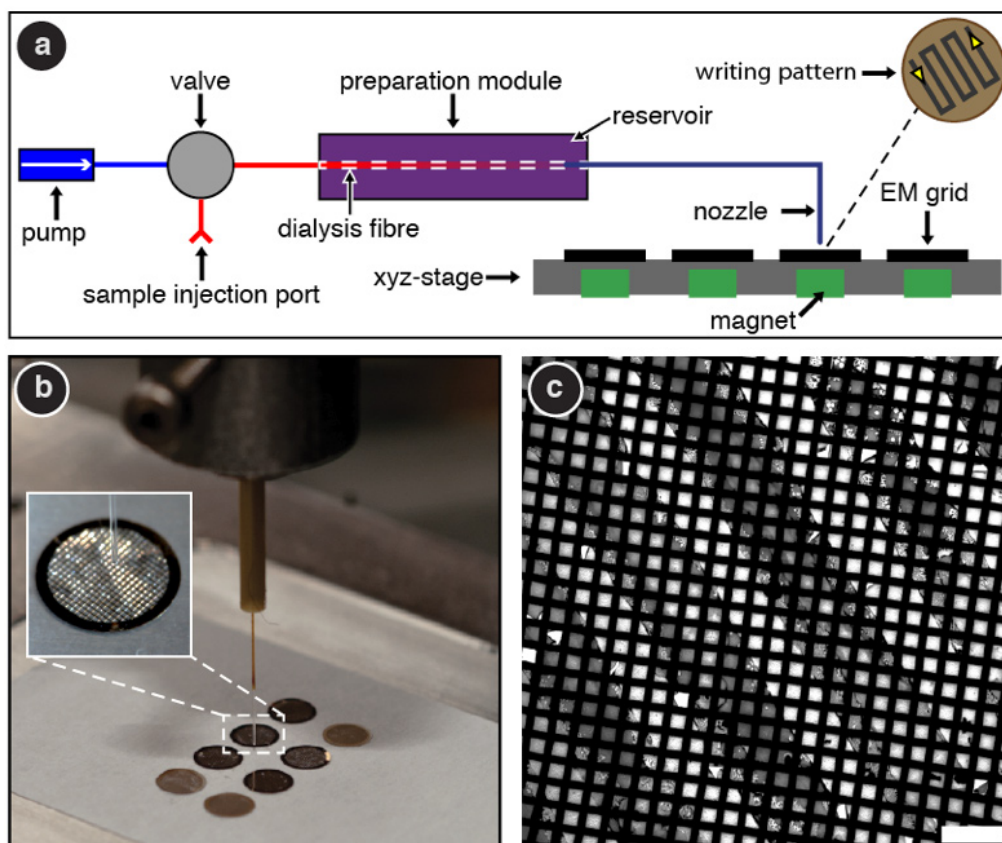
Figure 2. Sample-conditioning module and micro-patterning device. (a) Schematic representation of the main components and the meander-type writing pattern. (b) Nozzle positioned above an EM grid on the xyz-stage. Inset: enlarged view; the arrow indicates the nozzle tip. (c) TEM image of a micro-patterned grid showing a section of the six 200–300-μm-wide lines of a $PTA_{7.0}$ stained sample (diagonal dark grey lines) written on an EM grid (black) and the empty carbon film in between (light grey). Scale bar: 200 μm.

Serum, E7524, Sigma, Switzerland) and complemented with nonessential amino acids (MEM nonessential amino acid solution, M7145, Sigma, Switzerland), L-glutamine (L-glutamine solution, G7513, Sigma, Switzerland), and vitamins (RP-MI1640 vitamins solution, R7256, Sigma, Switzerland).

4.5.4 Microfluidic setup

Samples were specifically treated and then deposited on carbon films covering 200 and 400 mesh Ni-TEM grids or on the special grids used for mass measurement (see below). This was achieved using a custom-built modular microfluidic setup (Figure 2a) consisting of a syringe pump, a 10-port 2-position valve, a custom-built sample conditioning module, a custom-built hand-over module, with functionalised nozzle, xyz-stage and several HPLC consumables (fused silica capillaries, PTFE tubing and connectors; BGB-analytic, Switzerland). The whole system is driven by the syringe pump (KDS210; Ismatec SA, Switzerland) and the sample is injected via a sample loop on the valve (Valco 10-port 2-position valve; BGB-analytic, Switzerland). All electronic components of the apparatus are controlled by a LabView-based custom-made software system (Supplementary Figure 1), which features a macro language for flexible automation by coordination of the different modules. On request we will provide the software and the construction plans.

4.5.5 Sample-conditioning module

The sample-conditioning module consists of a custom-built reservoir that holds about 5 ml of solution (dialysis reservoir); either stain solution (for negative stain TEM) or 100 mM ammonium acetate prepared using quartz-ddH$_2$0 (desalting). About 10–12 cm of a 13 kDa cut off cellulose fibre (Spectra/Pro® microdialysis fibres ID = 200 μm; Spectrum Laboratories, USA) that holds 3–4 μl of sample at one time spans this reservoir. When the sample is pumped through this conditioning module at a rate of 2 μl/min, the dialysis time is about 2 min.

4.5.6 Hand-over module and grid preparation

The hand-over module deposits sub-microlitre sample volumes on EM grids by contact writing and can be programmed to automatically prepare a series of grids. The Ni-TEM grids are held in place by magnets and their carbon films are activated with atmospheric pressure helium cold-plasma (piezobrush® PZ1, Polyscience AG Switzerland) immediately before sample application. Initial tests showed that a 4 s treatment at a distance of 1 cm from the plasma source gives comparable results to the conventional glow discharge[13], without destroying the carbon film. A fully controllable micro-mechanical device (Physik Instrumente xyz micro-precision translation stages; Dyneos AG, Switzerland) brings a thin nozzle that is connected by micro-capillaries to the sample-conditioning module, in close proximity to the EM grid (Figure 2b). After liquid contact, the grids are moved under the nozzle with sub-micrometre precision to create a micro-pattern of the sample on carbon in the form of a thin wet film. In this way 0.1–0.3 μl of stained or specifically desalted sample are 'written' on the grid, which is then air-dried. The degree of wetting obtained can be tuned by modifying the plasma treatment, and the writing can be optimised for the sample by adjusting the writing parameters. A defined combination of grid hydrophobicity (defined by plasma treatment parameters), writing speed, and surface tension of the applied solution (can be changed by the addition of ethanol traces), allowed a continuous line about 13 mm long and 200–300 μm wide to be written (Figure 2c).

4.5.7 Nozzle preparation

Commercially available fused silica capillaries (Polymicro) were used to make the nozzles. These were processed in the following way to optimise the liquid handling and direct the fluid onto the EM grids. The first 0.5–1.0 cm of the polyimide coating of the fused silica capillaries was stripped away using hot chromosulfuric acid[14]. Afterwards, the nozzle was extensively rinsed with ddH$_2$0 to remove all traces of the acid. The fused silica was then cleaned by successively dipping the capillaries into ddH$_2$0, ethanol and acetone for 10min while shaking. Subse- quently, the fused silica surface was activated by a 1 min treatment with

cold atmospheric pressure helium plasma (piezobrush® PZ1, Polyscience AG, Switzerland). Immediately after plasma treatment the capillary tips were dipped into a silanisation solution (~5% dimethyldichlorosilane in heptane; silanisation solution 1, 85126, Fluka, Switzerland) for 1 h and baked at 90 °C for 4 h. The stripped and silanised capillaries have an inner nozzle diameter of 50 μm.

4.5.8 Scanning transmission electron microscopy

A Vacuum Generators (East Grinstead, UK) HB-5 STEM interfaced to a modular computer system (Tietz Video and Image Processing Systems) was used. All samples were prepared on thin carbon films spanning gold sputtered, carbon-coated, 200-mesh-per-inch, gold-plated copper grids (STEM microscopy grids)[15]. The aim was to determine whether samples leaving the microfluidics setup were clean and suitable for mass evaluation. After extensive rinse cycles for maintenance of the set-up, the sample dialysis reservoir was filled with quartz–ddH$_2$O. A stock solution of TMV in quartz–ddH$_2$O was then passed through the conditioning module (micro-dialysis time of 2 min) and written to STEM microscopy grids by the hand-over module. The control grid, which also served as mass standard, was manually prepared in the conventional manner, i.e., a 5 μl droplet of the same TMV stock was adsorbed to a STEM grid, blotted and washed on eight droplets of 100 mM ammonium bicarbonate solution prepared with quartz–ddH$_2$O, blotting after each step. All grids were allowed to air-dry. Series of digital 512 × 512 pixel, dark-field images were recorded from the grids at an acceleration voltage of 80 kV and a nominal magnification of 200,000×. The recording dose used varied between 290 and 635 electrons/nm^2. The images were evaluated with the MASDET program package as described previously[16]. All mass-per-length (MPL) data were corrected for beam-induced mass-loss. The results from the control grid (mass standard) gave the instrumental scale factor, which was correspondingly applied to all measurements. The MPL data from the test grid were binned into a histogram and described by a Gaussian curve. The average MPL and standard deviation (SD) were also calculated and compared to the expected value of 133 kDa/nm^2, and to the SD of the control grid results, respectively[15].

4.6 Results

The apparatus enables micro-patterning of EM grids with stained or desalted samples. It consists of two main units, (a) a sample-conditioning module for staining or desalting (or an inline combination of both), and (b) a hand-over module for micro-patterning the sample onto the grids (Figure 2a). The instrument is designed for a prospective degree of automation and controlled by custom-written software (Supplementary Figure 1). In the first step the sample is conditioned using the micro-dialysis principle. This method was chosen because it is easy to integrate and because of its multiple application potential. In this sample-conditioning module, the sample flows through a cellulose fibre capillary (13 kDa cut-off) that extends through a reservoir of either negative stain solution or a volatile buffer (e.g., ammonium acetate or ammonium bicarbonate) in quartz double-distilled water (ddH$_2$O). Dialysis occurs as the sample liquid flows through the chamber, to either add the negative stain solution or remove undesired salts. The sample flow rate defines the dialysis time and can be adapted in a range from seconds to minutes. Liquid contact writing is then used to deposit the sample on EM grids supporting a thin carbon film that was rendered partially hydrophilic by activation with an atmospheric pressure helium cold-plasma. This treatment replaced the conventional glow discharge technique[13]. Piezo-driven plasma generation was chosen, as it is easier to integrate in an automated setup. The hand over unit is a micro-mechanical positioning device that brings a thin nozzle in close proximity to the grid. After liquid contact has been established, the grid is moved under the nozzle at sub-micrometre precision to create a meander-type micro-pattern of the sample on its carbon film (Figure 2b and c). When this is finished, the nozzle is quickly moved up and down as the next grid is positioned (the time required is operator defined; minimum 0.5 s). At present, a series of 26 grids can be written in sequence.

We have tested this new grid preparation method with a range of commonly used negative stains[17], namely phosphotungstic acid at pH 7.0 (PTA$_{7.0}$), ammonium molybdate at pH 6.5 (AM$_{6.5}$), NanoVan® at pH 8.0 (NanoV$_{8.0}$), NanoW® at pH

6.8 (NanoW$_{6.8}$), and uranyl acetate at pH 4.5 (UA$_{4.5}$) and pH 7.0 (UA$_{7.0}$), and compared the results with grids prepared by conventional negative staining/blotting methods. Due to the effective staining behaviour of this method only half or even less (2 min micro-dialysis against 0.5%–1%) of the stain solution concentrations normally applied were used. A mixture of tobacco mosaic virus (TMV) and apoferritin (AF) in phosphate buffer system (PBS; 10 mM phosphate buffer, 2.7 mM KCl, 137 mM NaCl, pH 7.4) was employed to investigate the staining quality (Figure 3 left column, and Supplementary Figure 2), while complete cell lysates of Baby Hamster Kidney (BHK) cells allowed the staining behaviour for heterogeneous samples to be assessed (Figure 3 right column, and Supplementary Figure 3). UA, one of the most commonly used negative stains employed in conventional negative stain EM, caused sample aggregation in our new method at both, pH 4.5 and pH 7.0 (Supplementary Figure 4) and was not investigated further. Uranyl formate was not considered for testing, as a similar fixative effect as for UA has been reported[17]. The other stains examined gave excellent results for both test samples. When used at significantly lower concentrations than in classical staining methods, these stains provided good contrast in the EM and clearly revealed structural details. With the exception of UA$_{4.5}$, all of the stains were stabilised at physiological or close to physiological pH. When BHK cell lysates were examined in an analogous procedure, ultrastructural details, such as membrane fragments packed with proteins, filaments and individual proteins were all clearly resolved in the TEM with no sign of aggregation (Supplementary Figure 5).

A STEM mass measurement achieves an accuracy of ±5–10% depending on the sample and, working from an image, directly links the mass data to shape information[11]. Initial tests made with TMV clearly showed that the modular microfluidic setup is capable of preparing the stringently clean grids required for these measurements (Figure 4a). The carbon film of the written, airdried grids of TMV in quartz–ddH$_2$O dialysed against quartz–ddH$_2$O was clean. Further, the mass-per-length measured for TMV was within 1.5% of that measured for the control grids, which were manually prepared in the conventional way and imaged in the same data acquisition session (Figure 4b). Mass measurements require the removal of all non-volatile buffer components[15]. The classic way to

do this specific desalting is to wash the grid several times with quartz–ddH$_2$O or a volatile buffer, e.g., ammonium acetate or bicarbonate, directly after sample adsorption. With the new grid preparation method, the required desalting is achieved before adsorption by dialysis. To avoid drastic pH changes and sample aggregation (Supplementary Figure 6), microdialysis can be done against a volatile buffer, which allows the pH to be kept as close as possible to physiological values at all stages. Changes in the lateral aggregation of TMV after dialysis against ammonium bicarbonate illustrate the effect, and document the efficiency of the sample-conditioning module (Supplementary Figure 6).

4.7 Discussion

Negative stain TEM is a standard method used in most electron microscopy laboratories involved in biology or biomedicine. In classical negative staining techniques for EM, a drop of sample (3–7 μl) is applied to the EM grid, which is then washed and stained. Each step is followed by a blotting procedure to remove excess liquid (Figure 1a). Consequently, only a fraction of the sample and the stain remains on the grid. The amount of sample remaining depends on the adsorption, washing and blotting times, is often not reproducible, and the relative particle densities on the grid may be distorted by preferential adsorption of specific sample sub-fractions. Instead, our newly developed method adds the stain via dialysis prior to immobilisation on the EM grid. Only 0.1–0.3 μl of the stain-mixed sample are required and no washing or blotting steps are involved (Figure 1b). This allows a much higher proportion (close to 100%) of the initial sample to be deposited on the EM grid, so that the true relative ratios between the different sample con- stituents are maintained (Supplementary Figure 7). Moreover the stain density is controlled by the heavy metal concentration in the reservoir and the flow rate and can be easily tuned (Figure 5).

In our hands, the automated procedure is more reproducible than manual staining, especially for "difficult" stains such as AM, NanoW® and PTA. This new method without any blotting or washing steps provides good contrast even for stains with weak electron scattering properties; the contrast is significantly
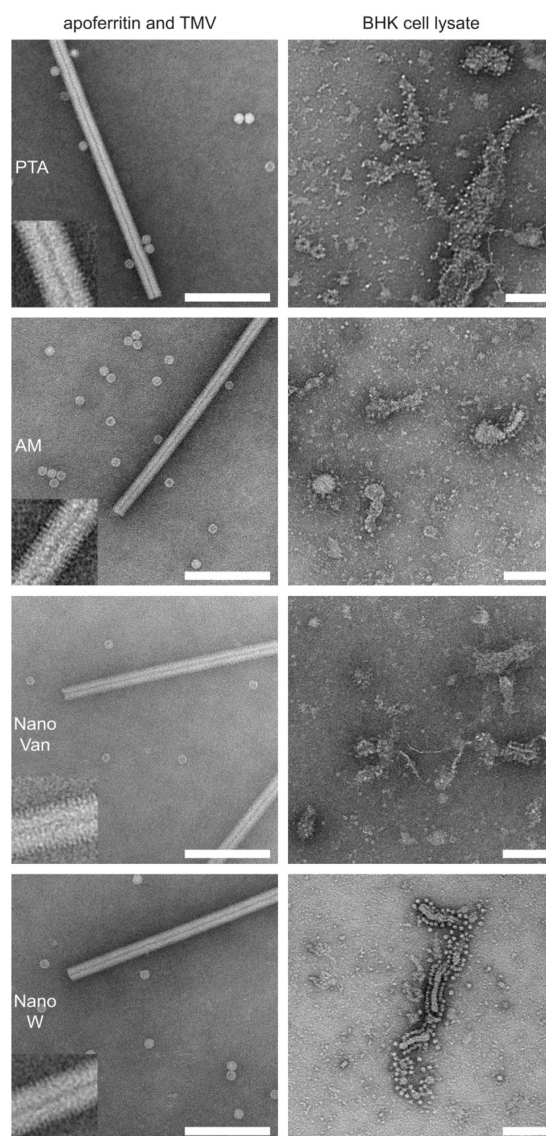
Figure 3. Gallery of TEM images. This selection shows TEM images of the two test samples prepared with the setup and different stains. (Left column) Mixture of AF and TMV. For all negative stains the central channel and the 23 Å repeat of TMV and the sub-structure of the AF is visible. (Right column) BHK cell lysate showing typical membrane structures with integrated membrane proteins that exhibit the shape of ATPases. (Rows) Samples in PBS were conditioned with 1% $PTA_{7.0}$, 0.5% $AM_{6.5}$, 1% $NanoV_{8.0}$, and 1% (left) or 2% (right) $NanoW_{6.8}$. Scale bars: 100 nm; insets depict three-fold enlarged regions of the TMV. (for more images see Supplementary Figure 2 and 3).the writing process allows a meander-type micro-pattern of stained sample to be created on the carbon film.

higher than that achieved manually. Furthermore, the stain seems to be homogenously distributed around the particles, a fact that might be important for subsequent data analysis steps, such as alignments. Both, the contrast and the stain distribution attained with low scattering stains, may be favourably influenced by the preincubation of the protein complexes before adsorption to the grid surface as the stain has more time to penetrate the fine structures of the proteins. However, the resolution still appears to be limited by the grain size of the stain. Visually, AM seems to exhibit an excellent balance be- tween stain grain size, contrast and "dynamic range" (Supplementary Figure 5c). Moreover, their tolerance to phosphate buffers, the most frequently used buffers in biochemistry and cell biology, and the possibility to adapt their pH makes AM and PTA applicable to a broad spectrum of samples.

In the future, the hand-over module will be developed to allow grid preparation for higher resolution techniques such as cryo-EM where the ice thickness is a critical, contrast-determining property. To this end, the grid temperature will be kept at the thaw point to avoid evaporation/condensation of the liquid during writing. Subsequently, the grid will be shot into liquid ethane. Alternatively, it will be freeze-dried to allow improved mass and shape measurements by STEM.

The microfluidic sample preparation platform presented here has the potential to become an important tool not only for systems biology but also for EM in general, which demands reproducible, quantitative sample grid preparation and assessment. The possibility of micro-patterning EM grids will allow a more systematic and convenient analysis of complex samples in the future. Combined with microfluidic methods for cell lysis, protein separation and labelling, this method for total cell content analysis for structure and mass offers the potential to optimally complement other experimental system biology techniques such as MS[18] and ET[19,20]. Importantly, the raw images must be analysed by feature matching methods[7,20,21] to obtain quantitative information. To aid the analysis, a visual library will be constructed containing the projections of a priori target molecules. The raw data images recorded from samples prepared in a lossless manner will be segmented by a hierarchical algorithm[22,23], and the various particles present classified according to their size and shape. Shape matching will

also allow the link to be made between negative stain and STEM images, combining the higher resolution and high contrast of the TEM projections with the mass obtained from unstained samples by STEM. Finally, crosscorrelation techniques will be used to assign the TEM projections to the most probable match in the visual library[20].

The outlined automated sample preparation technique opens the way for a new visual proteomics approach. Ultimately it will allow the total content of a single cell or miniscule tissue region to be examined by EM. It will then become possible to assemble complete ultrastructural libraries from cells or tissues. The method will make the structural study of the various cellular components on the single molecule level possible. We foresee this technique as a valuable tool to study complex biological systems, complementing other systems-biological methods.
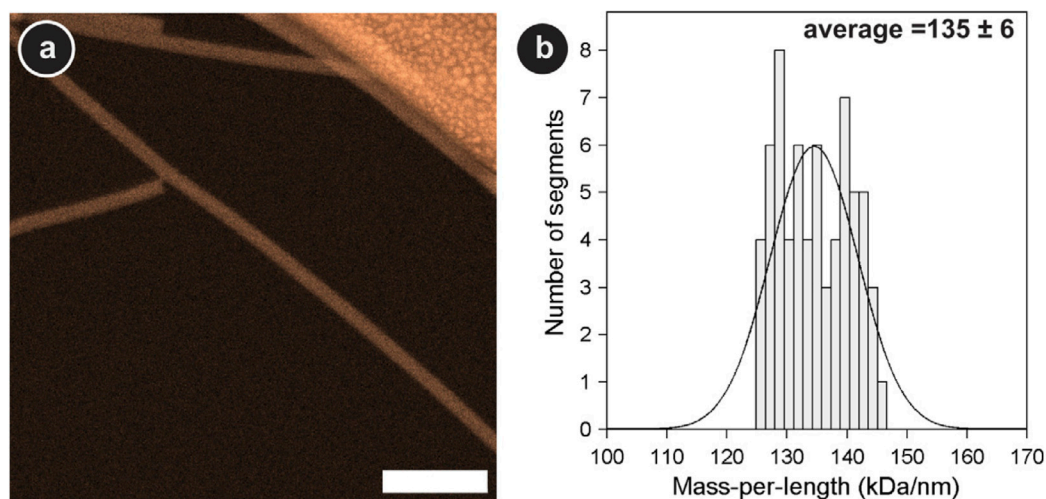
Figure 4.   Mass measurement of TMV by STEM to test the preparation quality and cleanliness delivered by the microfluidic setup. (a) STEM dark-field image of unstained, airdried TMV written on a STEM microscopy grid for mass measurement. TMV (0.1 mg/ml) in quartz–ddH$_2$O was dialysed against quartz–ddH$_2$O for 2 min in the sample-conditioning module and written onto the grid. The thin carbon film beneath the TMV rods is clean (uniform dark regions). A small segment of the gold-sputtered, perforated thick carbon layer supporting this film is also visible (bright irregular region upper right). (b) Mass-per-length histogram of correspondingly written TMV. After scaling according to the mass standard, the determined average mass-per-length, 135 ±6 kDa/nm, is within 1.5% of the expected value, 133 kDa/nm[15]. Further, the standard deviation of the data set is comparable to that of the mass standard, ±4 kDa/nm, which was prepared in the conventional way (see Section 2). Scale bar: 100 nm.
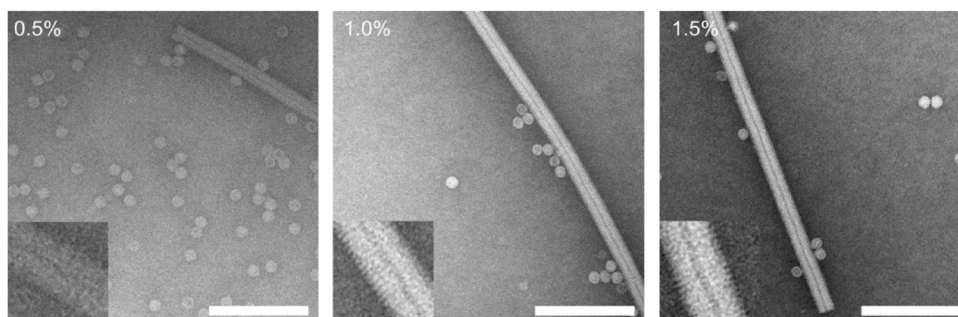
Figure 5. Fine-tuning of the stain density: representative images of samples conditioned with different PTA7.0 concentrations, clearly showing the different stain densities. The mixture of AF and TMV in PBS was conditioned with 0.5%, 1% or 1.5% of PTA$_{7.0}$. This demonstrates that easy and reproducible stain density fine-tuning is possible to adapt to different samples or to reveal different details of the same sample. Combined with several applicable stains with distinct properties, this offers the potential to individually optimise the staining for a certain sample or certain sample details. Scale bars: 100 nm; insets depict three-fold enlarged regions of the TMV.

4.8 Supplementary Figures

Supplementary Figure 1   Screenshot of the LabView-based control software

Supplementary Figure 2   Gallery of negatively stained test samples

Supplementary Figure 3   Gallery of negatively stained BHK lysate

Supplementary Figure 4   UA staining results

Supplementary Figure 5   Images of BHK cell lysate demonstrating the absence of aggregation

Supplementary Figure 6   TMV preparation for STEM

Supplementary Figure 7   Comparison of manual and automated grid preparation
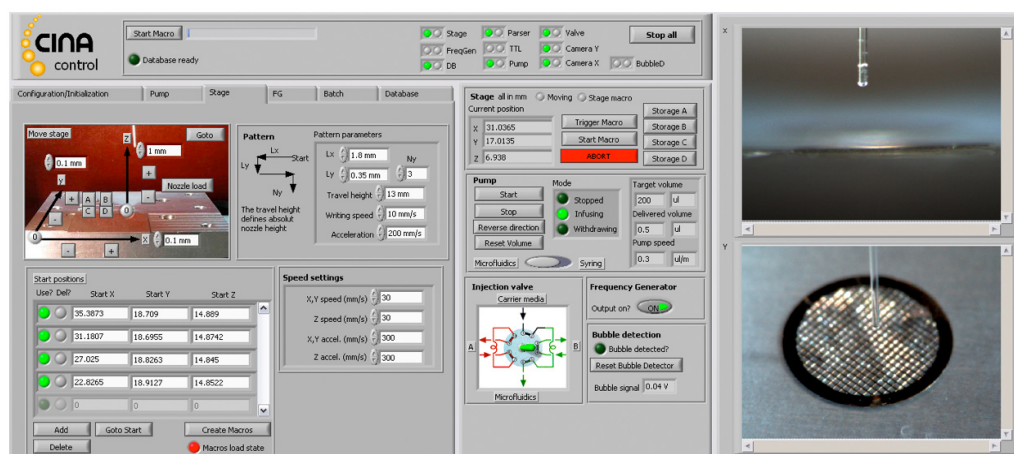
Supplementary Figure 1.   Graphical user interface of the LabView-based control software: This self-written software allows all setup components to be controlled and examined. It shows the status of all components and two cameras installed at different angles deliver live images of the nozzle and the grid being processed, respectively. The parameters controlling the components can either be set individually or via a macro language that was integrated to facilitate automation.
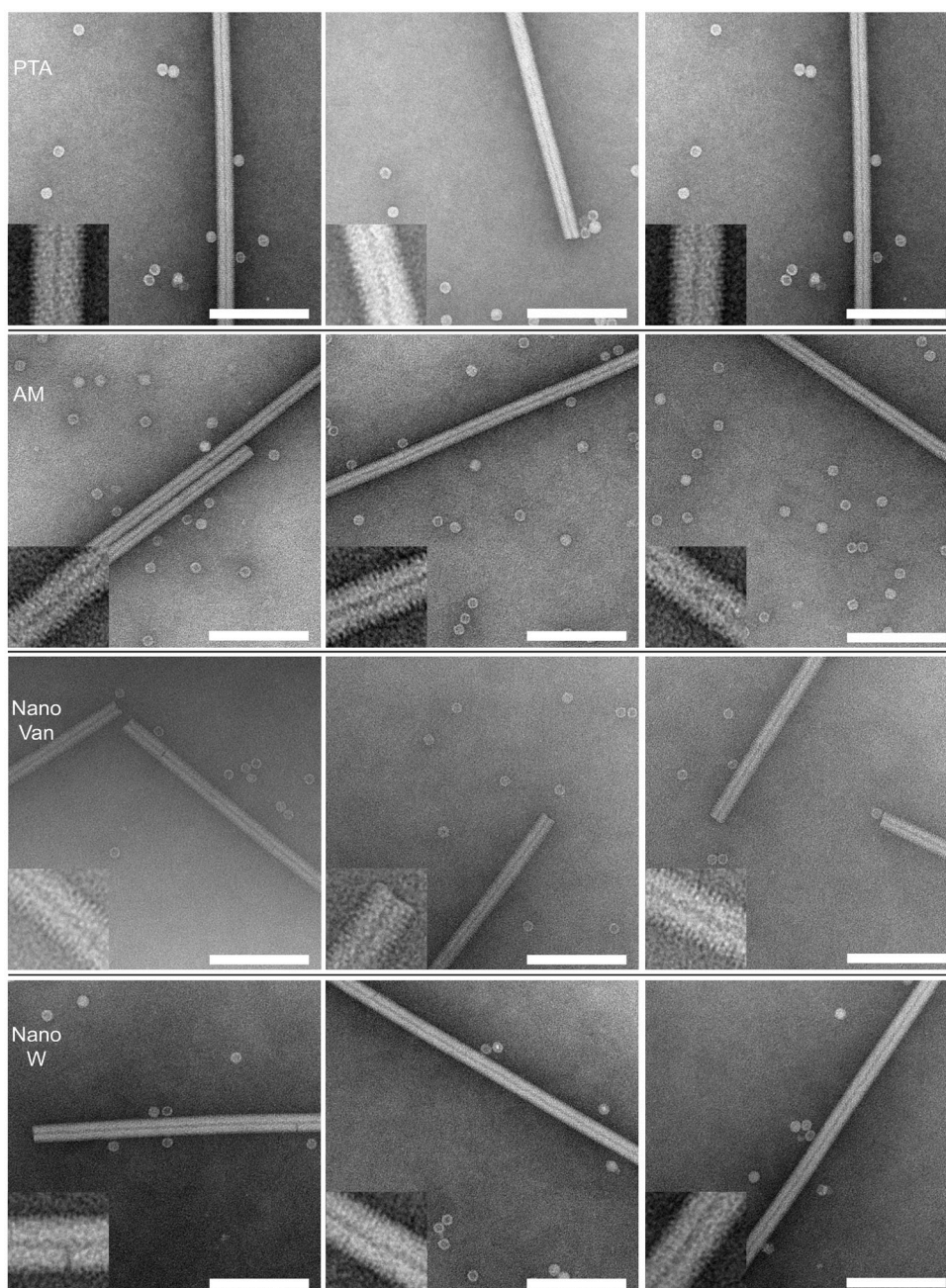
Supplementary Figure 2.   Further examples of negatively stained TMV and AF samples. For all four stains the ultrastructure of TMV and AF is well preserved and the surrounding background shows a smooth fine grain. Samples were conditioned with 1% $PTA_{7.0}$, 0.5% $AM_{6.5}$, 1% $NanoV_{8.0}$, and 1% $NanoW_{6.8}$. Scale bars: 100 nm; the insets depict three-fold enlarged regions of the TMV.
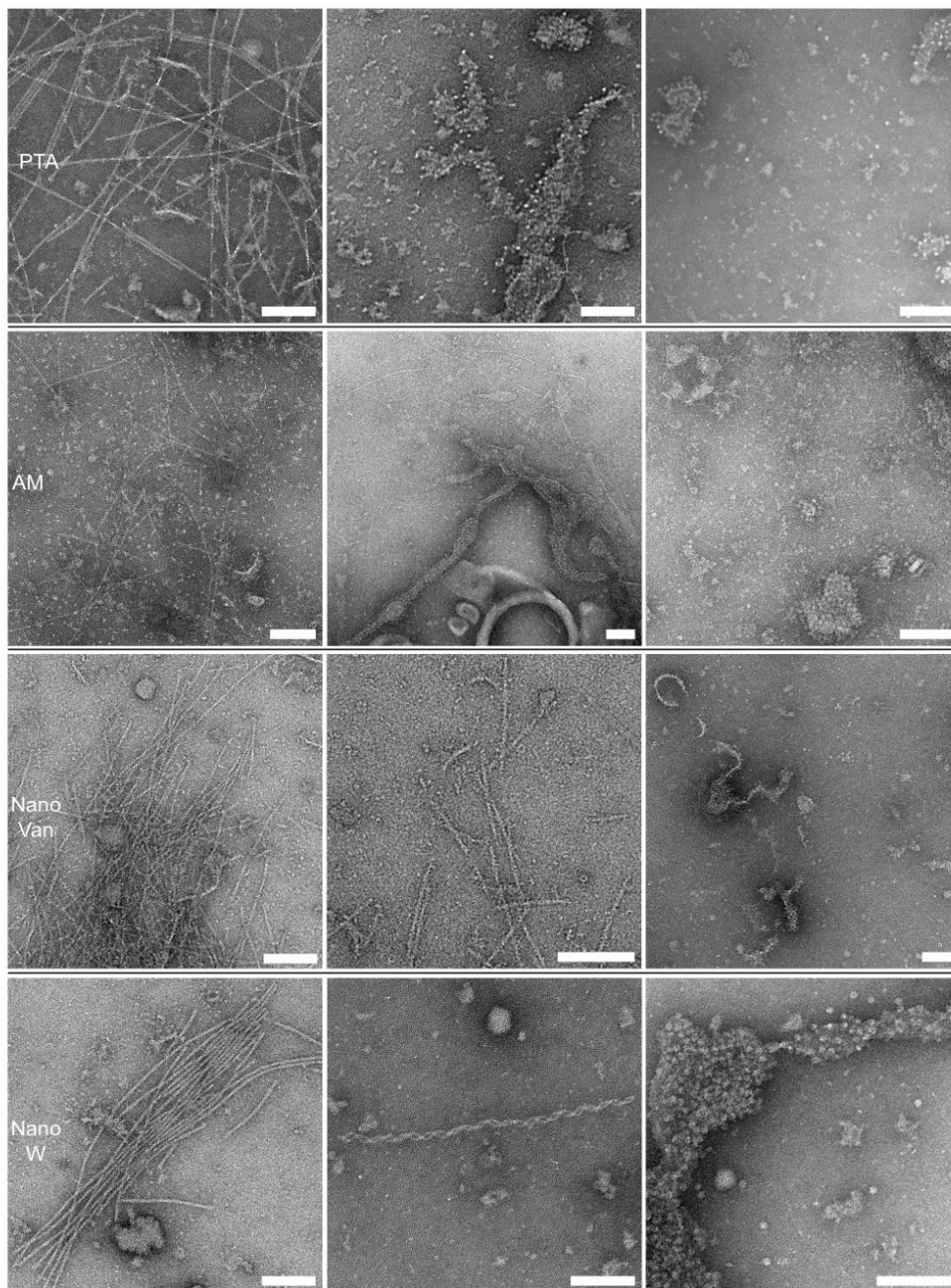
Supplementary Figure 3.   Further examples of negatively stained BHK lysate for the four different stains, revealing structures resembling actin filaments (e.g. top left) and protein-packed membranes (e.g. top center). Samples were conditioned with 2% $PTA_{7.0}$, 0.5% $AM_{6.5}$, 1% $NanoV_{8.0}$, and 2% $NanoW_{6.8}$. Scale bars: 100 nm.
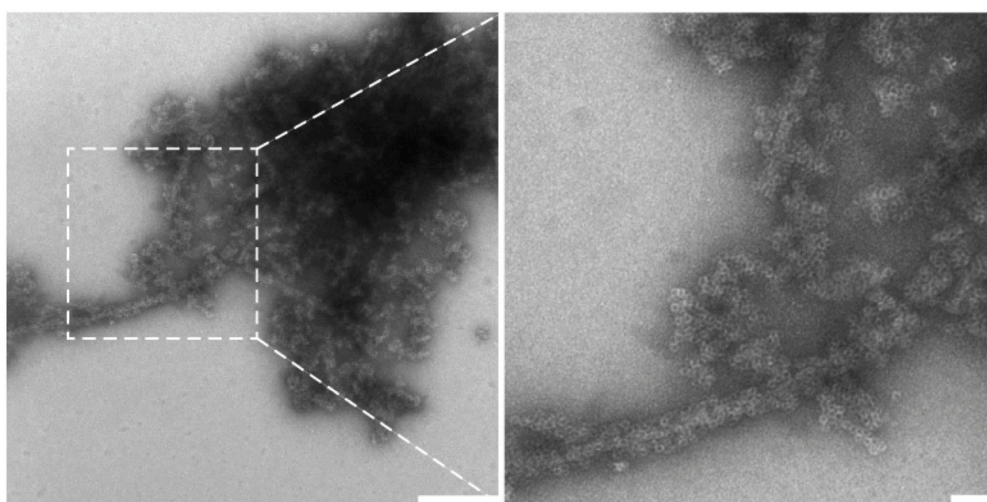
Supplementary Figure 4. UA staining results. A TEM image of aggregated TMV and AF conditioned with 0.25 % $UA_{4.5}$. An enlarged view of the marked region is shown on the right. Other experiments showed, that there is serious precipitation when $UA_{4.5}$ is mixed with the sample at concentrations above 0.5 % and dried down on the grid (data not shown), even if the buffer does not contain phosphate; the sample was in HEPES or ddH_2O. Decreasing the UA concentration to 0.25 % or below prevented the formation of precipitates, but the fixation property of UA caused sample aggregation when stain and sample were mixed prior to immobilization on the grid. Furthermore, buffering the UA solution at a concentration of 0.25 % or below at pH 7 could not prevent this sample aggregation. Scale bars: (left) 250 μm; (right) 50μm.
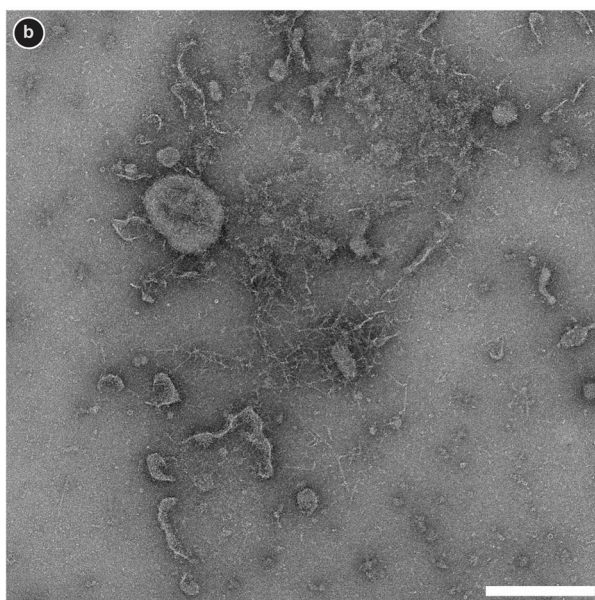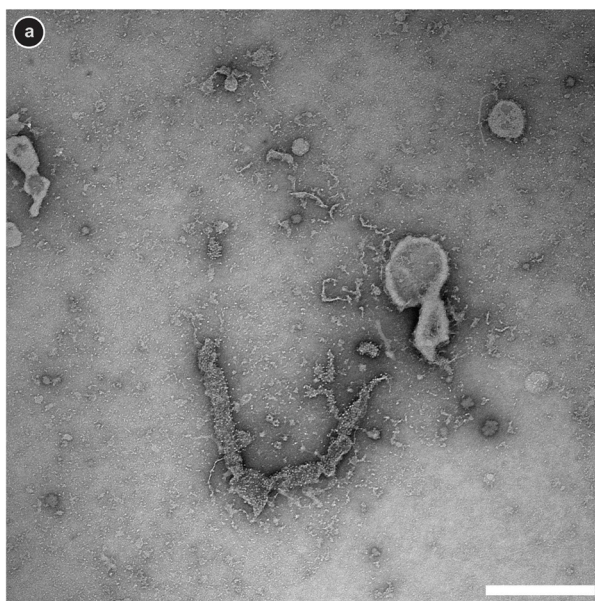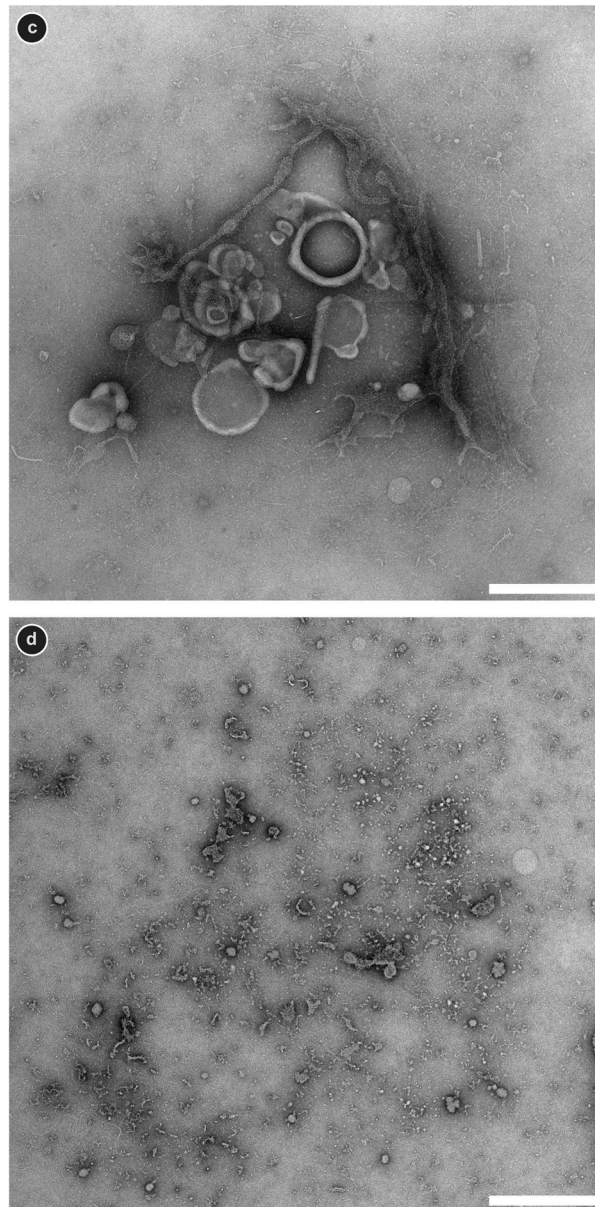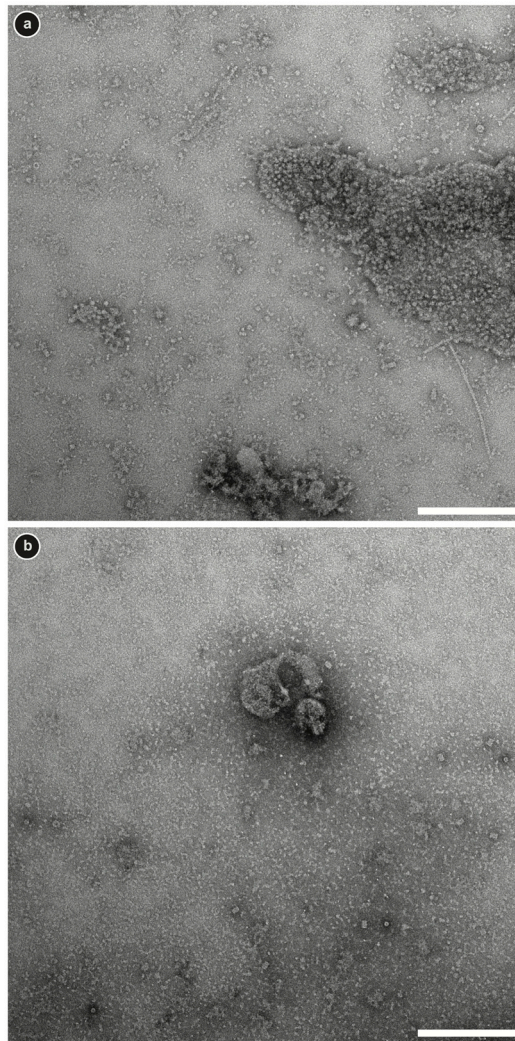
Supplementary Figure 5.   Images of BHK cell lysate demonstrating the absence of aggregation. The overview images show soluble proteins, membrane patches and filaments; there is no sign of aggregation. The sample in PBS was conditioned with (a) 2% $PTA_{7.0}$. (b) 0.5% $AM_{6.5}$. (c)1% $NanoV_{8.0}$. (d) 2% $NanoW_{6.8}$. Scale bars: 500 nm.
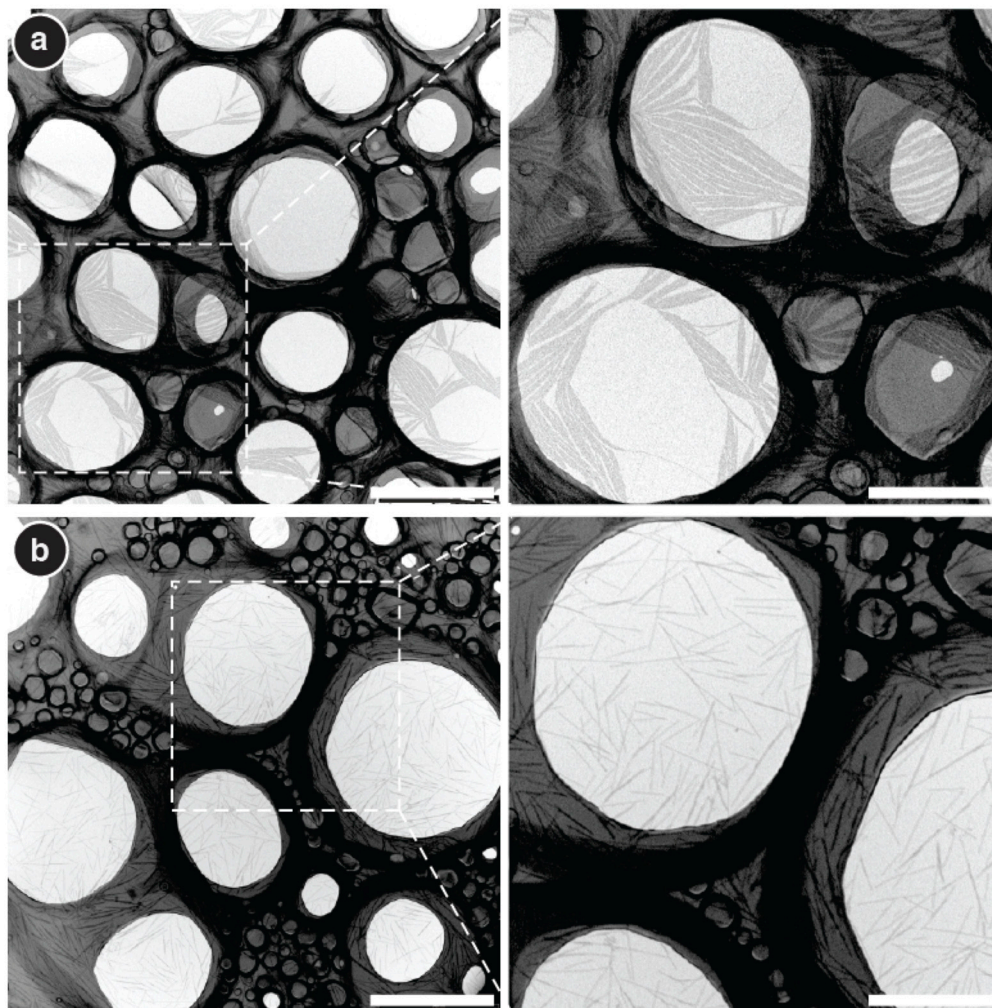
Supplementary Figure 6. TEM images of unstained TMV written on STEM grids after passage through the sample preparation module: (a) TMV in quartz-ddH$_2$0, after micro-dialysis against quartz-ddH$_2$0. The rods tend to aggregate, which would hinder mass determination; only a few are well separated from their neighbors. (b) TMV in quartz-ddH$_2$0, after micro-dialysis against 100 mM ammonium bicarbonate buffer. The rods are homogeneously distributed over the grid and generally well separated. The marked change in aggregation shows that conditioning was effective. The results illustrate that even robust samples like TMV benefit from solutions that are buffered close to physiologic pH. Scale bars: (left column) 500 µm; (right column) 250 µm.

Supplementary Figure 7. Comparison of manual and automated grid preparation. Representative overview images of lysate from heat-shocked (46 °C for 60min) BHK cells. (a) Prepared with the setup and conditioned with 1% $NanoW_{6.8}$. (b) Manually prepared (1 min sample adsorption followed by four wash steps of 5 sec) and stained with 2% $NanoW_{6.8}$ (two times 5 μl of stain for 10 sec). Besides the heat-shock proteins that can be observed with both preparation methods the setup preparation method reveals more sample constituents. Large "protein packed" membrane patches as well as filaments are abundant and clearly visible with structural details. These components were not observed when the grids were prepared by hand. Scale bars: 200 nm.

4.9 Acknowledgments

4.10 References

1   Aderem, A. *Cell* **2005**, *121*, 511-513.

2   Aloy, P. and Russell, R. B. *Nature reviews. Molecular cell biology* **2006**, *7*, 188-197.

3   Kherlopian, A. R. *BMC systems biology* **2008**, *2*, 74.

4   Ben-Harush, K.; Maimon, T.; Patla, I.; Villa, E. and Medalia, O. *Journal of cell science* **2010**, *123*, 7-12.

5   Lucic, V.; Förster, F. and Baumeister, W. *Annual review of biochemistry* **2005**, *74*, 833-865.

6   Leis, A.; Rockel, B.; Andrees, L. and Baumeister, W. *Trends Biochem Sci* **2009**, *34*, 60-70.

7   Bohm, J. *Proc Natl Acad Sci U S A* **2000**, *97*, 14245-14250 (2000).

8   Nickell, S.; Kofler, C.; Leis, A. P. and Baumeister, W. *Molecular Cell Biology* **2006**, 7, 225-230.

9   Kireev, I. *Nature Methods* **2008**, *5*, 311-313.

10 Aebersold, R. and Mann, M. *Nature* **2003**, *422*, 198-207.

11 Bremer, A., Henn, C., Engel, A., Baumeister, W. and Aebi, U. *Ultramicroscopy* **1992**, *46*, 85-111.

12 Engel, A. *Ultramicroscopy* **1978**, *3*, 273-281.

13 Müller, S. A. and Engel, A. *Micron* **2001**, *32*, 21-31.

14 Müller, S. A.; Goldie, K.; Burki, R.; Haring, R. and Engel, A. *Ultramicroscopy* **1992**, *46*, 317-334.

15 Picotti, P.; Bodenmiller, B.; Mueller, L. N.; Domon, B. and Aebersold, R. *Cell* **2009**, *138*, 795-806.

5. Extreme Ultraviolet Interference Lithography for Generation of Platinum Nanoparticles on Glassy Carbon

A. Savouchkina[a], A. Foelske-Schmitz[a], R. Kötz[a], A. Wokaun[b],G. G. Scherer[a], C. Padeste[c], J. Ziegler[c], V. Auzelyte[c], H. H. Solak[c]

[a] Laboratory for Electrochemistry, Paul Scherrer Institut, Villigen 5532, Switzerland

[b] General Energy Research Department, Paul Scherrer Institut, Villigen 5532, Switzerland

[c] Laboratory for Micro- and Nanotechnology, Paul Scherrer Institut, Villigen 5532, Switzerland

J.Z. fabricated the nanopatterning mask using extreme ultraviolet lithography and developed the multi-metal layer deposition protocol including the lift-off procedure.

5.1 Keywords

microfabrication, extreme ultraviolet interference lithography, thermal metal deposition, glancing angle metal deposition, polymer electrolyte fuel cells

5.2 Abbreviations

CB, chlorobenzene; **EBL**, electron beam lithography; **EUV-IL**, extreme ultraviolet interference lithography; **GC**, glassy carbon; **GLAD**, glancing angle deposition; **PEFC**, polymer electrolyte fuel cell; **PMMA**, poly(methyl-methacrylic acid); **SEM**, scanning electron microscopy; **SLS**, Swiss light source; **XIL**, X-ray interference lithography; **XPS**, X-ray photoelectron spectroscopy

5.3 Abstract

In order to investigate corrosion processes of a catalyst and/or its support in polymer electrolyte fuel cells (PEFC), model electrodes consisting of platinum nanodots upon glassy carbon (GC) substrate were produced via extreme ultra-violet interference lithography (EUV-IL) and subsequent platinum deposition. The exposure experiments were performed at the X-ray Interference Lithography (XIL) beamline of Swiss Light Source (SLS). The influence of exposure parameters (e.g. dose, thickness of the photoresist, amount of deposited platinum) and pre-treatment of the GC substrate upon the size of produced nanostructures and their adhesion to the surface was closely monitored using scanning electron microscopy (SEM) and X-ray photoelectron spectroscopy (XPS). The diameter of obtained Pt nanodots was in the range of 40-100 nm. It was found that the diameter of the obtained Pt nanodots was only dependent on the EUV dose. Thermal pre-treatment of GC had no obvious influence on the process steps.

5.4 Introduction

Polymer electrolyte fuel cell (PEFC) is a promising alternative for power supply in stationary and mobile applications. The catalyst which enables PEFC to function at 60-80°C and ambient pressure consists of Pt nanoparticles on a carbon support with a high surface area (e.g. Vulcan). Unfortunately, the lifetime of the PEFC is limited amongst others by degradation and corrosion of the catalyst and/or its support. There are three main reasons for the corrosion of the platinum catalyst such as (i) platinum dissolution and/or redeposition (Ostwald

Thickness [nm]	Velocity [rpm]	Acceleration [rpm/s]	Time [s]	Softbake
44	4000	2000	45	1 min @ 450°C
65	2000	1000	45	1 min @ 450°C

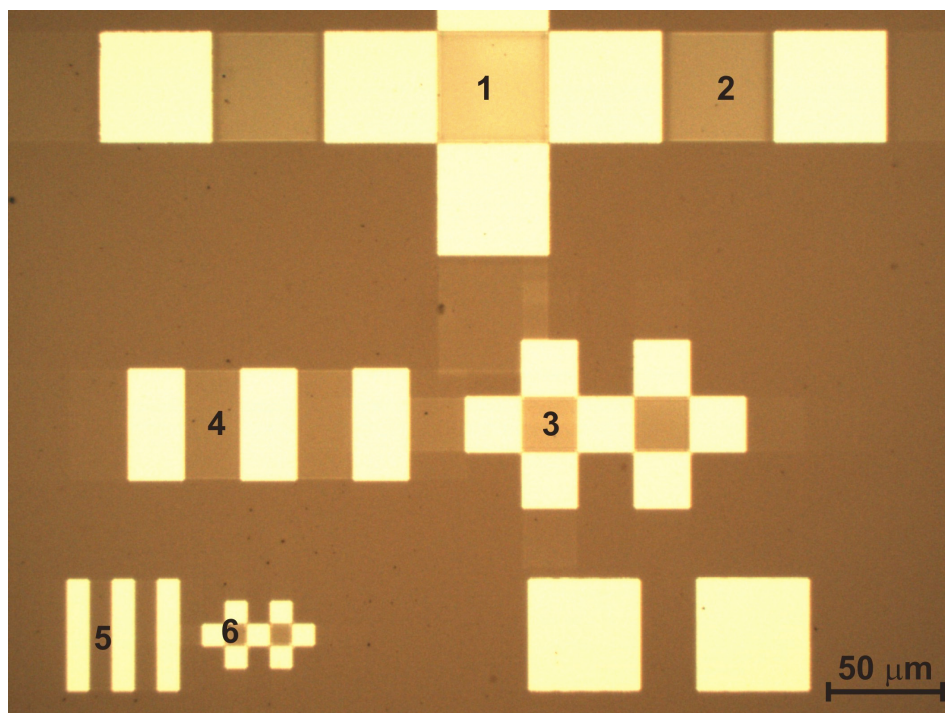**Table 1.** Spin-coating conditions for glassy carbon samples.

Figure 1. Light microscope image of a field with various structures indicated as following 1) 141 nm holes; 2) 100 nm lines; 3) 283 nm holes; 4) 200 nm lines; 5) 1500 nm lines and 6) 1500 nm holes created in one exposure.

ripening), (ii) migration and sintering of the Pt atoms on the carbon support and (iii) Pt particle agglomeration triggered by corrosion of the carbon support (1). Also the investigation of corrosion processes of the carbon support is of interest, as they may influence the degradation of the platinum catalyst.

An approach to improve the understanding of the degradation and corrosion processes of the catalyst is to prepare model electrodes consisting of Pt nanodots of various but defined sizes on a flat carbon support. Somorjai, for instance, used electron beam lithography (EBL) for the fabrication of platinum model catalysts on silicon wafers (2). However, such model electrodes are only suitable for investigation of gas phase reactions and are not designed for electrochemical experiments. The required model electrodes should be adapted to being investigated by ex-situ and in-situ methods which enable to observe changes in morphology and composition during and after electrochemical degradation of the catalyst and/or its support. Central issues of the design, which have to be addressed, are producing nanoparticles with a desired size and position. In order to achieve this narrow size distribution and defined particle arrangement, recently, Lindström et al. (3) produced model electrodes by means of colloidal lithography as well as a novel lithography technique termed Hole Mask Colloidal Lithography, introduced by Fredriksson et al. (4). These model electrodes were then used to investigate transport processes during CO oxidation on nanostructured Pt/GC electrodes. However, the size of the Pt structures created by the above-mentioned lithography methods was so far in the range of 100-120 nm (4). Typical catalyst particle size for PEFC is smaller than 10 nm.

Herein we report the approach to produce model electrodes using EUV IL. Extreme ultraviolet interference lithography (EUV-IL) is an established technique able to produce large area periodic nanostructures with structures down to 11 nm (Metals/Ge on Si wafer) (5,[6]). The X-ray interference lithography (XIL) facility at the Swiss Light Source (SLS) uses a spatially coherent beam in the extreme ultraviolet energy range. This method has been used to produce perfect epitaxial assembly of block co-polymer films (7) or patterned magnetic media for data storage (8).

Using this technique and subsequent platinum deposition via sputtering we were able to define optimized parameters for the production of Pt nanodot arrays on smooth as well as porous GC substrates down to a height of 5 nm and an average diameter of 40 nm.

5.5 Experimental

Prior to the exposure at the XIL beamline, the glassy carbon samples (Sigradur K Hochtemperatur Werkstoffe GmbH, Germany) were spin-coated with a "positive" photoresist poly(methyl-methacrylic acid) (PMMA). Before spin-coating six of the nine samples were heat-treated for 10, 20 and 30 minutes at 450°C (in air). This thermal pre-treatment opens the surface pores present in the glassy carbon substrate (9), which in turn could improve the adhesion of platinum and, therefore the lift-off process. Three samples were left untreated (as-received) to monitor this effect. Two different photoresist thicknesses, 65 and 44 nm, were chosen. The 15x15x1 mm^3 pieces of glassy carbon were first cleaned by immersion into isopropanol, ultrasonicating for 5 min and drying in nitrogen flow. The procedure was repeated for acetone and afterwards again for isopropanol. The cleaned samples were then spin-coated with an 1:6 PMMA : chlorobenzene (CB) solution under following reaction conditions (cf. Table I). Nine glassy car-

Number	Pre-treatment	Photoresist thickness [nm]
1	None	44
2	None	44
3	10 min @ 450°C (in air)	44
4	20 min @ 450°C (in air)	44
5	30 min @ 450°C (in air)	44
6	None	65
7	10 min @ 450°C (in air)	65
8	20 min @ 450°C (in air)	65
9	30 min @ 450°C (in air)	65

Table 2.   Description of glassy carbon samples to be exposed at the XIL beamline.
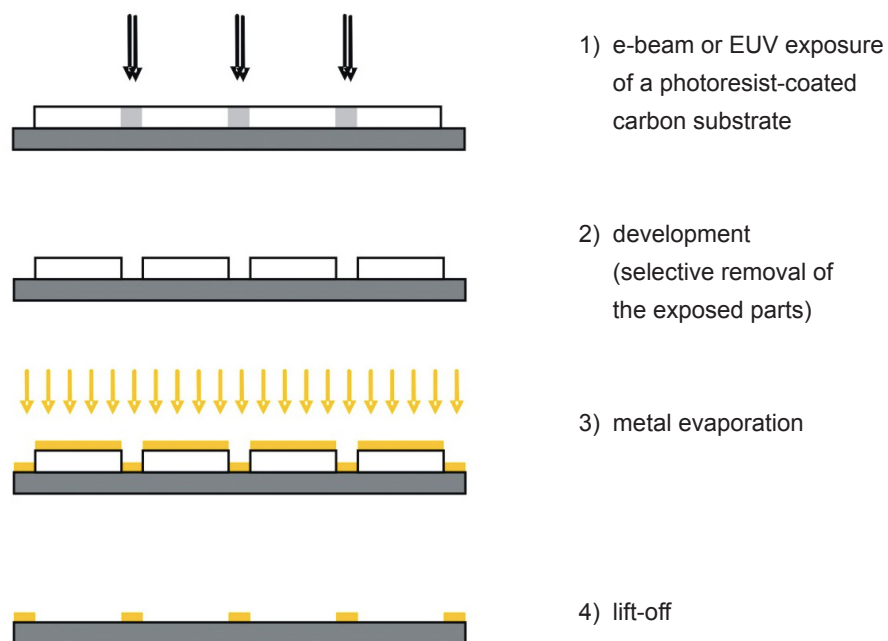
Figure 2.   Scheme of lithographic preparation of metal nanoparticle arrays on carbon substrates.

Figure 3.   Scheme of evaporation of additional Cr/Ag mask upon EUV structures using glancing angle deposition (GLAD) technique (10).
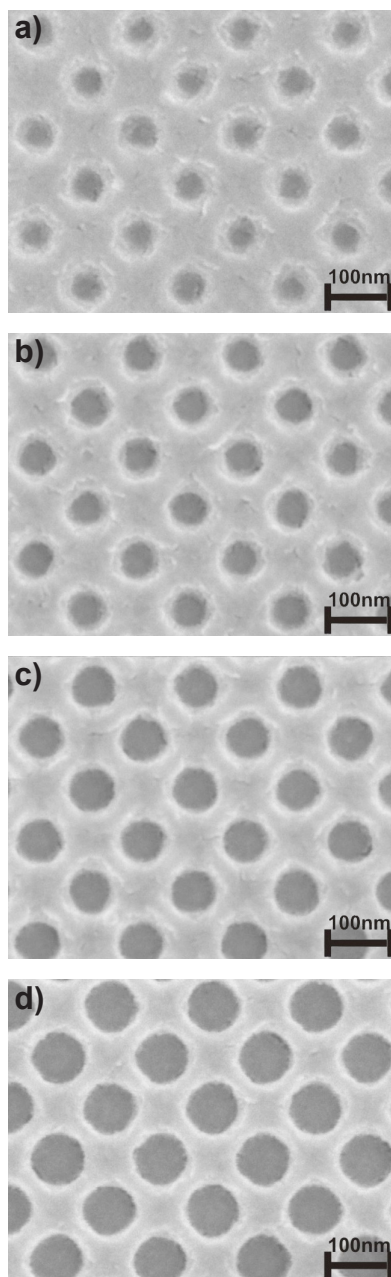
Figure 4.   SEM images of 141 nm period hole structures on GC with EUV dose of a) 62.2 mJ/cm²; b) 74.6 mJ/cm²; c) 89.6 mJ/cm²; d) 107.5 mJ/cm² before lift-off.

bon samples were chosen for the XIL exposure, four with the photoresist thickness of 65 nm and five with the thickness of 44 nm (cf. Table II).

Sample exposure was performed at the XIL beamline which uses undulator light with a central wavelength of 13.4 nm (92 eV) and 4% spectral bandwidth. The incident EUV power on the sample was several mW/cm^2 and the delivered dose was controlled in the range of 25-107.5 mJ/cm^2 using a fast beam shutter. Sample irradiation was performed according to the methods described by Solak et al. (6). Silicon nitride masks with gratings of various periods were used to create interference patterns with periodicity in the range of 141 to 1410 nm. On each sample, nine fields were exposed using EUV doses of 25-107.5 mJ/cm^2. After the EUV exposure, the samples were developed using the 3:1 mixture of methyl-isopropyl-ketone and isopropanol for 30 s at the Hamatech Steag machine. Deposition of a Pt layer was performed with a DC magnetron-sputtering device (TIPSI) with an Ar pressure of 10^{-3} mbar and a power of 30 W.

After Pt deposition the lift-off process was accomplished by soaking the GC samples overnight in acetone and ultrasonicating them for five minutes in acetone the following day. The whole exposure process is schematically depicted in Figure 2. To decrease the size of the platinum dots an additional chromium/silver mask was evaporated on the EUV exposed sample before platinum sputtering. This bi-metallic combination was chosen as chromium alone leads to a good constriction of the holes but the layers have a grainy appearance while smooth layers of pure silver clog the holes (10). For the deposition of the metal mask a Balzers BAE 250 (Oerlikon Balzers, Liechtenstein) evaporation system was used. The metal deposition was performed according to the methods described by F. A. Zoller et al. (10). For the chromium deposition the substrates were tilted to a highly oblique angle of 65°C relative to the incident flux and were continuously rotated about an axis normal to the substrate at 120 rpm/s. The deposition rate was set to 0.1 nm/s. For the silver deposition the substrates were tilted to a highly oblique angle of 70°C relative to the incident flux and were continuously rotated about an axis normal to the substrate at 120 rpm/s. The deposition rate was set to 2 nm/s. After the platinum deposition the bi-metallic mask and the photoresist were wet-etched in the **solution "Chrom etch n°1" by Microchemi**cals GmbH, containing ammoniumceriumnitrate, perchloric acid and water.
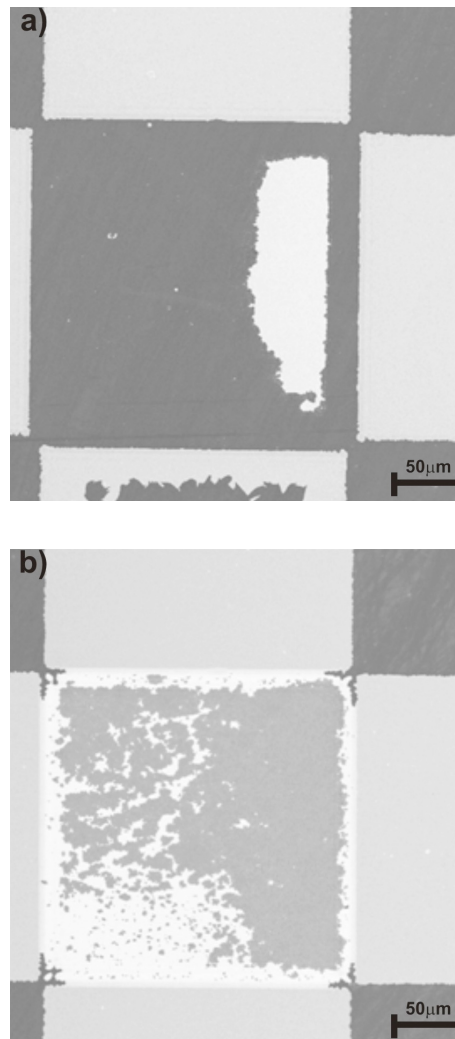
Figure 5.   An SEM image of the field with 141 nm period hole structures on GC with EUV dose of a) 43.2 mJ/cm² and b) 89.6 mJ/cm² after lift-off.

5.6 Results and Discussion

In order to find optimized conditions for the lithographic process upon each spincoated GC sample 9 fields, each with a different EUV dose, were generated. Field 1 had the lowest EUV dose of 25 mJ/cm² and field 9 the highest (107.5 mJ/cm²). On each field the pattern shown in Figure 1 was generated. The micro- and nanostructures comprised either holes (1, 3 and 6 in Figure 1) created by four-beam or lines (2, 4 and 5 in Figure 1) created by two-beam X-ray interference. In particular, the largest cross (1 in Figure 1) was investigated as it comprises 141 nm period structures which are of interest for the current work. The bright areas in Figure 4 correspond to areas of direct exposure, the darker ones are those with photoresist and/or interference patterns.

The platinum deposition was performed by sputtering platinum on the developed GC samples prior to the lift-off procedure. The samples were investigated prior to and after lift-off to test whether the procedure was successful. The diameter of obtained nanostructures before lift-off varied from 50 to 100 nm, depending on the dose (Figure 4). The bright area indicates the photoresist covered by platinum and the dark round structures are holes with platinum on the bottom. As expected, the size of the holes increases with increasing EUV dose, as the employed positive photoresist is more susceptible to higher energy densities.

After the lift-off, the samples were investigated once again with SEM. The completeness of the lift-off procedure was dependent on the EUV dose of the investigated field. The 141 nm structures on the fields with lower EUV doses (d < 62.2 mJ/cm²), were completely removed by the process (Figure 5 a)), while for the fields with higher EUV dose the procedure was successful. The best result has been achieved for the dose of 89.6 mJ/cm² (cf. Figure 5 b)): Dark parts of the image represent the photoresist-free GC where only carbon support is left, the bright, almost white area is the photoresist covered with Pt and the gray area displays a successful lift-off with platinum nanodots. The gray area covers ca 80 % of the exposed field proving that most of the structures withstood the lift-off process under the chosen preparation conditions. **The dose with the most nano-dots after the lift-off was determined to be dose 8 or 89.6 mJ/cm²** (cf. Figure 5

b)) for both employed photoresist thicknesses and different pre-treatment conditions of the GC substrate.

Seven out of nine samples have been measured with SEM after lift-off to find the best conditions for the exposure; the results are summarized in Table III. Pt nanodots could be found for doses above 43.2 mJ/cm², i.e. 51.8 mJ/cm² to 107.5 mJ/cm². A thinner photoresist led to better results due to easier the lift-off procedure, there are nanodots also on the fields with lower EUV doses (compared to a thicker photoresist) and the abundance of the dots is higher (cf. Table III). There is no obvious influence of the thermal pre-treatment on the platinum adhesion (compare the rows with different length of thermal pre-treatment). The success of the lift-off step is increasing with higher EUV dose, however, the field with the highest EUV dose (107.5 mJ/cm²) presented a challenge, here the photoresist remained even after the lift-off process.

The SEM images have shown that the size of the nano-particles increases almost linearly with the applied EUV dose (cf. Figure 6), reaching from approximately 40 to 100 nm. Little difference in size was observed for two different photoresist thicknesses. After lift- off the smallest structures have the size of 40 nm and the largest of 100 +/-5 nm (cf. Figure 6). The only change is in the quality of the lift-off process, if a thinner photoresist was used, it was possible to find Pt nanoparticles on five doses instead of four (cf. Table III).

The smallest nanodots were obtained for the fields with lower EUV dose (cf. Figure 6). However, only little area upon these fields withstands the lift-off process and displays the desired arrangement of the nanodots (cf. Table III). Thus, a possibility to further decrease the diameter of nanodots without lowering the EUV dose was tested. For this purpose, an additional Cr/Ag mask was evaporated on the EUV exposed sample using a glancing- angle-deposition (GLAD) process.

Afterwards, the sample was investigated via SEM to measure the reduced diameter of the holes and to make sure that the vapour-deposition process was successful (Figure 8 a). This figure displays the nanoholes (black and round, highlighted by white circles around them, with a diameter of approximately 44 nm), some silver-uncoated chromium (grayish) and chromium/silver mask
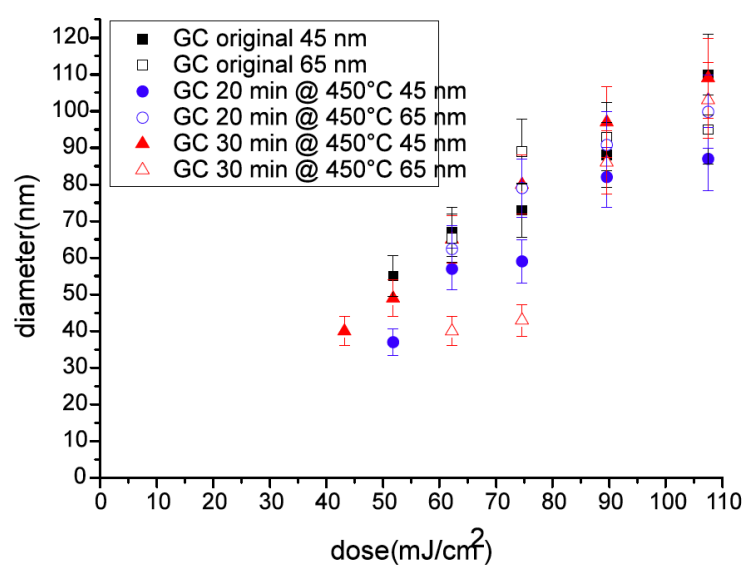
Figure 6.   Diameter vs. dose (measured via SEM) diagrams of the seven investigated samples after lift-off. Photoresist thickness is 44 nm (solid symbols) and 65 nm (open symbols).
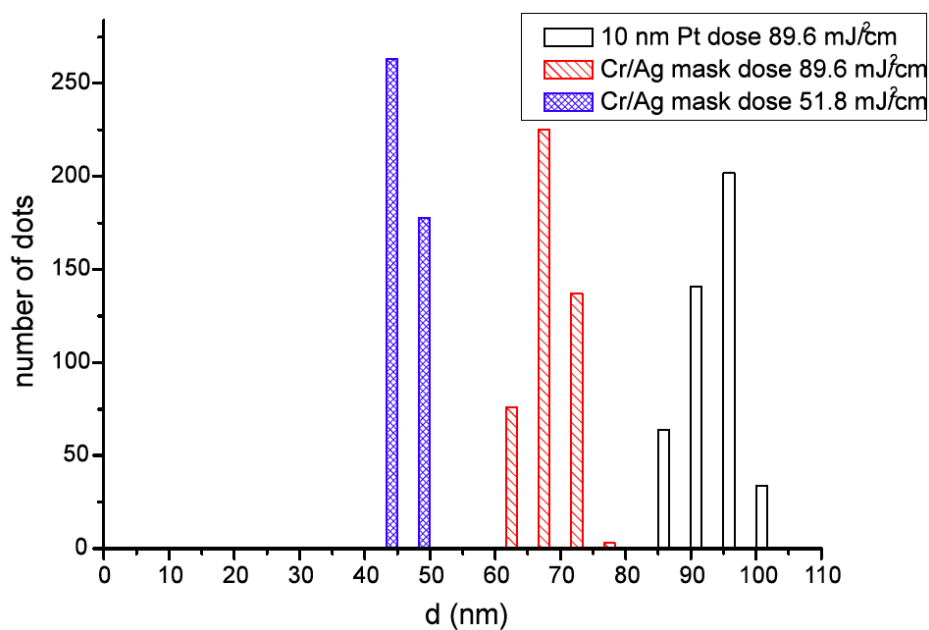
Figure 7.   Size distribution on the model electrodes. Empty bars represent a GC model electrode with PMMA thickness of 65 nm, 10 nm Pt layer and the dose of 89.6 mJ/cm²; dashed a GC model electrode with PMMA thickness of 44 nm, additional Cr/Ag mask,   5 nm Pt layer and the dose of 89.6 mJ/cm² and chequered a GC model electrode with PMMA thickness of 44 nm, additional Cr/Ag mask, 5 nm Pt layer and the dose of 51.8 mJ/cm².

Sample: GC	Time [min] @450°C	Dose [mJ/cm²]								
		25	30	36	43.2	51.8	62.2	74.6	89.6	107.5
Photo resist thickness 65 nm	0	<1	<1	<1	<1	<1	1-19	20-60	20-60	1-19
	10	<1	<1	<1	<1	<1	<1	1-19	61-100	61-100
	20	<1	<1	<1	<1	<1	<1	1-19	1-19	61-100
	30	<1	<1	<1	<1	<1	<1	<1	1-19	1-19
Photo resist thickness44 nm	0	<1	<1	<1	1-19	1-19	20-60	20-60	61-100	<1
	20	<1	<1	<1	<1	61-100	61-100	61-100	61-100	20-60
	30	<1	<1	<1	<1	20-60	61-100	61-100	61-100	20-60

Table 3. Summarized results of the lift-off process, the numbers (percentage) indicates the part of whole area which is covered with Pt nanodots

(bright, largely oval-shaped islands).

The results of SEM measurements were very satisfactory, upon the dose of 89.6 mJ/cm2, for instance, the size of the nanoholes could be decreased by almost 50 % (from approx. 100 nm to approx. 60 nm). The smallest holes which could be produced were in the range of 40-45 nm (cf. Figure 8 a). The next step was to deposit platinum and test whether this metal would survive the etching conditions and whether the obtained platinum nanodots would be free from chromium and silver residues.

After deposition of a 5 nm thin Pt layer via sputtering, the chromium/silver mask was removed by treating the sample with a chromium etch solution, which removed not only chromium and silver but also the excess photoresist. The size of the resulting nanodots ranged from 40 nm (dose of 51.8 mJ/cm2, Figure 8 b) to 80 nm (dose of 107.5 mJ/cm2). The etching process was very thorough, neither chromium nor silver were found on the sample surface. The only contamination which could be measured with XPS was traces of cerium (0.5 at %) originating from the etching solution.

The obtained model electrodes displayed not only a defined geometrical arrangement but also a narrow diameter distribution of platinum dots (Figure 7). The diameter of the dots for the dose of 89.6 mJ/cm², the one where the lift-off step worked best for all samples, was 65 nm (dashed bars in Figure 7) with and 85 nm (empty bars in Figure 7) without an additional Cr/Ag mask. Also the
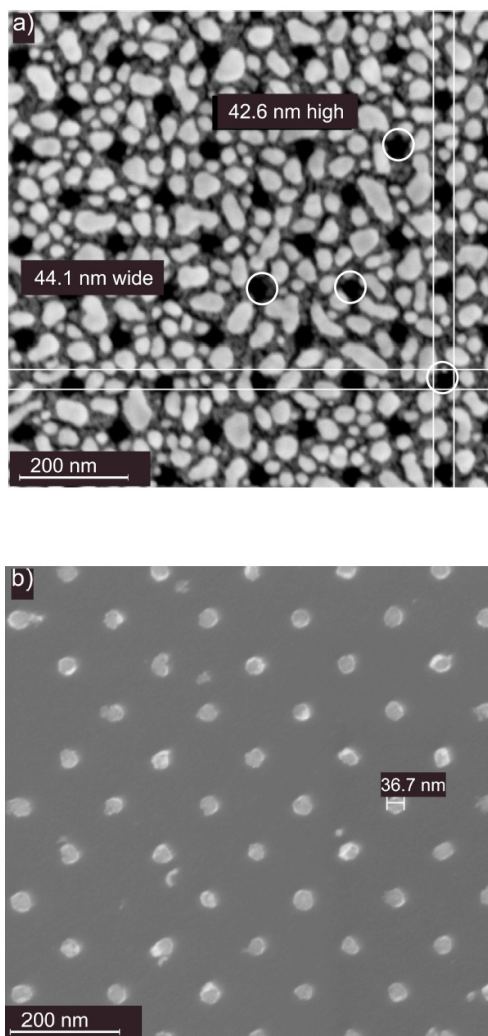
Figure 8.　SEM images of a) glassy carbon surface with a 30 nm Cr and 20 nm Ag layer (dose of 51.8 mJ/cm²) and b) platinum nanodots after removal of chromium, silver and photoresist via etching.

dose of 51.8mJ/cm^2 with 45 nm small dots (chequered bars in Figure 7) showed a uniform size distribution.

5.7 Conclusion

EUV IL was used to produce Pt/GC model electrodes with Pt nanodots. The diameter of the obtained dots ranged from 60 (51.8 mJ/cm^2) to 100 nm (107.5 mJ/cm^2), increasing with larger EUV doses. Smaller nanodots with diameter of 40 nm could be produced using an additional chromium/silver mask. The lift-off worked best for thin photoresist (44 nm) and the EUV dose of 89.6 mJ/cm^2, the diameter of the obtained nanodots for this dose was around 80 nm. The thermal pre-treatment of glassy carbon had no obvious influence on the completeness of lift-off process or on the diameter of Pt nanoparticles. EUV proved a good technique to control the size distribution as well as the arrangement of the nanodots on the surface.

5.8 Acknowledgment

5.9 References

1   Fereira, P. J.; La O, G. J.; Shao Horn, Y.; Morgan, D.; Makharia, R.; Kocha, S. and Gasteiger, H.A. *J. Electrochem. Soc.* **2005**, *152/11*, A2256-A2271.

2   Somorjai, G. A. *Appl. Surf. Sci.* **1997**, *1*, 121-122.

3   Lindström, R. W.; Seidel, Y. E.; Jusys, Z.; Gustavsson, M.; Wickman, B.; Kasemo B. and Behm, R. J. *J. Electroanal. Chem. In Press.*

4   Fredriksson, H.; Alaverdyan, Y.; Dmitiev, A.; Langhammer, C.; Sutherland, D. S.; Zäch, M. and Kasemo, B. *Adv. Mater.* **2007**, *19*, 4297.

5   Auzelyte, V.; Dais, C.; Farquet, P.; Grützmacher, D.; Heyderman, L. J.; Luo, F.; Olliges, S.; Padeste, C.; Sahoo, P.; Thomson, T.; Turchanin, A.; David C. and Solak, H. H. *J. Micro/Nanolith. MEMS MOEMS* **2009**, *8*, 21204.

6   Solak, H. H.; David, C.; Gobrecht, J.; Golovkina, V.; Cerrina, F.; Kim, S. O. and Nealey, P. F. *Microelectron. Eng.* **2003**, *67*, 56-62.

7   Kim, S. O.; Solak, H. H.; Stoykovich, M. P.; Ferrier, N. J.; De Pablo, J. J.; and Nealey, P. F. *Nature* **2003**, *424*, 411-414.

8   Heyderman, L. J.; Solak, H. H.; David, C.; Atkinson, D.; Cowburn, R. P. and Nolting, F. *Appl. Phys. Lett.* **2004**, *85*, 4989.

9   Braun, A.; Bärtsch, M.; Schneider, B.; Kötz, R.; Haas, O.; Haubold, H. G. and Goerigk, G. *J. Non-Cryst. Solids* **1999**, *260*, 1-14.

10   Zoller, F. A.; Padeste, C.; Ekinci, Y.; Solak H. H. and Engel, A. *Microelectronic Eng.* **2008**, *85*, 1370-1374.

6. Fabrication of Large Scale Arrays of Metallic Nanodots by means of High Resolution E-beam Lithography

Vitaliy A. Guzenko[a], Jörg Ziegler[a], Anastasia Savouchkina[a], Celestino Padeste[a], and Christian David[a]

[a] Paul Scherrer Institut, 5232 Villigen PSI, Switzerland

6.1 Keywords

single shot EBL, large scale nanodot arrays, thermal metal deposition, annealing, double layer photoresist

6.2 Abbreviations

DAC, digital-to-analog converter; **EUV-IL**, extreme ultraviolet interference lithography; **HSQ**, hydrogen silsesquioxane; **IPA**, isopropyl alcohol; **MIBK**, methyl isobutyl ketone; **PMMA**, poly(methyl-methacrylic acid); **SEM**, scanning electron microscopy

6.3 Abstract

We present the fabrication of large nanodot arrays with very small single dot sizes made of different metals and on different substrates using e-beam lithography and lift-off techniques. Nanodot arrays have a high potential for bioanalytical applications aiming towards single molecule detection. In addition, they can be used as well defined models of heterogeneous catalysts. For this purpose an independent control of the dot size and the distance between the dots is necessary. This is a limitation for many fabrication techniques, which can be overcome by e-beam lithography. However, aiming for the dot size of few tens of nanometers, we observed a strong influence of the beam focusing and astigmatism on the quality of the fabricated nanodot arrays. A significant improvement, i.e. reduction of defect density as well as better control of the dot size, was achieved by modification of the fine focus and stigmation system of the used e-beam writer. Using lift-off technique, we successfully fabricated platinum dot arrays on glassy carbon with target dot diameter ranging from 25 to 35 nm. By applying additional annealing step, we could fabricate nanodot arrays made of gold on SiO2 with very small dot sizes down to 6 nm and pitch of 100 nm. Furthermore, the generation of large area arrays of nanosized pillars was demonstrated using the same exposure strategy in a negative tone HSQ resist.

6.4 Introduction

In the recent years, the number of publications and research projects working with large scale nanostructured surfaces is continuously growing. For example, the integration density of protein arrays for bio-analytical applications is steadily being increased and is approaching the level of high-density nanoarrays [1]. The ultimate integration of nanoarrays is reached with protein immobilization sites in the size of single protein molecules which may for instance be made from gold islands to which proteins are immobilized via thiol linker chemistry [2,3]. Such arrays could furthermore greatly enhance the sensitivity of bioanalytical sensors.

Arrays of nanoparticles made of platinum have also found their application for the studies of fundamental processes of heterogeneous catalysts [4,5] or of the corrosion processes of electrodes. Here, a model system made of catalyst nanoparticles on the glassy carbon substrates can help to get deeper insight into their electromigration and clustering behavior in dependence on the distance between the particles [6].

Large areas of regular nanodot arrays have been produced by means of EUV interference lithography for applications in bioanalytical systems [2] or as model electrodes in polymer electrolyte fuel cells [7]. This method results in very low defect density dot arrays with feature sizes approaching the 10 nm mark [8]. However, both applications need an independent control of the dot size and the distance between them, which is difficult to achieve by EUV interference lithography. In order to solve this problem an electron beam lithography tool Vistec EBPG5000Plus has been used. This direct writing tool is operated at 100 keV and is capable of exposing any required arrangement of two-dimensional shapes by scanning a Gaussian beam spot of few nm in diameter over the sample surface. Even though the throughput of e beam lithography is relatively low, fabrication of large scale rectangular nanodot arrays could be achieved within reasonable exposure times, due to the high deflection capabilities of the e-beam writer and the chosen "single shot" exposure strategy.

6.5 Experimental Procedure

In order to prepare the metallic nanodot arrays, glassy carbon (Type A) or thermally oxidized silicon (Type B) samples were coated by double-layer of poly(methyl methacrylate) (PMMA) positive tone resist. First, a layer of resist with the lower molecular weight of the polymer chains (PMMA 50k) and than the one with the heavier chains (PMMA 950k) was spin-coated. Bake-out step at 175°C on a hot plate for at least 5 min followed every coating step. The rotation speed of the spin-coater was chosen as high as required in order to obtain the resulting thicknesses of 30 nm for each resist layer. E-beam lithography of such resist coating results in a slight undercut profile, which is preferable for lift-off processes.

For exposures of the dot arrays in a negative tone resist, silicon wafers have been dehydrated at 180°C prior to spin-coating by hydrogen silsesquioxane (HSQ) and then transferred directly into vacuum to avoid the aging of the resist.

Exposures of the dot arrays were performed using Vistec EBPG5000Plus electron beam lithography tool, operated at 100 keV. This e-beam writer is equipped with a pattern generator which can be operated at beam stepping frequencies up to 50 MHz, and a deflection system, capable of deflecting the beam to large angles so that a writing field as large as 512×512 μm2 can be exposed without any stage movements. The Gaussian shaped beam was focused to approximately 10 nm in diameter at a beam current of 10 nA. Rectangular dot arrays were generated by exposing 10×10 mm2 large squares with the beam step size set equal to the required dot pitch (100 nm or 200 nm in our experiments), so that the exposure of each dot was performed within a single "beam shot". This well established technique allows very high exposure speeds for large scale dot arrays. Exposed PMMA samples were spray developed in a MIBK:IPA (1:3) solution for 45 sec, rinsed in IPA for 30 sec and dried by centrifugation at 3000 rpm. The development of the exposed HSQ samples was performed using MICROPOSIT 351:DI water (3:1) solution for 2.5 min, followed by sequential rinsing in DI water and IPA. These samples were dried using a nitrogen blow gun.

Type A samples were metalized by Pt (5 nm) with DC magnetron sputtering

tool at Ar pressure of 10^{-3} mbar and a power of 30 W. In case of Type B samples, Cr (1 nm)/Au (2 nm) film was deposited using the resistive evaporation at the deposition rate of 1 nm/min. Finally, a "lift-off" removal of resist and excessive metal was done in acetone using an ultrasonic bath.

6.6 Results and Discussion

The optimum exposure doses were determined from a dose series of dot arrays with reduced areas. The optimum exposure doses for fabrication of the dot arrays in PMMA with the period of 100 nm and 200 nm were determined to be 44 µC/cm2 and 13 µC/cm2, respectively. Using these doses we performed the exposure of large scale areas, however, instead of homogenous dot arrays, a mosaic-like pattern was observed, that was repeated in every writing field, as depicted in Figure 1(a). In case of metallic dots, square regions of about 4×4 µm2 with well defined dot arrays could be found besides regions with many or even all missing dots, as shown in Figure 1(b). Closer SEM inspection of the samples before lift-off showed square regions, which were underexposed and consequently not completely developed. Thus, the reduced exposure dose was a reason for the missing dots.

Exposures of the dot arrays in 150 nm thick HSQ with the period of 160 nm and the dose of 300 µC/cm2 did confirm our conclusion, that some square regions are underexposed. Here, underexposed dots were not missing, but had a smaller diameter. If, due to underexposure, the resulting diameter of a dot (actually, of a rod) went below a critical value, its mechanical stability was disturbed. Therefore, drying of the sample after the development step resulted in many bended rods, which can be clearly seen in the Figure 1(c).

Reproducibility of the mosaic-like pattern and the size of the easily distinguishable regions with clearly different lithography quality allowed us to conclude that the origin of the problem was hidden in the e beam tool itself. There was obvious dependence of the local quality of the dot array on the deflection angle of the beam. Therefore, we took a closer look at the fine focus and stigma-
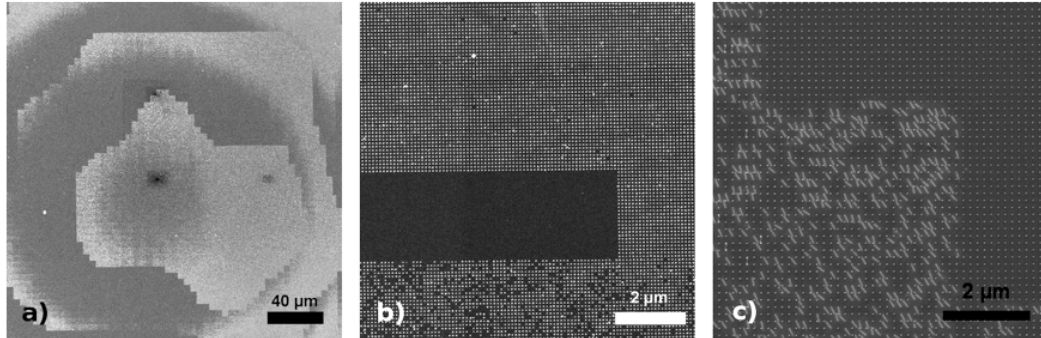
106

Figure 1. SEM images of large scale nanodot arrays exposed before modification of the fine focusing and stigmation correction unit: (a) A Pt dot array after lift-off and (b) a zoom in into the area with different defect density; (c) Fragment of a nanorod array exposed in HSQ showing the mechanical instability of individual rods in some trapezium fields.

tion system of the e-beam tool. Its task is to compensate for the defocusing and astigmatism of the deflected beam, which are most pronounced at large deflection angles. Indeed, the color-coded representation of DAC settings of the fine focus compensation system in dependence on the deflection angle, shown in Figure 2(a), resembled very well the shape of the mosaic-like pattern found on the specimens.

Thus, the fine focus and stigmation system did not compensate sufficiently well for the defocusing and astigmatism effects. The beam spot diameter varied across the writing field and, in turn, the effective dose at locations with larger deflection angles dropped below "dose-to-clear". Further increase of the deflection angle caused an increment of the DAC value of the fine focus and remarkable change of the beam spot size. As a result, a gradual changing with several jumps of effective exposure dose across the large scale dot arrays was observed.
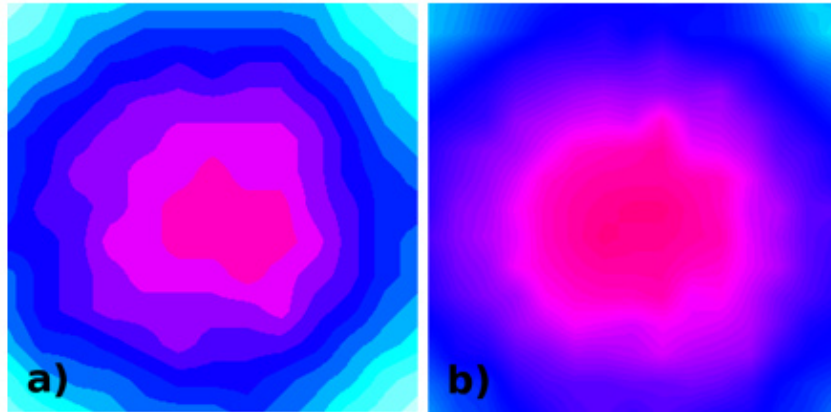
Figure 2.   A graphical representation of the focus correction table: (a) before and (b) after the hardware modification. Each color, starting from center, represents a unit increment of DAC value across the 500×500 µm² writing field.

In many cases, such variations of the beam spot size do not have a remarkable effect on the exposure result, since the beam step size is smaller than the spot diameter and the neighboring shots are overlapping. However, for exposures of nanodot arrays even small deviations of the spot size from the optimum have significant impact on the dot size. Hence, a fine-tuning of the fine focus and stigmation system was inevitable. For this purpose, a special modification of the hardware of the e-beam writer was implemented in cooperation with Vistec Lithography B.V. This allowed us to control more accurately the beam quality over the whole write field (see Figure 2(b), which resulted in a uniform size distribution of the exposed dots.

Several examples of the dot arrays after the hardware modification are shown in the Figure 3. A number of high quality 1×1 cm2 large arrays were produced by lift-off of 5 nm thick sputtered Pt with the dot size down to 25 nm. In case of thermally evaporated Cr/Au nanodots, an additional annealing in a quartz tube furnace at 600° C for 10 minutes in the dry nitrogen atmosphere followed by

cooling down of 10 min in N2 allowed us to reduce the dot size from in average 13 nm down to 6 nm, which was confirmed by comparison of fabricated dots with the 10 nm big colloidal gold particles, which were randomly distributed over the sample surface. A test exposure in 150 nm thick HSQ resulted in a uniform, mechanically stable array of SiO2-like nanorods with diameter of 21 nm, and thus, confirmed the success of modification of the e-beam lithography tool and its importance for fabrication of the large scale nanodot arrays.
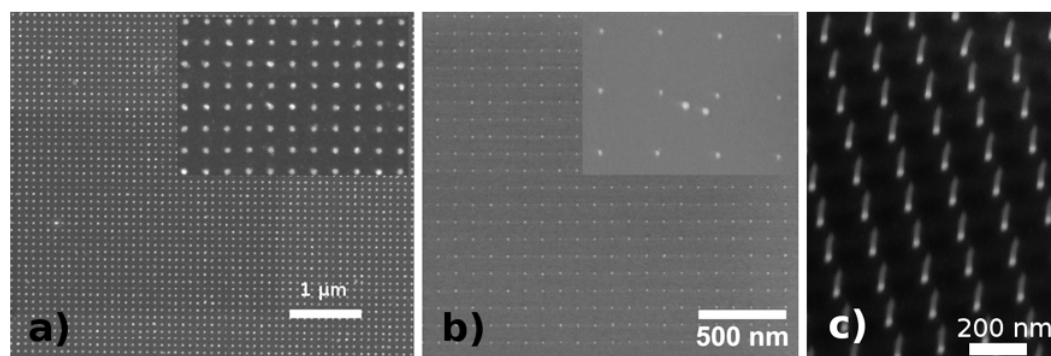

Figure 3. SEM images of several large scale arrays fabricated after focusing and stigmation hardware modification: (a) 5 nm high Pt nanodots on glassy carbon with 100 nm pitch and average dot diameter of 25 nm. (b) Cr(1 nm)/Au(2 nm) nanodots on thermally oxidized silicon with 100 nm pitch and average dot diameter of 6 nm annealed at 600° C. The inset shows 10 nm colloidal gold particles distributed over the sample surface, to compare with the fabricated nanodots. (c) Nanorod array exposed in 150 nm thick HSQ on Si with the dot diameter of 21 nm (sample was tilted by 32°)

6.7 Conclusions

From analysis of the imperfections of the large scale nanodot arrays fabricated by e-beam lithography using "single shot" technique, we concluded that the current density distribution in the Gaussian shaped electron beam is of utmost importance for the quality of obtained structures. By modifying the existing e-beam lithography tool, a significant improvement of the beam quality control, i.e. of the fine focusing and astigmatism correction, was achieved across the writing field of 500×500 μm2. This allowed us to fabricate large scale arrays of metallic nanodots and of HSQ nanorods with independent control of the dot size and period while keeping the exposure time at a reasonable level. Uniform arrays of nanodots were made of platinum on glassy carbon with dot size in the range from 25 to 35 nm. Gold dots on oxidized silicon with dot diameters as small as 6 nm were successfully fabricated using lift-off technique and subsequent annealing step.

6.8 Acknowledgment

6.9 References

1   Wingren, C. and Borrebaeck, C.A.K. *Drug Discovery Today* **2007**, *12*, 813-819.

2   Zoller, F.A.; Padeste, C.; Ekinci, Y.; Solak, H.H. and Engel, A. *Microelectronic Engineering* **2008**, *85*, 1370-1374.

3   Lee, S.W.; Shin, Y.-B.; Jeon, K.S.; Jin, S.M.; Suh, Y.D.; Kim, S.; Lee, J.J. and Kim, M.-G. *Ultramicroscopy* **2008**, *108*, 1302-1306.

4   Somorjai, G. A. *Applied Surface Science* **1997**, *121*, 1-19.

5   Jacobs, P. W.; Wind, S. J.; Ribeiro, F. H. and Somorjai, G. A. *Surface Science* **1997**, *372*, L249-273.

6   Lindström, R.W.; Seidel, Y.E.; Jusys, Z.; Gustavson, M.; Wickman, B.; Kasemo, B. and Behm, R.J. *Journal of Electroanalytical Chemistry* **2010**, *644*, 90-102.

7   Solak, H.H. and Ekinci, Y. *Journal of Vacuum Science & Technology* **2007**, *25 (B)*, 2123-2126.

8   Savouchkina, A.; Foelske-Schmitz, A.; Kötz, R.; Wokaun, A.; Scherer, G. G.; Padeste, C.; Ziegler, J.; Auzelyte, V. and Solak, H. H. *ECS Transactions*, **2010**, *25*, 175.

7. Label-free Single Molecule Detection using Multi-Arrays of Individual Immobilized DARPins

Jörg Ziegler[a,b], Manuel Simon[c], Vitaliy Guzenko[a], Andreas Plückthun[c], Andreas Engel[d], Celestino Padeste[a]

[a] Laboratory for Micro- and Nanotechnology, Paul Scherrer Institut, Villigen 5532, Switzerland

[b] Center for Cellular Imaging and Nanoanalytics (C-CINA), Biozentrum, Universität Basel, Basel, Switzerland

[c] Biochemisches Institut, Universität Zürich, Winterthurerstrasse 190, Zürich 8057, Switzerland

[d] Department of Pharmacology, Case Western Reserve University, Cleveland, USA

7.1 Keywords

EBL, acetone lift-off, DARPins, direct immobilization, single molecule detection, label-free, AFM

7.2 Abbreviations

AFM, atomic force microscope; **DARPins**, designed ankyrin repeat proteins; **DCM**, dichloromethane; **DMF**, dimethylformamide; **DMSO**, dimethylsulfoxide; **ELISA**, enzyme-linked immunosorbent assay; **MBP**, maltose binding protein **PBS**, phosphate-buffered saline; **PEG**, polyethylene glycol

7.3 Introduction

The immobilization of recognition molecules on a surface controlling their density towards single molecule resolution is a prerequisite for single protein detection. To this end their specificity and functionality must be preserved. Biological questions such as target-protein binding may than be addressed. Conventionally, recognition molecules are immobilized covalently onto pre-patterned surfaces. This method requires precisely dimensioned patterns with a material contrast that allows covalent and directed immobilization of the recognition molecules on the patterns and guarantees low unspecific binding of any protein in the space between the patterns.

We have developed a new procedure to immobilize individual designed ankyrin repeat proteins (DARPins) directly through a nanofabricated polymer mask on a flat substrate and we use such functionalized surfaces as a sensor platform to detect single proteins bound to the DARPins. The immobilization process combines nanometer sized hole masks with the outstanding stability of DARPins. Whereas in conventional single molecule immobilization techniques recognition molecules are immobilized after the lift-off of the polymer mask on patterns of, e.g., biotinylated linker molecules, or gold[1] or silver layers, DARPins withstand the lift-off process by organic solvents and can therefore be immobilized directly through the polymer mask (Figure 1). After the mask is dissolved by harsh lift-off protocols including sonication in an acetone bath, the DARPin remain covalently bound on the surface in the position predefined by the mask. On the same chip DARPin patterns could be produced from millimeter sized areas down to single DARPin immobilization by varying the hole size of the mask. Furthermore, sensitivity to different target proteins was achieved by immobilization of different DARPin clones in different areas of the same chip.

For the mask, poly methyl methacrylate (PMMA) was spin cast on a silicon dioxide substrate and structured using state of the art e-beam lithography and nanofabrication methods. To covalently immobilize DARPin molecules a bifunctional heterospecific cross-linker was used in combination with an amino silane.
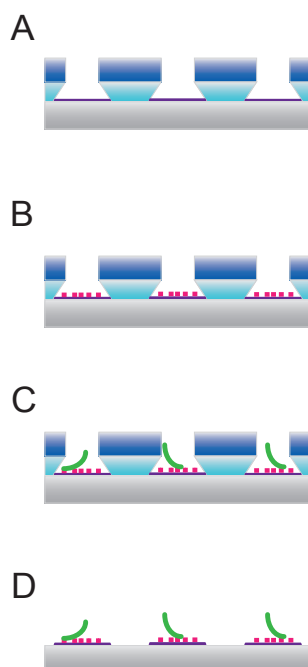
Figure 1.   Single DARPin molecules can be immobilized covalently through a photoresist mask on oxidized silicon and withstand the lift-off of the mask by an acetone ultrasonic bath. The immobilization and lift-off process involves the following steps. (A) Patterns of PMMA made by EBL on an oxidized Si wafer are functionalized with a layer of amine at a gas-phase silanization of an amino-silane. (B) Functionalization of the amine layer with a heterospecific bifunctional linker which binds on one end to the amine with its NHS-ester and exposes at the other end its maleimide groups. (C) These maleimide groups bind DARPins engineered with one cysteine at their c-terminus. (D) After immersion and sonication in acetone, the PMMA mask is lifted and leaves functional active DARPins covalently bound to the oxidized Si wafer from single molecule resolution up to patterns of many molecules, depending on the pattern openings of the mask.

7.4 Results and Discussion

7.4.1 Stability of DARPins in Organic Solvents

To evaluate the performance of DARPins to fully resolubilize and regain their specific affinity after precipitation in an organic solvent, their binding capacity was measured by an ELISA (Figure 2 A). Off7, a 14 kDa sized DARPin with an high affinity for the Escherichia coli maltose binding protein (MBP) (KD = 4.4 nM) was incubated on MBP-biotin coated streptavidin ELISA plates[2]. For comparison, Off7 in PBS was precipitated in different organic solvents including dichloromethane (DCM), dimethyl sulfoxide (DMSO), acetone and dimethylformamide (DMF). All the used solvents are common in micro- and nanofabrication processes to lift-off masks. Off7 immediately precipitated in all solvents due to the lower dielectric constant of the solvent enriched media[3,4,5]. By dialysis against PBS all solvents could be removed and the Off7 was fully resolubilized and used for the ELISA. Off7 bound to MBP on the ELISA plates was detected by colorimetric determination of the enzymatic activity of an HRP labeled IgG which is binding to the His-tag of Off7. No significant difference between the signals of solvent treated Off7 and the signals from the controls were measured. Within the solvent treated samples, the resolubilized Off7 from precipitation by DMSO showed a slightly lower signal. Usually, many proteins irreversibly degenerate when treated with organic solvents. Indeed Off7 precipitates from the buffer solution during treatment with the organic solvents, but it can be fully resolubilized and regains its high affinity.

7.4.2 Fluorescence assay using immobilized DARPins

A polymer thin film mask was used to create patterns of Off7 on silicon dioxide in order to demonstrate that DARPins regain their affinity after precipitation not only in solution but also when immobilized on a surface. E-beam lithography was used to create structures in PMMA spin coated on a surface-oxidized silicon wafer. The structures included cavities of 2 mm in length and 1.5 μm in width produced in very close proximity to 150 nm wide lines and arrays of 1000 x 1000 holes with few nm in diameter (layout see Supplementary Figure 1). Through the
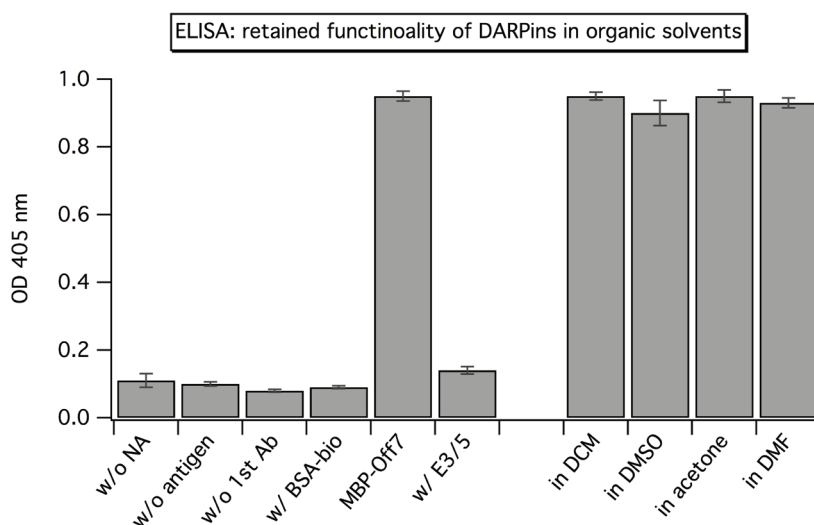
Figure 2 A.   DARPins retain their high specific affinity after immersion in different organic solvents in solution and immobilized on surfaces, where successfully sandwich immunoassays can be performed with various DARPins. (A) An ELISA assay was done to determine the activity of DARPins immersed in different organic solvents. The left side includes binding assays and their controls without the influence of organic solvents. On the right side, the binding activity of DARPins was determined after immersion in one of four different organic solvents including DCM, DMSO, acetone and DMF. After the addition of anti-His IgG labeled with HRP, the optical density at 405 nm was measured and plotted against the corresponding condition.
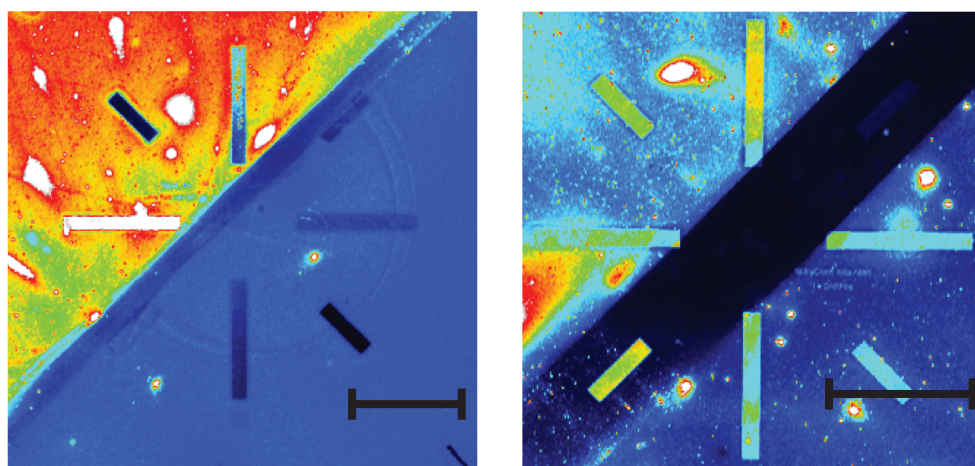
Figure 2 B.   On the left side, two different DARPin clones have been immobilized on the same chip and their corresponding targets has been applied. The sectioning was achieved by using a thin elastic polymer septum made out of PDMS. For the DARPin immobilization, the septum was placed at the position northeast to southwest, what allows pipetting Off7c at the lover left corner and Ec1c at the upper right corner. For the addition of the target, the septum was placed after lift-off and blocking at the position northwest to southeast and MBP-bio has been pipetted at the upper left corner and EpCamEx at the lower right corner. On the right side, a surface immunoassay on oxidized Si done with covalently bound Off7c over the whole chip. MBP-bio as target molecule has been applied in two different concentrations, with 500 nM at the upper left corner and 250 nM at the lower right corner. Again the two solutions have been separated by the PDMS septum. The patterns of MBP-bio bound to Off7c and EpCamEx bound to Ec1c were both visualized using streptavidin labeled with the fluorescent molecule AlexaFluor488. The conformal contact of the PDMS septum and the surface has been enough to completely seal the two compartments from any leaking (scale bars 2 mm).

mask, the silicon dioxide surface was functionalized with amino-silane using a gas-phase silanization process. A heterospecific bifunctional linker was then used to bind the DARPins covalently to the silicon dioxide surface. The linker binds on one end with its NHS ester to the amine of the amino-silanized silicon dioxide and exposes on its other end the maleimide. DARPins engineered with a freely accessible single cysteine at their c-terminus form stable carbon-sulfur bond between their thiol group and the maleimide. Besides the specific binding of the Off7c to the maleimide functionalized areas, unspecifically binding might also happen on the PMMA mask. However during lift-off, the mask and adhering proteins are removed, leaving well-defined Off7 patterns surrounded by protein-free silicon dioxide (Supplementary Figure 3). Usually proteins totally denature when they are immobilized on surfaces and treated with organic solvents. However, after resolubilization of Off7c and passivation of the free silicon dioxide surfaces against unspecific protein binding, a surface immunoassay could be performed. MBP-bio was incubated on Off7c-functionalized surfaces and after removing the unbound MBP-bio by rinsing, the remaining was labeled with a fluorescent streptavidin conjugate (SAvAF-488). To prove the general stability of DARPins, Ec1c, a second clone, was immobilized as recognition element. Patterns of the two different DARPins were produced on the same chip (Figure 2 B) and used in a fluorescence immunoassay where their specific target molecules were detected. The results verify that DARPins regain both, their high affinity and specificity after the immobilization and lift-off processes.

7.4.3 AFM measurements of line patterns

To approach label free single molecule detection, we propose to discriminate the bound and unbound state of immobilized DARPins by AFM. Thanks to the small size of DARPins, a complex formed of one DARPin and its target molecule is expected to be more than the double of the size of a single DARPin (Supplementary Figure 2). Such a change in the size should be detectable as a change in height in the AFM profiles. Furthermore the used linker has a much better defined length than microfabricated metal immobilization islands. Although the fabrication of nanometer sized patterns with similar size of single

120

DARPin molecules has recently made big progresses[6], the heights of dots fabricated within an array, still varies between one to two nm, what makes a discrimination by AFM difficult. AFM measurements (Figure 3) of 150 nm wide line structures show well visible height differences in patterns of the linker, of Off7c immobilized via the linker and of MBP-bio bound to the immobilized Off7c. To measure the height of patterns of the linker only (Figure 3 A), the linker was blocked by cysteine before lift-off. Despite the limited length of the blocked linker molecule, distinct lines are clearly visible. When Off7c was immobilized and after lift-off the remaining silicon dioxide was blocked with casein. The measured height of the lines was significantly compared to the structures of the linker only. Furthermore, two populations within the height measurements can be determined which may correspond to the two different configurations, in which the elongated Off7c molecules can be immobilized on surface. A model made from crystallographic data of a DARPin-MBP complex describes the expected configurations (Supplementary Figure 2). Due to the high flexibility of linker which contains two PEG units and the two glycines between the C-terminus of the DARPin and the engineered cysteine, an immobilized Off7c can be placed in upright or in lying position. To prove the binding capacity of Off7c immobilized in 150 nm wide lines, MBP-bio was incubated (Figure 3 C). Binding between the Off7c and the MBP-bio is evident from distinct and localizable features with an increase of the height of more than 5 nm.
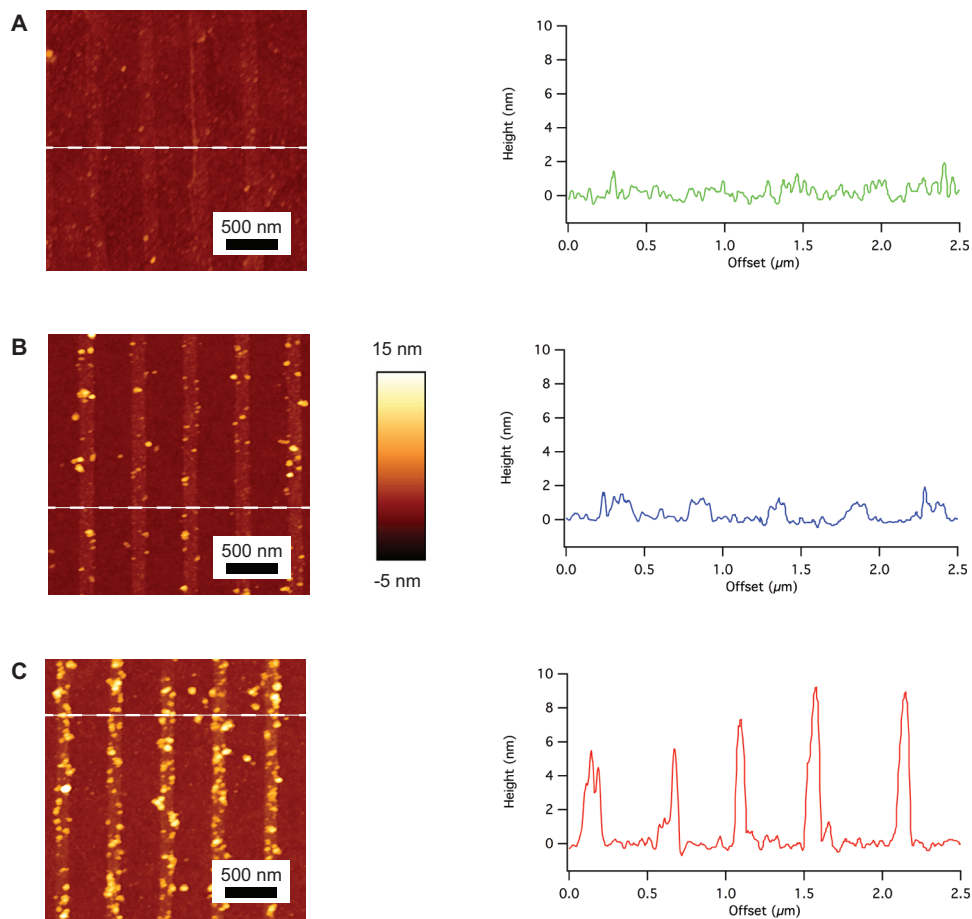
Figure 3. Label free detection of MBP-bio bound to covalently immobilized Off7c trough a 150 nm wide line mask. (A) AFM height image without the immobilization of Off7c. Only the bifunctional cross-linker was immobilized within the 150 nm wide lines and the Maleimide groups were directly blocked using cysteine. After lifting the mask and blocking with caseine, MBP-bio was incubated (left). The height sections show a slight increase within the lines, due to the immobilized linker (right). (B) No MBP-bio was applied and only Off7c was covalently bound to the linker in the lines and the chip was blocked after

lift-off with caseine. PBS without MBP-bio was applied on the chips and the AFM height image (left) and the height sections (right) showing homogenous line patterns of 1 to 1.5 nm above background, which is due to the immobilized DARPin. (C) AFM images of the full assay of MBP-bio bound to Off7c immobilized within the lines (left). The height profiles show a plateau at around 1 to 1.5 nm which is due to the immobilized Off7c. Bound MBP-bio is measured in peaks of 5 to 8 nm height (right).
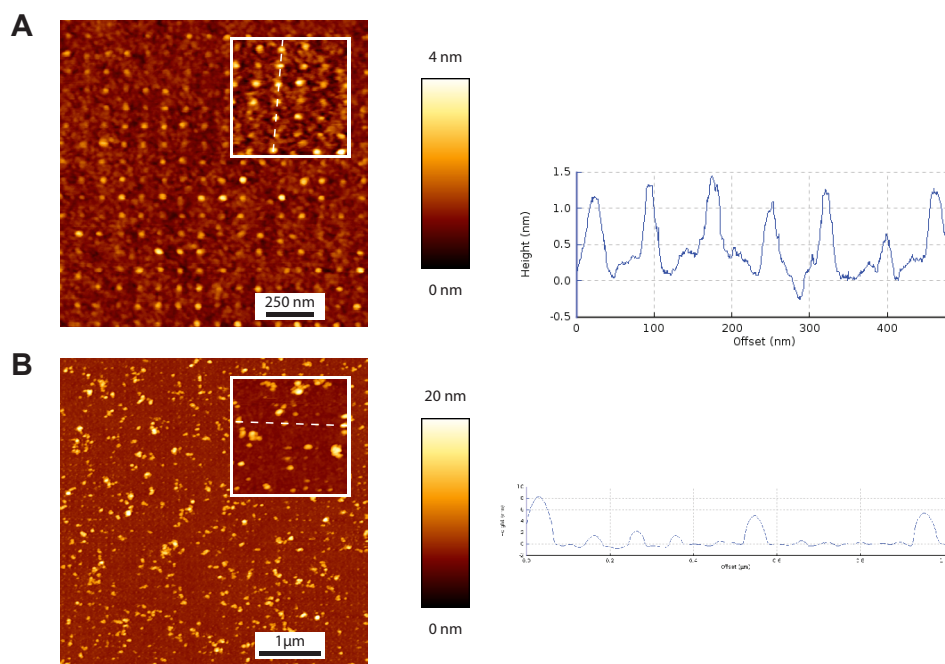
Figure 4.   Single Off7c molecules are immobilized on an array as individual recognition elements, to detect the binding of single MBP-bio molecules. (A) AFM measurements show a height of single Off7c molecules of 1 to 1.5 nm. Only very few positions in the array are not occupied by Off7c molecules. (B) MBP-bio was incubated for 60 minutes on arrays of Off7c molecules, AFM images after washing (left) demonstrate the binding of single MBP-bio on the Off7c array. Height trace profiles confirm a size of the bound MBP of 5-8nm.

7.4.4 AFM measurements of array structure

Single individual Off7c molecules could be immobilized in distinct arrays using the 10 nm PMMA hole-array mask. After lift-off of the mask and passivation of the remaining silicon dioxide surface, AFM measurements (Figure 4 A) showed the same heights on the immobilized single molecules as on the Off7c immobilized within the lines. On such arrays of single immobilized Off7c molecules, MBP-bio was incubated and the height differences were again determined by AFM. The line profile of the section marked with a white dashed line in the inset of Figure 4 B shows three binding events of MBP-bio on individually immobilized Off7c. The increase of the height measured when a complex between Off7c and MBP-bio was formed is again similar to the height differences measured in the line structures. On the array, also some agglomerates of MBP-bio were detected, which might be formed from MBP-bio molecules before their binding to the patterns and which could be probably removed by centrifugation of the sample before incubation on the Off7c functionalized array.

7.5 Conclusion

Single DARPins were successfully immobilized through a PMMA mask on silicon dioxide. Their affinity and specificity after the lift-off of the mask by acetone was shown in binding assays with their targets and detected either using fluorescence labels or a label-free detection. This label-free detection which is based on the height discrimination of bound and unbound DARPins by AFM, allowed us to detect single binding events. The proposed protein detection platform not only opens new ways for highly specific and sensitive sensor platforms but also new immobilization methods to produce very precise patterns of recognition elements, which reach single molecule resolution. The outstanding stability of DARPins against organic solvents might also be of interest in organic chemistry, where organic solvents are often used but also functionalization of recognition elements are necessary.

7.6 Materials and Methods

7.6.1 Preparation of DARPins

The used recognition element was Off7, a DARPin with high affinity towards maltose binding protein (MBP). The C-terminus of the protein was fused to GGC in order to use the very c-terminal cysteine for immobilization or for further conjugation. After expression in E. coli and IMAC purification, Off7c was aliquoted, snap frozen and stored at -80 degrees. Before immobilization, Off7c was thawed, potential dimers formed by disulfide bridges were reduced using 50 mM TCEP during 30 min at 37 degrees with gentle agitation. TCEP was separated from the reduced Off7c by a PD10 size desalting column from GE.

7.6.2 MBP-bio and fluorescence measurements

MBP-bio was a kind gift of Dr. Birgit Dreier. For fluorescence labeling, AlexaFluor488 labeled streptavidin was used (Pierce) and measured in a Tecan LS400 fluorescence scanner.

7.6.3 AFM measurements

For AFM measurements, the samples where washed with distilled water and dried under a nitrogen flow. Conical shaped silicon tips from MicroMesh (NSC15) with a typical spring constant of 40 N/m and a resonance frequency of about 325 kHz has been used in non contact mode on a NanoWizzard II AFM from JPK.

7.6.4 DARPin immobilization

Oxidized silicon wafer were spin coated by a double-layer of poly(methyl methacrylate) (PMMA) positive tone resist. The first layer is made with PMMA with a low molecular weight of 50 kDa followed by a layer with a molecular weight of 950 kDa. Both layers have a thickness of 30 nm and after each coating, a

bake-out step during 5 min at 175 degrees followed. E-beam lithography of such resist coating results in a slight undercut profile, which is preferable for lift-off processes. Such prepared samples where gas phase silanized with monoethoxy-dimethyl amino silane (ABCR). The samples were introduced in a 2 liter vacuum reactor and coated during 20 minutes with 10 µL of the amino silane injected into the reactor at a pressure of 7 mbar. After intensely rinsing with distilled water, 10 µM of an heterospecific bifunctional linker dissolved in PBS buffer was applied at room temperature during 60 minutes. The linker consist of an ethylene glycol dimer with a sulfo-NHS ester on one end and a maleimide group at the other end(Pierce). After binding of the linker, the samples were incubated for 60 minutes with Off7c which was reduced with TCEP. To completely block all maleimide groups of the linker, 10 mg/mL of cysteine in PBS was pipetted on the chip and incubated during 10 minutes. To lift-off the PMMA mask, the chip was 3 times flushed with 1 mL of acetone and then shaked in an acetone bath for 2 minutes with a 5 second ultrasonic burst at the end. After carefully rinsing with distilled water, the remaining silicon dioxide surface was blocked with 10x Caseine blocking solution (Roche) for 60 min. MBP-bio at a concentration of 10 µM was pipetted on the chip and incubated for 60 minutes for the binding assay. Fluorescence labeling, if necessary, was done with AlexaFluor488 labeled streptavidin (Pierce) for 60 minues.

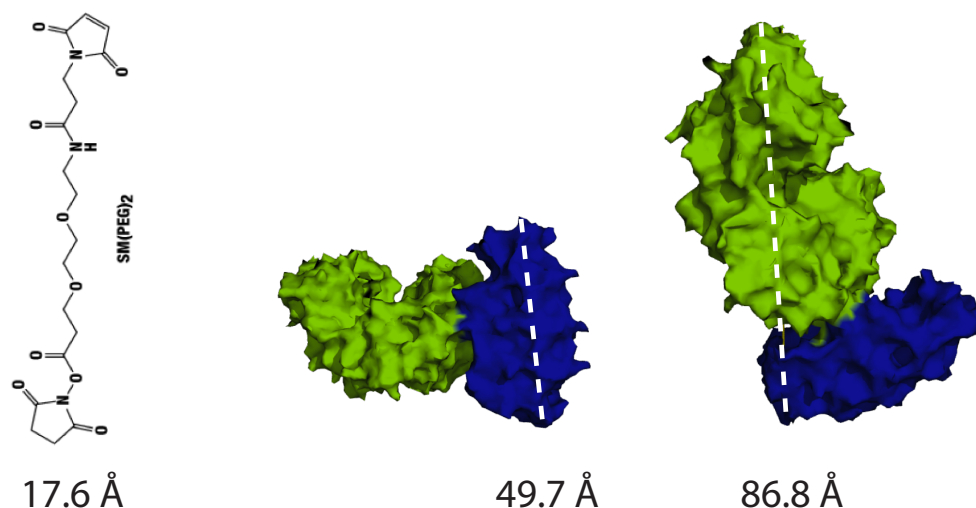## 7.7 Supplementary Figures

Supplementary Figure 1   EBL layout

Supplementary Figure 2   Linker and DARPin model

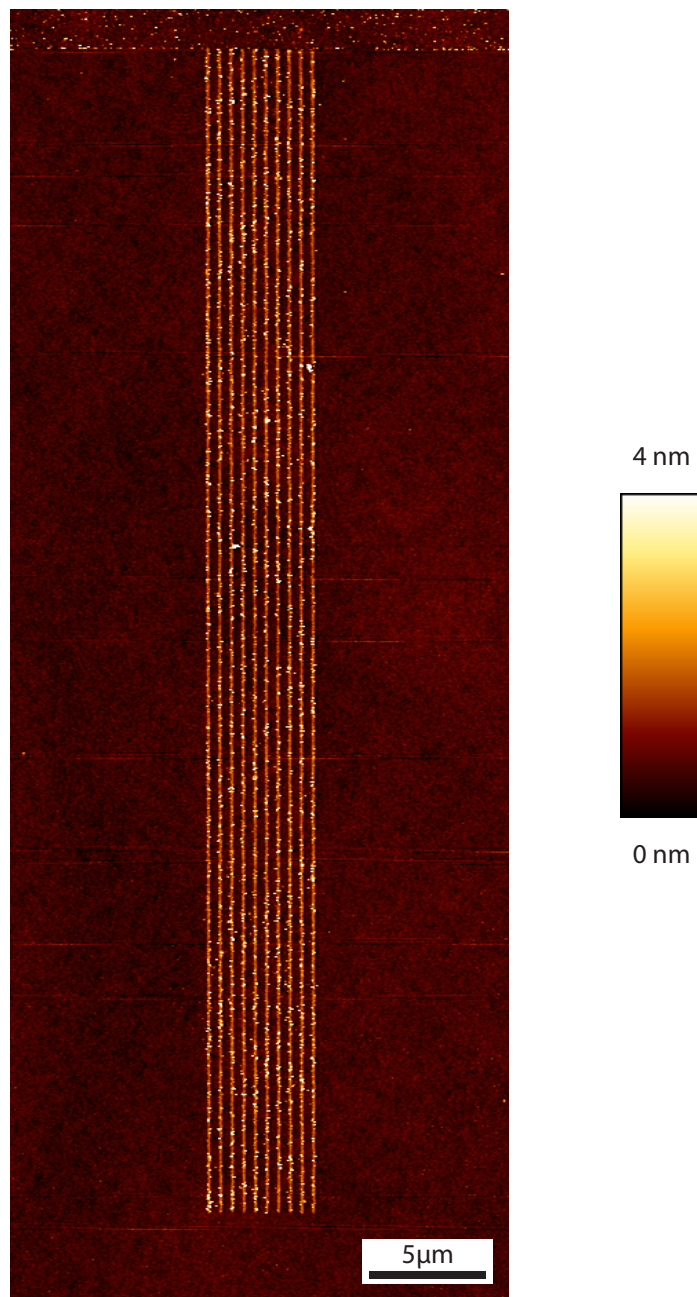**Supplementary Figure 3**   More AFM measurements of line patterns
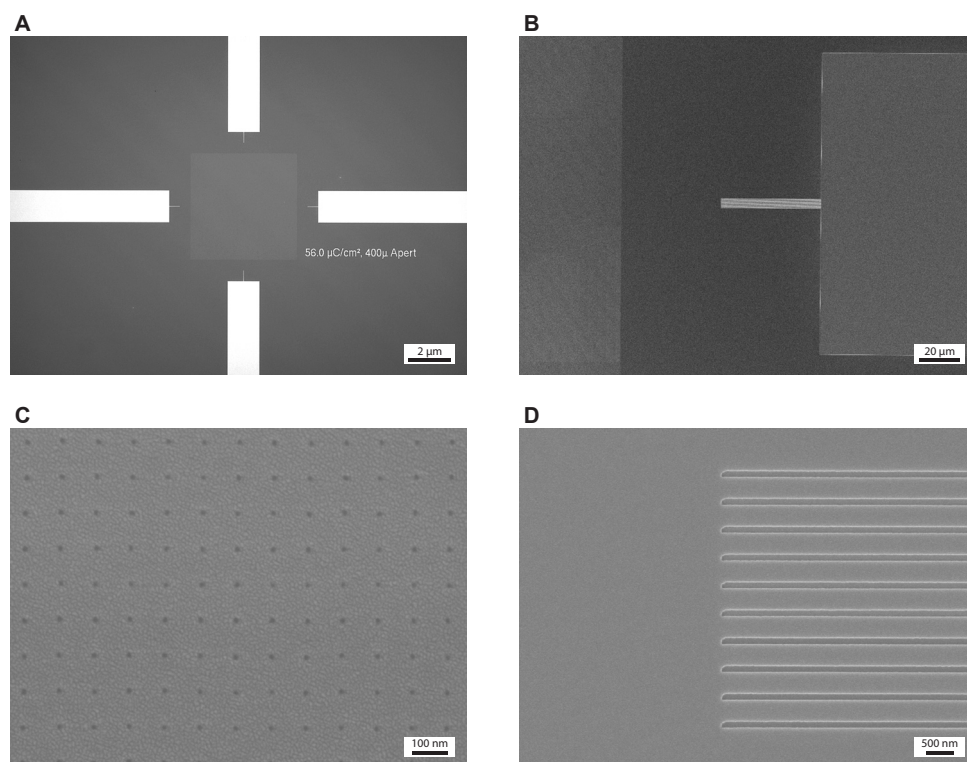
Supplementary Figure 1.   EBL layout

The chip consists of three different patterns besides a label which informs about the dose and the aperture used at the e-beam. The patterns cover areas of several mm to 10 nm dots and can be used in assays and serve in addition as guiding structures. (A) Without any maginification, four lines arranged perpendicular to each other are visible and can be used as guides by eye. Using optical microscopy, the nm dot array can be seen in the center of the four guiding structures as a light grey square. (B, C) SEM pictures show between the end of a guiding line and the nm dot array 10 additional guiding lines. Their width is 150 nm and they are 50 nm long, half the distance between the nm dot array and the big guiding lines. (D) The square sized nm dot array has a side length of 500 nm. After a thin metal layer of 1 nm Cr and 2 nm Au, electon microscopy shows the 10 nm holes made by e-beam with a pitch of 100 nm.

17.6 Å　　　　　49.7 Å　　　86.8 Å

Supplementary Figure 2.　Linker and DARPin model

Length scale of molecules and complexes used in the experiments. The heterospecific bifunctional linker has a length of about 17.6 Å corresponding to the manufacturers information. The linker has in its middle two PEG entities and the Off7 has its cysteine engineered with a two glycine. This gives the immobilized Off7c a high flexibility and two positions are possible, at which Off7c can bind its target. Either the paratope from Off7c is accessible by the side, when Off7c is immobilized upwards or the paratope is exposed upwards, when the Off7c is bendet. The crystal structure of the Off7c and the MBP-bio complex can act as a model to determine the hights, which can be expect using our label free approach. When the paratope is located at the side, the highest part of the complex is the DARPin length, which is in this case around 5 nm. On the other hand, 8.5 nm measures the complex, when the paratope is positioned upwards, what is the length of the Off7c including the MBP-bio.

Supplementary Figure 3.   More AFM measurements of line patterns

AFM image of the lines, on which Off7c is immobilized, without MBP-bio. The lines are very homogeneous and almost the full length is covered with Off7c. However beside the lines are no unspecific binding visible, which demonstrate the high efficiency and precision of the presented immobilization method.

7.8 References

1   Glass, R.; Arnold, M.; Cavalcanti-Adam, E. A.; Bluemmel, J.; Haferkemper, C.; Dodd, C. & Spatz, J. P.Block copolymer micelle nanolithography on non-conductive substrates*New Journal of Physics,* **2004***, 6*, 101.

2   Binz, H. K.; Amstutz, P.; Kohl, A.; Stumpp, M. T.; Briand, C.; Forrer, P.; Grutter, M. G. & Pluckthun, A.High-affinity binders selected from designed ankyrin repeat protein libraries*Nat Biotech, Nature Publishing Group,* **2004***, 22*, 575-582.

3   Pierce & TR0049.0
Acetone precipitation of proteins
Pierce, **2004**

4   Thongboonkerd, V.; Mcleish, K. R.; Arthur, J. M. & Klein, J. B.
Proteomic analysis of normal human urinary proteins isolated by acetone precipitation or ultracentrifugation
Kidney Int, **2002***, 62*, 1461-1469.

5   Hagerman, A. E. & Butler, L. G.
Protein precipitation method for the quantitative determination of tannins
Journal of Agricultural and Food Chemistry, **1978***, 26*, 809-812.

6   Guzenko, V. A.; Ziegler, J.; Savouchkina, A.; Padeste, C. & David, C.
Fabrication of large scale arrays of metallic nanodots by means of high resolution e-beam lithography
MNE, **2011***, accepted.*

8. General Conclusions and Outlook

Scope of the thesis – The main goal of my thesis was to develop platforms and protein sensors to provide appropriate methods towards single cell proteomics. Therefore we used and combined different detection methods such as optical, electron and atomic force microscopy with devices made by micro- and nanofabrication methods and by chemical surface modification. We could successfully produce platforms for cell growth and protein sensors including whole cell content analysis and immunochemical determination of protein concentrations down to the single molecule level.

Protein analysis using microfluidic systems – By using stencils microfabricated in silicon dioxide, patterns of cAbs were immobilized on poly(dimethylsiloxane) (PDMS), with high accuracy and in a manner compatible to mass fabrication (chapter 2). Such prepared PDMS substrates reversibly seal microfluidic reaction chambers to perform surface immunoassays using capillary systems (CS). Besides the reaction chamber, the developed CSs features channels and capillary pumps to control the analyte, as well as pads to load reagents and samples using micropipettes. For convenient cleaning by UV-ozone before use and reuse, the CSs typically are micro-fabricated in silicon dioxide. Using the CSs covered with cAb patterned PDMS, a surface immunoassay with fluorescence labels was performed, to detect the concentration of CRP in human blood serum. By only four consecutive pipetting steps, CRP was successfully detected within eleven minutes. The calculated sensitivity of the assay is 0.9 ng mL^{-1}, i.e., 7.8 pM, whereat only 1 μL of analyte sample was needed. In the use of such high performance immunoassays, well defined patterns of cAbs are very important. The developed method using stencils to homogenously pattern cAbs on PDMS with a feature size of a few tens of micrometers in lateral dimensions not only minimizes the amount of used cAb reagents. It also helps limiting the depletion of analytes and can be spaced so as to provide many contiguous signals and controls, which is useful for the combinatorial screening of analytes, and for achieving assays with small intra-assay variations.

Separation, handling and culturing of individual cells – In Chapter 3 we used the mobile nature of BalbC neural stem cells to investigate the effect of high aspect ratio structures in poly(L-D,L-lactic acid) (PLLA), on the cell outgrowth in distinct directions. PLLA was chosen because of its good biocompatibility and the strong adhesion of fibronectin to its surface, which additionally enhances cell growth. For the topographic patterning, structures with aspect ratios (AR) of 1:5 in the size range of 100 nm to 10 μm were reported to have the necessary influence on cell outgrowth[1, 2, 3, 4]. Generally, in cell experiments, biocompatible substrates have to be provided in large numbers to be able to perform several test runs. Furthermore, structures on the substrates have to be homogenously fabricated to ensure that the structures and not the defects within the structures influence the cells. Replication processes are ideal methods that fulfill the request for high throughput combined with high feature quality. In replication processes, a reusable template is fabricated and used as a master. For our master fabrication with features in the micrometer to 100-nanometer scale, microfabrication processes in silicon dioxide were used, including e-beam (EBL) patterning of thin-films, metal evaporation and reactive ion plasma etching. However it was a big challenge, to detach the soft and brittle PLLA from the silicon dioxide master without breaking the structures on the surface. Therefore we developed a two-step replication process, where the silicon dioxide substrate is a positive master that served to produce a polydimethylsiloxane (PDMS) negative master, on which the PLLA was poured. To entirely peel the fragile PLLA layer from the PDMS master after curing, without damaging the high AR nanometer scale structures, the following properties of the PDMS proved to be beneficial. PLLA is dissolved in chlorinated solvents. During the curing of the PLLA on the PDMS master, the small, chlorinated solvent molecules can enter the PDMS mesh, but not the bigger PLLA molecules, leading to an increased concentration and eventually to solidification of PLLA at the PDMS surface. The solvent, accumulated in the PDMS mold leads to a slight swelling of the PDMS, which is reversible and the PDMS mold returns to its original volume after the evaporation of the solvent over time. Furthermore, the flexibility and the low surface energy of the PDMS master help to peel the PLLA substrate from the PDMS master, without destroying the high AR structures. Using 2 x 2 mm arrays of cone structures with AR of 1:5 and top diameters of 120 nm we

could show the influence of inter-pillar distances on cell outgrowth along the cone-lines. Our method allows preparing substrates for studying the growth of individual cells under well-defined conditions and environmental stimuli. Furthermore the produced substrates might be useful to separate single cells from cell clusters using their migration activity.

Analytics at the level of single cells – A method was developed to write total content sample preparation on EM grids for structure and mass analysis by transmission EM (TEM) and scanning TEM (STEM) respectively (Chapter 4). In classical staining of protein solutions on EM grids, the sample is first pipetted onto the grid and is followed by a staining step. After each of the two steps, a blotting step has to be performed to remove the excess liquid. Unfortunately these blotting steps leave only a fraction of the sample that is stained on the grid. The major part of the sample is taken up by the blotting paper. In our direct content writing method, we minimized the loss of the analyte solution. A thin nozzle filled with the cell lysate comes in close contact to the hydrophilic grid and deposits the cell content in meandered structures onto the carbon coated electron microscopy grids. Before the writing, the solution flows through a cellulose fiber, surrounded by heavy metal stain or double distilled water, respectively. By dialysis, the biological sample is mixed and negatively stained or undesired salts are removed. With negatively stained protein samples deposited on EM grids, transmission EM can be used for the structure analysis, while desalted samples are used for the mass analysis by scanning TEM. Since we are using EM analysis techniques, the cell lysation needs to be done without addition of chemicals and was achieved by sonication at 25 kHz during 2 min while cooling. The structures detected with EM will be compared to known protein structures listed in protein databases using dedicated software algorithms. This will allow the mapping of the EM measurements to specific proteins and the determination of their relative concentration on the EM grid, which is in relation to the protein concentration in the corresponding lysed cell[5].

AFM-based proteomics – Measuring the height of a single receptor molecule by AFM, a label free discrimination of its bound or unbound state should be possible. By measuring hundreds of single receptor molecules, the protein concentration within an analyte can be determined statistically with a theoretical detection limit of one molecule. Therefore we developed arrays of immobilization islands to bind single receptor molecules on very flat surfaces. As receptor molecules, the small but highly specific DARPins have been chosen and for the fabrication of the immobilization islands, extreme ultraviolet interference lithography (EUV-IL) and EBL as well as a newly developed direct immobilization method of single DARPin molecules was used.

In EUV-IL, a coherent beam of extreme ultraviolet light with a wavelength of 13.4 nm is diffracted by grating structures and creates an interference pattern. Information in the form of the interference pattern is recorded on a photoresist-coated substrate[6]. By using parallel line gratings, large area periodic lines with a half pitch of 11 nm have been achieved[7]. To produce a hole mask, the beam has to be diffracted at line gratings perpendicular to each other. Based on the intensity distribution of the four diffracted beams on the surface, masks with hole sizes of about 60 nm and a period of 100 nm have been produced as described in *chapter 5*. To immobilize single DARPins, the hole size has to be further diminished to obtain smaller immobilization islands. For this purpose we used glancing angle metal depositon (GLAD) of chromium followed by silver. To homogenously shrink the hole size, the substrate is rotated around an axis perpendicular to the substrate during metal deposition. Chromium was first deposited to get a maximum constriction of the hole in the PMMA. About 50 % of the origin hole diameter could be reached. Due to the accumulation of grains and flakes of the chromium during deposition, the holes lost their round form as before the chromium deposition. To obtain more round shaped holes after chromium deposition, silver was additionally deposited, which reduced the irregularity of the hole structures due to it's higher fluidity. Even if GLAD could reduce the hole size of EUV-IL produced masks by 50 % the resulting immobilization islands have still a diameter of about 30 nm. However on 30 nm sized immobilization islands, several DARPins that have a total length of around 8.5 nm and a width of 5 nm could theoretically be immobilized.

State of the art EBL was found to be the appropriate method, to produce gold immobilization islands of 6 nm in diameter (Chapter 6). In EBL a beam of electrons is scanned over a resist coated surface. Patterns are generated by exposing the resist and selectively removing either the exposed (negative resist) or the non-exposed (positive resist) during developing. Elecron beams have a wavelength of only a few picometers and can be focused very well. Beam spots of 2-3 nm are common and the resolution of EBL is nowadays mainly determined by the resist resolution, scattering effects and proximity effects including secondary electron generation. To produce the 6 nm gold islands on silicon dioxide with a pitch of 100 nm as described in chapter six, we used the single shot technique of a Vistec EB machine. Regular large area structures were achieved only after an improvement of the focusing unit of the machine. As the resist we used a double layer coating, where first the poly(methyl-methacrylic acid) (PMMA) with a relaively low molecular weight (PMMA 50 kDA) followed by a layer of heavier chains (PMMA 950 kDa) was spin-coated. E-beam lithography of such resist-coatings results in a slight undercut profile that is preferable for lift-off processes. After deposition of 1 nm of Cr, 2 nm of Au and a lift off using acetone, immobilization islands of 13 nm were obtained. An additional thermal annealing step was applied and allowed us to reduce the dot size by 50 % from around 13 nm down to 6 nm. On silicon dioxide with a roughness of less than 0.3 nm gold immobilization islands patterns with a diameter of 6 nm could be successfully fabricated[8] and are ready to be functionalized by single DARPins.

But to functionalize only the gold islands with DARPins, the surrounding silicon dioxide surface has to be protected against non-specific DARPin adsorption before the incubation of the DARPins. However a passivation with commonly used PEGs let to a fully coverage of the surface including the immobilization islands which have been either blocked by unspecific binding of PEG molecules or which have been buried by PEG molecules, since they have chain length several times longer than the 3 nm high gold immobilization islands. Therefore it would be preferable to immobilize the DARPin on the substrate, before the lift-off of the mask. Single DARPin molecules could then bind to the substrate through the holes of the mask and DARPins non-specifically bound to the mask are washed away during the lift-off of the mask. However recognition molecules,

immobilized in this way have to remain functional after the lift-off process in organic solvents, what has been shown using DARPins, but is usually not the case for other protein based recognition molecules.

The direct immobilization of DARPin molecules through an EBL patterned PMMA mask on silicon dioxide substrates has been developed and is described in chapter 7. Through the holes of the PMMA mask, the silicon dioxide is first functionalized with a layer of amino-silane and a heterospecific bifunctional linker capable to bind to the sulfur provided by free cysteins at the C-terminus of specifically engineered DARPins. After immersion and sonication in acetone, the PMMA mask is lifted and leaves functional active DARPins covalently bound to the oxidized silicon wafer. Using the newly developed method, we could immobilize DARPins within various structures on the same substrate ranging from several µm wide and mm long lines down to arrays of openings in a size to immobilize single DARPin molecules. The DARPin functionalized surfaces were successfully passivated and used to detect target proteins, either with fluorescence within the big µm to mm binding sites, or with the described height discrimination using the AFM within the single DARPin molecule arrays. Single binding events have been successfully measured and bound and unbound DARPins could be discriminated.

Outlook – The developed surface for cell growth and the methods to detect proteins are promising tools for the analysis towards single cell proteomics. The immunoassay in capillary systems using through-stencil immobilized cAb, is notably fast, sensitive, and economical of sample compared with commercially available ELISA assays. The sensitivity might be further improved by employing signal-amplification strategies similar to the work by Hosokawa et al.[9]. Since the developed method is fairly flexible and straight forward to use, it has promising chances to replace the microtiter platform and is very suitable for point of care applications. A combination of the presented cell growth surface with the pipetting device used for writing the EM grids and the developed method to detect singe protein molecules, would allow to determine the small concentration of proteins expressed in single cells. The yet slow detection based on the size

discrimination of bound and unbound single DARPins by AFM, can be accelerated in future by using high-speed AMF[10] or arrays of AFM tips[11] for scanning. Recent developments in the resolution of fluorescence microscopy[12] may be an alternative detection for single molecule binding events and may deliver the necessary high throughput for the statistical relevance to determine the proteome of single cell.

8.1 References

1   Shalek, A. K.; Robinson, J. T.; Karp, E. S.; Lee, J. S.; Ahn, D. R.; Yoon, M. H.; Sutton, A.; Jorgolli, M.; Gertner, R. S.; Gujral, T. S.; MacBeath, G.; Yang, E. G. and Park, H. *Proceedings of the National Academy of Sciences of the United States of America* **2010**, *107*, 1870-1875.

2   Bettinger, C.; Langer, R. and Borenstein, J. *Angewandte Chemie International Edition, WILEY-VCH Verlag* **2009**, *48*, 5406-5415.

3   Martìnez, E.; Engel, E.; Planell, J. and Samitier, J. *Annals of Anatomy - Anatomischer Anzeiger, Special Issue - Stem Cell Research* **2009**, *191*, 126-135.

4   Cyster, L. A.; Parker, K. G.; Parker, T. L. and Grant, D. M. *Biomaterials* **2004**, *25*, 97-107.

5   Aderem, A. *Cell* **2005**, *121*, 511-513.

6   Park; When top-down meets bottom-up: EUV and X-ray interference lithography for sub-20-nm features; **2010**.

7   Auzelyte, V.; Dais, C.; Farquet, P.; Grutzmacher, D.; Heyderman, L. J.; Luo, F.; Olliges, S.; Padeste, C.; Sahoo, P. K.; Thomson, T.; Turchanin, A.; David, C. and Solak, H. H. *J. Micro/Nanolith. MEMS MOEMS, SPIE* **2009**, *8*, 21204-10.

8   Zhang, F.; Baralia, G.; Boborodea, A.; Bailly, C.; Nysten, B. and Jonas, A. M. *Langmuir, American Chemical Society* **2005**, *21*, 7427-7432.

9   Hosokawa, K.; Omata, M. and Maeda, M. *Anal Chem, Bioengineering Laboratory, RIKEN, 2-1 Hirosawa, Wako, Saitama 351-0198, Japan.* **2007**, *79*, 6000-6004.

10 Ando, T.; Uchihashi, T.; Kodera, N.; Yamamoto, D.; Miyagi, A.; Taniguchi, M. and Yamashita, H. *Pflugers Arch* **2008**, *456*, 211-225.

11 Polesel-Maris, J.; Aeschimann, L.; Meister, A.; Ischer, R.; Bernard, E.; Akiyama, T.; Giazzon, M.; Niedermann, P.; Staufer, U.; Pugin, R.; de Rooij, N. F.; Vettiger, P. & Heinzelmann, H. *Journal of Physics: Conference Series* **2007**, *61*, 955-9.

12 Lemmer, P.; Gunkel, M.; Weiland, Y.; Mueller, P.; Baddeley, D.; Kaufmann, R.; Urich, A.; Eipel, H.; Amberger, R.; Hausmann, M. and Cremer, C. *Journal of Microscopy, Blackwell Publishing Ltd* **2009**, *235*, 163-171.

9. Acknowledgments

First of all I would like to thank Prof. Andreas Engel for giving me the possibility to work in his laboratory during my PhD. Andreas offered great flexibility and a major knowledge and fascination for science, which generates a very positive environment for research and an outstanding productive work atmosphere.

My special thanks go to Prof. Andreas Plückthun for supporting my work. He always found time for my questions and providing extremely sagacious, helpful and appropriate comments.

I express my deepest gratitude to Dr. Celestino Padeste for being an excellent supervisor and for his extraordinary skills at the bench in the laboratory, his great patience in explaining, correcting and writing and his straight way to give his opinion about sometimes crazy ideas popping out of my head.

I further wish to thank Dr. Thomas Braun for his friendship, fascination for research and for his ideas and great help within small and very big problems.

My thanks go further to friends and colleagues at the CINA in Basel, specially to André, Simon, Julia, Chris, Patrick F., Patrick B., Philippe, Paul and Karen and of course to Prof. Henning Stahlberg for fruitful, critical and future-oriented discussions.

I thank my colleagues Manuel, Lutz and Nikolas at the Biochemical institute in Zürich and Luc from the IBM Research Laboratories Zürich, for great discussions and their open-minded perspective onto science.

Furthermore I acknowledge support and many useful discussions from my collegueas at the PSI, specially from Mirco and the currently and former members of the ODRA 100 which are Sonja, Patrick H., Sankha, Nicklaus, André, Thomas and Alexandra from the Molecular cell Biology laboratory and all the great outstanding technical stuff at the PSI: Koni, Eugen, Rolf, Anja, Christian, Arnold, Thomas, Jana, Stefan, Bianca and Michaela.

And most importantly my thanks go to my entire family to whom I dedicate this work. I profoundly thank my parents for raising me, giving me so much of

10. Curriculum Vitae

Jörg Ziegler

⌨ joerg.ziegler@me.com
Date of birth: July 10, 1978
Nationality: Swiss

EXPERIENCE & EDUCATION

PhD, Biophysics   **May 2006 – February 2011**
IBM Research GmbH (Rüschlikon, Switzerland)
PSI (Villigen, Switzerland)
Biozentrum University of Basel (Basel, Switzerland)

Single molecule detection on nanopatterned substrates (paper published: ECS 2010; paper in preparation: Nat. Nanotech 2011) and immunochemical analysis using microfluidics (paper published: Analyt. Chem. 2008)

Master of Science, computer science and neurobiology   **October 2004 – April 2006**
Tokyo Institute of Technology (Tokyo, Japan)
Natural Sciences University of Fribourg (Fribourg, Switzerland)

Sensation of passive rotation about the vertical body axis during different human gaits in simulated environment and in the dark

Internship Biotechnology   **June 2005 – September 2005**
Japan National Institute of Material Science (Tsukuba, Japan)

Morphological change of fibroblast cells on titanium and platinum cultured at anodic and cathodic potentials
(Paper published, Corr. Eng. 2008)

Bachelof of Science, computer science and neurobiology   **June 2000 – September 2004**
Natural Sciences University of Fribourg (Fribourg, Switzerland)

EMPA MaTisMed Lab (St. Gallen, Switzerland)

Elektrophysiology on nerve cells in vivo and in vitro and data analysis using Fourier-transformation

Internship, Software programmer   **July 2000 – August 2000**
ATTIK System (Fribourg, Switzerland)

Development, programming and testing of databases and web content management systems

Federal Matura, Type A (*Gymnasium Disentis, Switzerland*)   **September 1993 – June 1999**

CERTIFICATIONS & TRAININGS

- Patenting in Life Sciences   **June 2010**

EXTRA CURRICULAR ACTIVITIES

- **2009 – 2011 co-founder of www.5stutz.ch** idea, businessplan, advertisement
- **1985 – 2011 trumpet player** first trumpet at Swiss National Youth Orchestra. At present: Trumpet in a Jazz-Trio
- **2004 – 2005 founder of an IT-teaching service for seniors** idea, businessplan, advertisement, teaching
- **1998 – 2005 3 movies** made and presented at Swiss film festivals
- **1995 – 1999 high-school athletic club** member and participation at national meetings
- **1994 – 1999 class speaker** 5 years consecutive class speaker at the high school

HOBBIES

- music (trumpet, singing)
- sports (swimming, basketball, kendo, iaido, boxing)
- japanese language and culture